CHAPTER 49

Computational and Theoretical Approaches to Unraveling the Permeation Dynamics in Biological Nanotubes

Shin-Ho Chung

Department of Theoretical Physics, Australian National University, Canberra, Australia

D. Peter Tieleman

Department of Biological Sciences, University of Calgary, Canada

CONTENTS

1. INTRODUCTION

All living cells are surrounded by a thin membrane consisting of an aggregation of two layers of phospholipid molecules, called the *lipid bilayer*, each molecule being composed of a polar head and a hydrocarbon tail. This thin membrane effectively partitions the external

ISBN: 1-58883-042-X/$35.00

Handbook of Theoretical and Computational Nanotechnology
Edited by Michael Rieth and Wolfram Schommers
Volume X: Pages (1–54)

medium from the internal medium. The dielectric constant of the hydrophobic interior of the membrane is about 2, whereas that of the electrolyte solutions on either side of the membrane is 80. Thus, no charged particles, such as Na^+, K^+, and Cl^- ions, can jump across the membrane. The amount of energy needed to transport one monovalent ion, in either direction across the membrane, known as the *Born energy*, is enormously high. For a living cell to function, however, the proper ionic gradient has to be maintained, and ions at times must move across the membrane to maintain the potential difference across the membrane and to generate synaptic or action potentials. To do so, nature has devised specialized, large, transmembrane protein molecules and inserted them densely across the membrane. These transmembrane proteins, known as *ion channels*, form water-filled passages through which ions can freely move in and out.

Ionic channels of living membranes play a crucial role in the existence of all living organisms. All electrical activities in the nervous system, including communication between cells and the influence of hormones and drugs on cell function, are regulated by opening and closing of membrane ion channels. Because these channels are the elementary building blocks of brain function, understanding their mechanisms at a molecular level is a fundamental problem in neurobiology. Moreover, elucidation of how single channels work will ultimately help us find the causes of, and potentially cures for, a number of neurological and muscular disorders.

The measurement of ionic currents flowing through single channels in cell membrane has been made possible by the giga-seal patch-clamp technique [1, 2]. A tight seal between the rim of the electrode tip and the cell membrane drastically reduces the leakage current and extraneous background noise, enabling the resolution of the discrete changes in conductance that occur when single channels open or close. The technique has so far proven to be a powerful tool for characterizing biologically important currents. It appears that all different main types of membrane ion channels have been discovered and characterized in the past 20 years. These fall into three broad classes. There are ligand-gated channels: these channels open when one or possibly two chemical molecules, known as *neurotransmitters*, secreted from nerve terminals, bind to the channel. Some channels, the so-called voltage-gated channels, open in response to step-changes in the electric field. Dipoles or charged residues in the channel protein interact with the sudden change in the membrane potential, and this interaction energy causes the channel to open briefly. The importance of the third class of ion channels, the second-messenger–mediated channels, is now beginning to be realized. A channel is activated either chemically or electrically, and this activation in turn triggers a cascade of biochemical events inside the cell. One of the products released in turn activates a cluster of these second-messenger–mediated ion channels.

All of these different types of channels obey a few general principles. A channel in the closed state acquires a small amount of energy, either binding energy or electrostatic energy, and goes into the open state. When a channel is in the open state, or a higher energy state, ions can flow through the central pore under the influence of chemical or electrical driving force. Some drugs and toxins can interfere with this process, making a channel less likely to open or more likely to stay in the open conformation once it opens. Others may physically occlude the ionic pathways, thus impeding the flow of ions across the open channel. A channel, once open, stays open for various intervals, usually a few milliseconds. How long it will stay open and when it will open again is determined by two random variables. In other words, it obeys the first-order Markovian process. A channel exists, mostly, in one of two states: fully closed or fully open. When a channel is fully open, we see an ionic current of about 1 pA (10^{-12} A).

Despite the wealth of information accumulated over the past two decades, some important questions about how biological channels work remain unanswered. The first among these questions is the detailed dynamical processes underlying the permeation of ions across an open channel. An ion in electrolyte solution does not move freely but drags along a shell of waters that are semipermanently bound to it. To give an example, the electrostatic binding energy of a water molecule in the first hydration shell of a Na^+ ion is about 10^{-19} J or 24 kT in room temperature units. This is a huge energy compared to the average kinetic energy of ions. To move across a narrow conduit, such as the selectivity filter of the potassium channel, the ion–water geometry needs to be rearranged, with partially dehydrated ions interacting

electrostatically with the charged residues on the protein wall. Second, all biological ion channels are selectively permeable to a specific ion. Channels generally discriminate anions from cations; some channels select sodium ions but reject potassium ions or *vice versa*. This selectivity mechanism needs to be understood in terms of the interactions of the permeating ions with the surrounding water and protein molecules. Third, what determines the upper-limit of channel conductance? To be functionally effective, a channel must process a large number of ions but, at the same time, it has to be highly selective to specific ionic species. It is a challenge to unravel the design that most satisfactorily reconciles these conflicting requirements. Fourth, what kind of structural changes take place when a channel makes transitions from the closed conformation to the open conformation? Whether the gating of biological ion channels is steric or controlled electrostatically, such as by rotating the orientation of a ring of dipoles guarding the channel gate, remains to be elucidated. Finally, the tertiary structures of all known ionic channels need to be determined. The solutions proposed for these unsolved questions must be consistent with the channel structure deduced by protein chemists.

In the past few years, the field of ion channels has entered into a rapid phase of development. Recently, the molecular structures of the *Streptomyces lividans* KcsA potassium channel, as well as several other potassium channels, two mechanosensitive channels, and a chloride channel, have been determined from crystallographic analyses [3–7]. It is expected that crystal structures of other ion channels will follow these discoveries. Also, as new analytical methods have been developed and the available computational power increased, theoretical models of ion permeation have become increasingly sophisticated. Now it has become possible to relate the atomic structure of an ion channel to its function, through the fundamental laws of physics operating in electrolyte solutions. Many aspects of macroscopic observable properties of ion channels are being addressed by molecular and stochastic dynamics simulations. Intuitive and hand-waving explanations of the permeation and selectivity of ions are beginning to be replaced by quantitative statements based on rigorous physical laws.

Here we give an overview of recent advances in biophysics of ion channels, placing a special emphasis on theoretical approaches that are currently under development. Computational methods of solving complex biological problems, such as permeation, selectivity, and gating mechanisms in ion channels, will increasingly play prominent roles as the speed of computers increases. Our aim in this chapter is to provide some understanding of various methods that have been proposed for treating time-dependent, nonequilibrium processes that underlie the flow of currents across biological ion channels. This review chapter is primarily devoted to the three computational approaches molecular dynamics, stochastic dynamics and continuum theories—to unravel the inner workings of biomolecules. We give intuitive explanations of the physics underlying each of the methods, referring to more comprehensive publications for mathematical details. We discuss the merits and shortcomings of each computational approach. Detailed accounts of recent experimental findings on ion channels are not given here; the reader is referred to the latest edition of Hille [8], which provides an excellent source of information in this regard.

The chapter is organized as follows. We first describe the principles underlying the continuum theories, stochastic dynamics, and molecular dynamics, stressing the strengths and weaknesses of each approach. We then discuss briefly how these computational tools have been applied in studying selectivity and permeation of ions in biological channels. We do not attempt to give an exhaustive review of the literature, which is given elsewhere [9–15]. Instead, we discuss a few selected examples to illustrate how the theories are applied in modeling of ion channels. We conclude the paper by highlighting future directions for research and identifying the problems in different approaches that need to be resolved.

2. MODELS OF ION CHANNELS

2.1. Conceptual Frameworks for Studying Ion Channels

Henri Poincaré once said: "The goal of science is order. Science is constructed from facts just as a house is constructed from stones, but an accumulation of facts is no more a science than a pile of stones is a house." This statement aptly applies to the field of ion channel

research. Thus, the ultimate aim of theoretical biophysicists has been to provide a comprehensive physical description of biological ion channels. Such a theoretical model, once successfully formulated, will link channel structure to channel function through the fundamental processes operating in electrolyte solutions. It will also concisely summarize the data, by interlacing all those seemingly unrelated and disparate observations into a connected whole. The theory will elucidate the detailed mechanisms of ion permeation—where the binding sites are in the channel, how fast an ion moves across the channel, and where the rate-limiting steps are in conduction. Finally, it will make predictions that can be confirmed or refuted experimentally.

The tools of physics that are employed in this endeavor, from fundamental to phenomenological, are *ab initio* and classical molecular dynamics, stochastic dynamics, and continuum theories. In molecular dynamics simulations, trajectories of all the atoms in a system are followed using Newton's equation of motion. In *ab initio* molecular dynamics, the interaction between the atoms are determined from first-principles electronic structure calculations. As there are no free parameters in this approach, it represents the ultimate approach to modeling of biomolecular systems. But because of the extremely demanding nature of computations, its applications are limited to very small systems at present. In classical molecular dynamics, simulations are carried out using empirically determined pairwise interaction potentials between the atoms. Although it is possible to model an entire ion channel in this way, it is not feasible to simulate the system long enough to see permeation of ions across a model channel and to determine its conductance, which is the most important channel property. For that purpose, one has to go further down to stochastic dynamics, where water molecules that form the bulk of the system in ion channels are integrated out and only the ions themselves are explicitly simulated. The continuum electro-diffusion theory of Poisson–Nernst–Planck equations makes one further simplification known as the mean-field approximation. Here, ions are treated not as discrete entities but as continuous charge densities that represent the space-time average of the microscopic motion of ions. In the Poisson–Nernst–Planck theory, the flux of an ionic species is described by the Nernst–Planck equation that combines Ohm's law with Fick's law of diffusion, and the potential at each position is determined from the solution of Poisson's equation using the total charge density (ions plus fixed charges). The Poisson–Nernst–Planck theory thus incorporates the channel structure, and its solution yields the potential, concentration, and flux of ions in the system in a self-consistent manner.

There is one other approach that has been fruitfully employed to model biological ion channels, namely, the reaction rate theory [8]. In this approach, an ion channel is represented by a series of ion binding sites separated by barriers, and ions are assumed to hop from one binding site to another, with the probability of each hop determined by the height of the energy barrier. Many useful insights have been gleaned in the past about the mechanisms of ion permeation using this approach. The merits and demerits of this theory have been debated extensively in the literature [12, 16–19], to which the interested reader is referred. We will not discuss the rate theories further in this chapter because the model parameters have no direct physical relation to the channel structure, whereas our focus is on the structure–function relationships.

2.2. Continuum Theories

2.2.1. Ohm's and Fick's Laws and Nernst Equation

The flow of ions across a channel is controlled by the potential and concentration differences on the two sides of the cell membrane. For a pore whose radius is relatively large, the current across it will increase linearly with an applied potential. Also, the current here should increase linearly with ionic concentrations in the baths surrounding the pore. In the absence of an applied potential across the pore, ions should flow from the region of a high concentration to a low concentration. The quantitative relationships between the current, applied potential, and ionic concentrations are given by Ohm's and Fick's law.

Ions in electrolyte solutions undergo random Brownian motion with an average collision time τ. When an electric field $\mathbf{E}$ is applied, an ion of mass m_i and charge e accelerates, on

the average, for a time τ, gaining a drift velocity

$$v_d = \frac{e\mathbf{E}}{m_\mathrm{i}}\tau \tag{1}$$

With n_i ions per unit volume (where n_i is known as the number density), this leads to a current density of

$$\mathbf{J} = n_\mathrm{i} e v_d = n_\mathrm{i}\frac{e^2}{m_\mathrm{i}}\tau\mathbf{E} \tag{2}$$

The relationship between the current density and the potential gradient (or the electric field) is expressed by Ohm's law

$$\mathbf{J} = -g\nabla\varphi = g\mathbf{E} \tag{3}$$

where g, the conductivity of the electrolyte solution, is $n_\mathrm{i}e^2\tau/m_\mathrm{i}$. To make contact with the more familiar expression $I = GV$, where I is the channel current, V is the membrane potential, and G is the channel conductance, we consider a cylindrical channel with radius r and length L. Assuming a uniform current density and electric field across the channel, we have $J = I/\pi r^2$ and $E = V/L$. Substituting these values in Eq. (3) yields Ohm's law with the conductance given by

$$G = \pi r^2 g/L \tag{4}$$

The physical basis of the constant of proportionality featuring in Eq. (3) can easily be understood in terms of the microscopic motion of ions in water. Noting that the mean collision time τ is related to the mean free path l and average velocity of the ions $\bar{v}$ by $\tau = l/\bar{v}$ and making use of the equipartition theorem, we can derive a simple microscopic expression for the conductivity in electrolytes:

$$g = \frac{n_\mathrm{i}}{n_\mathrm{w}}\frac{e^2}{\pi(r_\mathrm{i}^2 + r_\mathrm{w}^2)}\left(\frac{m_\mathrm{w}}{3kTm_\mathrm{i}(m_\mathrm{i} + m_\mathrm{w})}\right)^{1/2} \tag{5}$$

Here r_w and r_i denote the radius of water molecules and ions, respectively, and n is the number density of ions or water molecules, which is related to the concentration c (in moles/liter) by $n = 1000N_A c$ where N_A is Avogadro's number. As ions in electrolyte solutions are surrounded by a shell of water molecules, the effective mass and radius of an ion must include the hydration waters.

Ohm's law, simple as it may be, can provide us with useful insights about the permeation mechanisms across a transmembrane pore. As an example, we consider the gramicidin A channel, a cylindrical pore whose radius r and length L are approximately 2 Å and 25 Å, respectively. The experimentally determined conductivity of 150 mM K^+ ions is $g = 8.4 \times 10^{-3}$ S/cm in the conventional units of Siemens (S) for conductance. Substituting these values in Eq. (4), we obtain $G = 42$ pS. For an applied potential of 200 mV, the current across the pore is then expected to be 8.4 pA. This is about 3 times larger than the current measured experimentally in gramicidin A (O. S. Andersen, personal communication). This example illustrates that ion permeation across channels is not just a passive process as envisioned in Ohm's law—ions moving from one side of the membrane to the other under a uniform driving field, confined by the channel walls but not interacting with them. In fact, ions do interact with the fixed and induced surface charges on the channel walls that creates energy wells and barriers along the permeation path, the net effect of which is to attenuate the current from that of a purely passive pore. Thus, a correct calculation of the ion-channel interactions is of utmost importance in order to obtain reliable results from a permeation model.

Fick's law provides a similar relationship between the flux of ions and the concentration gradient across a channel

$$\mathbf{J}_n = -D\nabla n \tag{6}$$

where D is the diffusion coefficient, which is specific to each ion and depends on temperature and has units $m^2\ s^{-1}$. Here the subscript n denotes number flux, which is related to the current density by $\mathbf{J} = e\,\mathbf{J}_n$. The minus sign is because the movement of ions is from a region of high concentration to a region of low concentration. As shown by Einstein in 1905, the underlying physics is the same as in Ohm's law, namely, the Brownian motion of ions. The probability distribution in the location of a given particle whose initial position was known would relax as a Gaussian. That is, the shape of the probability distribution will become broader as a function of time, with its center located in the original position. The area beneath the curve, normalized to unity, represents the probability of finding the particle somewhere in the system. The mean square displacement from the initial position grows with time as $\langle \mathbf{r}^2 \rangle = 6Dt + c$ due to the fluctuations, where c, a constant, is zero for a random or Markovian evolution. In the case of ion channels, when one side of the membrane has a higher concentration than the other ($n_1 > n_2$), ions will flow to the other side with a flux, $J_n = D(n_1 - n_2)/L$, where L is the channel length.

There are impermeant anions A^- inside of a cell, but K^+ and Cl^- ions can move across the membrane via ionic channels. Whenever a charged particle is constrained in its movements, a Donnan equilibrium arises. For electroneutrality to exist in the extracellular and intracellular media, the concentrations of K^+ ions inside and outside must obey a Donnan relationship of the form:

$$[K]_i^2 = [K]_o^2 + [A][K] \tag{7}$$

where the subscripts i and o denote inside and outside, respectively. Thus, in the living cell, the concentration of K^- ions is higher inside than outside and the other way around for Cl^- ions. Also, the asymmetrical distribution of ions across the cell wall gives rise to the membrane potential, which is typically about 70 mV negative inside with respect to outside. Thus, there are both potential and concentration gradients driving the ions across an ion channel. This situation is described by the Nernst–Planck equation, also known as the Nernst transport equation, that combines Ohm's and Fick's laws

$$\mathbf{J}_n = -D\nabla n - \frac{g}{e}\nabla\phi = -D\left(\nabla n + \frac{ne}{kT}\nabla\phi\right) \tag{8}$$

In writing this expression, we make use of the Einstein relation, $g = ne^2D/kT$, which relates the conductivity to the diffusion coefficient. Although the Nernst–Planck equation is primarily used to describe current flow, in the special case of a vanishing current, it makes an important statement about the electrochemical equilibrium in cells. Using $\mathbf{J}_n = 0$ in Eq. (8) and integrating once, we obtain the celebrated Nernst equation

$$\phi_1 - \varphi_2 = -\frac{kT}{e}\ln(n_1 - n_2) = -59\log\frac{c_1}{c_2}(\text{mV}) \tag{9}$$

that gives the potential difference required to maintain the equilibrium when the concentrations are different on the two faces of the membrane. The numerical factor in Eq. (9) is obtained using $T = 298$ K. In practice, the Nernst equation is often used to estimate the membrane potential generated by asymmetric solutions in cells. It predicts about a 59 mV change in potential for a 10-fold increase in $[K]_o$.

2.2.2. Poisson–Boltzmann Theory

In recent years, two continuum theories of electrolytes have been fruitfully applied for studying membrane ion channels (for reviews, see Refs. [9, 12, 13, 20]). The so-called Poisson–Boltzmann theory and Poisson–Nernst–Planck theory were originally developed early in the 20th century for bulk electrolytes, and their validity has been firmly established since then [21]. The Poisson–Boltzmann theory has become an important tool for studying proteins and membranes, leading to many insights on the key role played by electrostatic interactions [22]. In ion channels, this theory was initially used to include the effects of ionic atmosphere on the potential energy profile of an ion in schematic channels [23–25]. More recently,

the Poisson–Boltzmann calculation of potential energy profiles has been extended to realistic channel structures in numerous articles [26–35].

The Poisson–Boltzmann theory provides a classical electrostatic description of a system in which fixed external charges, represented by a density ρ_{ex}, are surrounded by mobile ions in a dielectric medium. At equilibrium, the distribution of mobile ions in the system is given by a continuous charge density ρ_{el}, given for monovalent ions, by the Boltzmann factor

$$\rho_{el} = \sum_{\nu} e n_{0\nu} \exp\left[\frac{-e\phi}{kT}\right] \tag{10}$$

where $n_{0\nu}$ is the reference number density of ions of species ν. The average electric potential $\phi(\mathrm{r})$ featuring in Eq. (10) is obtained from the solution of Poisson's equation

$$\varepsilon_0 \nabla \cdot [\varepsilon \nabla \phi] = -\rho_{el} - \rho_{ex} \tag{11}$$

By combining Eq. (10) and Eq. (11), we obtain the following Poisson–Boltzmann equation:

$$\varepsilon_0 \nabla \cdot [\varepsilon \nabla \phi] = 2 e n_0 \sinh\left[\frac{-e\phi}{kT}\right] \tag{12}$$

This equation cannot be solved analytically, except for a few special cases. To simplify the problem, we make the assumption that the interaction between the ions is small compared with the thermal energy of the ions. That is, we assume $\sinh[e\phi/kT] \ll 1$ and $\sinh[e\phi/kT] \approx [e\phi/kT]$. Then, Eq. (12) for a bulk electrolyte with no fixed charges (i.e., $\rho_{ex} = 0$) becomes

$$\nabla^2 \phi = \kappa^2 \phi \tag{13}$$

where $1/\kappa$ is the Debye screening length or Debye radius, given by

$$\frac{1}{\kappa} = \sqrt{\frac{\varepsilon_0 \varepsilon kT}{2e^2 n_0}} \tag{14}$$

Equation (14) is a linearized form of the Poisson–Boltzmann equation proposed by Debye and Hückel [36]. This equation is easy to solve with the boundary conditions that as $\mathbf{r} \to \infty$, $\phi \to 0$. At room temperature (T = 298 K) in water ($\varepsilon = 80$), the Debye length is related to concentration as $\kappa^{-1} = 3.07/\sqrt{c_0}$ Å. For $c_0 = 0.15, 0.30, 0.50$, and 1.00, the Debye lengths are, respectively, 7.9, 5.6, 4.3, and 3.1 Å. The Debye–Hückel theory provides many intuitive pictures and useful insights on the behavior of electrolyte solutions. The solution of Eq. (13) gives the following screened Coulomb potential around a central ion of diameter a:

$$\phi = \frac{e \exp[-\kappa(r-a)]}{4\pi\varepsilon_0 \varepsilon (1+\kappa a) r} \tag{15}$$

The radial density of the screening charge $p(r)$ is proportional to this potential

$$p(r) = 4\pi r^2 \rho_{el} = -4\pi r^2 \varepsilon_0 \varepsilon \kappa^2 \phi = \frac{-e\kappa^2}{1+\kappa a} r \exp[-\kappa(r-a)] \tag{16}$$

In words, when a cation is located at a fixed point, the density of anions around it increases, peaking at one Debye length or $r = \kappa^{-1}$, and then decays exponentially to the background number density. By integrating Eq. (16), we can deduce how big a sphere needs to be to shield the effect of a counter charge located at the origin. The volume integral of this shielding charge is given by

$$q(r) = -\left[1 - \frac{1+\kappa r}{1+\kappa a} \exp[-\kappa(r-a)]\right] \tag{17}$$

revealing that $-q(r)/e$ increases monotonically with r. A sphere of $r = 1/\kappa$ will contain an excess counter charge about 0.25 e, whereas a sphere with $r = 3/\kappa$ will contain an excess charge of 0.80 e. It is important to note that, for a $c_0 = 150$ mM electrolyte under bulk conditions, a length scale of ≈30 Å is required for nearly complete screening of an ionic charge.

2.2.3. Poisson–Nernst–Planck Theory

The Poisson–Boltzmann theory discussed in the previous section is limited to equilibrium situations. To describe nonequilibrium processes, such as ion transport, another continuum theory that is widely known as the Poisson–Nernst–Planck theory is used. This theory, which combines the drift-diffusion equation given in Eq. (8) and Poisson's equation given in Eq. (11), provides a premium description of ion transport problems in many branches of physics and chemistry [21, 37–40]. In recent years, the theory has also been fruitfully applied in ion channels, especially by Eisenberg and his colleagues [41–47]. Here we give a brief outline of the theory and refer to the recent articles by Eisenberg [12, 13] and others [9, 15, 20, 48] for further details and references.

When ions move across narrow channels, they interact with the charge groups on the protein walls, and the electric potential at any given position changes due to their motion. To account for these effects, the potential φ on the right-hand side of Eq. (8) has to be calculated from Poisson's equation. In the Poisson–Nernst–Planck theory, these two equations are solved simultaneously, yielding the potential, concentration, and flux of ions in the system. Here, the flux of ions is described by a continuous quantity corresponding to macroscopic averages of microscopic motion of individual ions.

Due to their nonlinear nature, the two coupled equations are notoriously difficult to solve analytically, except for a few special cases, such as the classical Goldman–Hodgkin–Katz equation [8]. For recent discussions of the analytical treatment of the Poisson–Nernst–Planck equations, the reader is referred to Syganow and von Kitzing [49–51].

When $\mathbf{J}_\nu = 0$ in the drift-diffusion equation,

$$\mathbf{J}_\nu = -D_\nu\left(\nabla n_\nu + \frac{en_\nu}{kT}\nabla\phi\right) \tag{18}$$

then, the Poisson–Nernst–Planck equations trivially reduce to the Poisson–Boltzmann equation with the density given by the Boltzmann factor,

$$n_\nu = n_{0\nu}\exp(-\psi_\nu), \qquad \psi_\nu = \frac{e\phi}{kT} \tag{19}$$

where $n_{0\nu}$ denotes a reference density and ψ_ν is the potential energy expressed in a dimensionless form. Using Eq. (19) for n_ν as an integrating factor in Eq. (18), it can be rewritten as

$$\mathbf{J}_\nu = -D_\nu\exp(-\psi_\nu)\nabla[n_\nu\exp(\psi_\nu)] \tag{20}$$

Let the number densities, $\eta_\nu = n_\nu\exp(\psi_\nu)$, at the boundary points $z = 0$ and L be $\eta_{\nu 0}$ and $\eta_{\nu L}$. Under steady-state conditions and assuming a uniform flux $\mathbf{J}_\nu$ in the z direction, Eq. (20) reduces to 1-D and integrating it from 0 to L gives

$$J_\nu = -D_\nu\frac{\eta_{\nu L} - \eta_{\nu 0}}{\int_0^L \exp[\psi_\nu(z)]\,dz} \tag{21}$$

If one assumes that the potential drops linearly from $z = 0$ to L, Eq. (21) integrates easily and gives the Goldman–Hodgkin–Huxley equation [8]. A similar expression for the density can be obtained by integrating Eq. (20) from 0 to z and using Eq. (21) to eliminate J_ν/D_ν

$$n_\nu(z) = \exp[-\psi_\nu(z)]\left[\eta_{\nu 0} + (\eta_{\nu L} - \eta_{\nu 0})\cdot\frac{\int_0^z \exp[\psi_\nu(z)]\,dz}{\int_0^L \exp[\psi_\nu(z)]\,dz}\right] \tag{22}$$

Finally, substituting Eq. (22) in Poisson's equation, we obtain an Poisson–Nernst–Planck expression for the potential

$$\varepsilon_0\frac{d}{dz}\left[\varepsilon(z)\frac{d}{dz}\phi(z)\right] = -\sum_\nu e\exp[-\psi_\nu(z)]\left[\eta_{\nu 0} + (\eta_{\nu L} - \eta_{\nu 0})\frac{\int_0^z \exp[\psi_\nu(z)]\,dz}{\int_0^L \exp[\psi_\nu(z)]\,dz}\right] - \rho_{\text{ex}} \tag{23}$$

There are no known analytical solutions of Eq. (23). With the advent of high-speed computers, the Poisson–Nernst–Planck equations can readily be solved numerically, enabling us to compute the current across ion channels [12, 44]. The Poisson–Nernst–Planck theory is perhaps the simplest form of a nonequilibrium theory that takes into account the shape of the channel, the magnitude and location of charge residues in the channel protein, and the applied electric field and asymmetrical ionic concentrations in the two sides of the channel.

To calculate the current across a channel, it is placed in a simulation system, and a reservoir with a fixed number of ions is attached at each end of the channel. The simulation system is then divided into small rectangular grids, and the Poisson–Nernst–Planck equations are solved at grid points using a finite difference algorithm [44, 48]. The grid size has to be optimized for efficient running of the program. A smaller grid size improves accuracy of the results but also takes a much longer computational time. The required inputs for the algorithm are (i) the channel shape, (ii) the dimensions of the reservoirs and ionic concentrations in each reservoir, (iii) the dielectric constant of the protein and the solution, (iv) the locations and strengths of charges on the channel wall, (v) the membrane potential, and (vi) the diffusion coefficients of cations and anions. Once these parameters are specified, the solutions of the Poisson–Nernst–Planck equations give the concentration and potential throughout the system as well as the ionic currents through the channel.

2.2.4. Modification of the Continuum Theories

The expression for the Debye shielding given in Eq. (16) provides an intuitive guide to the range of validity of the Poisson–Nernst–Planck theory and where and how it fails. An ion near the protein induces surfaces charges of the same polarity on the protein–water interface. When a cation in an electrolyte solution is placed near a slab of protein, water molecules near the ion align themselves such that the oxygen atoms, with their partial negative charges, are positioned nearest to the ion. Because polar or carbonyl groups on the protein wall cannot rotate as freely as water molecules, there will be excesses of hydrogen atoms at the water–protein interface. Viewed from the ion, these excess hydrogen atoms at the boundary appear as surface charges, exerting a repulsive force on it. Macroscopically, we say that a charge q located at a distance d from a slab of protein surface induces surface charges on the dielectric boundary. For an idealized infinite plane, the magnitude of repulsive force this ion experiences is the same as when we place another charge q', at the other side, at a distance d from the surface, and remove the boundary. The magnitude of this image charge q' is related to the relative permittivities of the protein ($\varepsilon_p = 2$) and water ($\varepsilon_w = 80$), given by

$$q' = \frac{\varepsilon_w - \varepsilon_p}{\varepsilon_w + \varepsilon_p} q \tag{24}$$

As the ion comes nearer to the boundary, the repulsive image force it experiences grows as d^2. A similar repulsive force acts on an ion that is about to enter an ion channel. Only, the force is more than an order of magnitude larger in this case because the dielectric boundary is now wrapped around the ion, enhancing the effect. Thus, an ion entering a pore formed by membrane proteins encounters an energy barrier due to the induced surface charges, the height of which increases rapidly with decreasing radius of the pore. This energy barrier, sometimes called self-energy or reaction field, plays an important role in determining permeation properties of ions across a narrow pore. For example, saturation of conductance cannot be explained if one ignores the self-energy barrier of ions. One of the shortcomings of the Poissson–Nernst–Planck theory is in its failure to calculate correctly the magnitude of the induced surface charges and the resulting self-energy barriers.

If the dimensions of the system one is dealing with is much larger than the Debye length, the Poisson–Nernst–Planck theory will give accurate results. As an example, consider ion diffusion across a cylindrical channel whose radius is 30 Å. The charge of an ion near the central axis of the pore will completely be screened by the counterions, so that there will be no induced surface charges on the water–protein boundary due to this ion. Thus, no self-energy barriers will be encountered by the permeating ions. In this situation, the Poisson–Nernst–Planck theory will correctly predict the current across the pore under various driving forces.

Now, let us consider a similar cylindrical channel with a radius of 3 Å, spanning a 30 Å-thick membrane, whose volume is $\sim 10^3$ Å^3. At physiological concentrations, an anion or a cation is expected to be in this pore only 10% of the time on average. As an ion enters the pore, it induces surface charges of the same polarity, which exert a repulsive force on it, pushing it out. Normally, there are no counterions in the pore to screen its charge and hence cancel the repulsive force. In the Poisson–Nernst–Planck theory, the simulation system is divided into small cubic cells with a volume, say, 1 Å^3, each of which contains 10^{-4} of a cation and an equal fraction of an anion. The effect of the fractional charge in each grid on the protein wall is completely screened by the equal and opposite fractional charge present in it. These fractional charges diffuse across the pore, one cubic grid to the other, under the influence of the membrane potential, unencumbered by any induced surface charges on the protein boundary. In short, the ion–protein interaction, which is the dominant force in the process of ion permeation across a narrow pore, is completely ignored in the Poisson–Nernst–Planck theory.

Detailed studies comparing Poisson–Nernst–Planck theory with Brownian dynamics [48] and lattice Monte Carlo simulations [52] have revealed that the Poisson–Nernst–Planck theory can reliably be applied to study the permeation process across pores whose radius is about 2 Debye lengths (or 16 Å for a 150 mM solution). The magnitude of errors increases rapidly as the radius of the pore becomes smaller. Thus, application of the continuum theories to biological ion channels, which have radii much smaller than 2 Debye lengths, is not justified. A second problem in this respect is how to treat the ion–ion interactions in the Poisson–Nernst–Planck theory, which are known to play an important role in multi-ion channels such as potassium and calcium channels. These problems need to be resolved satisfactorily before this theory can be used to study the structure–function relations in ion channels.

Given the computational simplicity of the continuum theories compared to simulation approaches and their widespread use, it would be desirable to find a solution to the problem of dielectric self-energy highlighted above. A possible approach is to include an explicit self-energy term in the formalism that would mimic the effect of the induced surface charges on ions entering the channel. Such a term would prevent the buildup of large counterion concentrations around a test ion and may eradicate the spurious shielding effects seen in the continuum models. Indeed, there have been several attempts to improve the accuracy of the standard Poisson–Boltzmann and Poisson–Nernst–Planck theories by including a specific dielectric self-energy term [53–57]. Near a water–protein interface, a mobile monovalent ion with charge e induces polarization charges of the same sign on the boundary [see Eq. (24)]. These charges, in turn, generate a reaction potential ϕ_R that acts to repel the ion from the boundary. The potential energy due to this reaction field, called the dielectric self-energy, is given by

$$U_{\nu R} = \frac{1}{2} z_\nu e \phi_R(\mathbf{r}) \tag{25}$$

Because ϕ_R is itself proportional to e, $U_{\nu R}$ depends on the square of the ionic charge, and hence it is always positive regardless of the valence of ions. Thus, the dielectric self-energy contribution to the total potential energy of an ion is the same for cations and anions. This of course is incompatible with treatment of the mobile ions in the Poisson–Boltzmann theory as a continuous charge density distributed according to the Boltzmann factor

$$n_\nu(\mathbf{r}) = n_{0\nu} \exp\left(\frac{-U_\nu}{kT}\right), \qquad U_\nu = z_\nu e \phi(\mathbf{r}) \tag{26}$$

Thus, the Poisson–Boltzmann equation cannot lead to a suppression of ionic densities near a dielectric boundary because it fails to take into account the dielectric self-energy distribution. In theory, the lack of dielectric self-energy in the Poisson–Boltzmann equation can be remedied by adding Eq. (25) to Eq. (26) such that

$$n_\nu(\mathbf{r}) = n_{0\nu} \exp\left[\frac{-(U_\nu + U_{\nu R}}{kT}\right] \tag{27}$$

The modified Poisson–Boltzmann equation then becomes

$$\varepsilon_0 \nabla \cdot [\varepsilon(\mathbf{r})] = 2en_{0_\nu} \sinh\left[\frac{e\phi(\mathrm{r})}{kT}\right] \exp\left[\frac{-U_R}{kT}\right] - \rho_{\mathrm{ex}} \tag{28}$$

As an ion approaches a dielectric boundary, U_R grows rapidly, and the exponential factor in Eq. (28) provides a natural mechanism to suppress the ion densities. For a single ion, the self-energy is well defined. We may first solve Poisson's equation for the single ion and substitute the computed reaction potential in Eq. (25). In a dilute electrolyte solution, where the effect of the reaction field created on one ion by another can be neglected, this simple recipe should be quite adequate for the self-energy correction. However, how to calculate U_R in a many-body system in a self-consistent manner is problematic. At higher concentrations, the approximation of the reaction potential with that of a single ion becomes less accurate. Incorporating the effect of the reaction field created by one ion on another ion is a difficult problem that poses a formidable theoretical challenge.

The Poisson–Nernst–Planck equations can be modified in a similar manner to the Poisson–Boltzmann equation by including a specific dielectric self-energy term in the potential energy of an ion:

$$\mathbf{J}_\nu = -D_\nu\left[\nabla n_\nu + \frac{z_\nu e n_\nu}{kT}\nabla\left(\frac{\phi + \phi_R}{2}\right)\right] \tag{29}$$

The analogy between Eq. (29) and the modified Poisson–Boltzmann equation [Eq. (28)], can be seen most clearly when the current vanishes. Then, Eq. (29) can be easily integrated yielding the modified Boltzmann factor given in Eq. (27).

2.3. Stochastic Dynamics

2.3.1. Langevin Equation

Of the several tools in statistical mechanics that treat the dynamics of nonequilibrium systems, the most widely known is perhaps the theory of Brownian motion. The behavior of an ion in an electrolyte solution undergoing a random type of motion can be described by the dynamical equation of motion in classical mechanics, known as the Langevin equation. The simplest form of stochastic dynamics, which deals with many-particle systems such as liquids and solutions, is Brownian dynamics. Brownian motion is triggered by the presence of a background noise or fluctuations, and the energy gained by a Brownian particle is dissipated in the medium.

When an impulsive force is imparted on a macroscopic particle with mass m in a fluid medium, its subsequent motion is given by Newton's equation of motion

$$m\frac{d\mathbf{v}}{dt} = -m\gamma\mathbf{v} \tag{30}$$

where $m\gamma$ is the friction coefficient, which is roughly proportional to the viscosity of the medium and the radius of the particle. The integral of Eq. (30) is simply given by $\mathbf{v} = \mathbf{v}_0 \exp(-\gamma t)$. Thus, the velocity of the particle exponentially decays to zero due to the frictional force. In other words, the energy of the particle is dissipated to the surrounding molecules in the fluid. For an ion in water, however, the situation is different because it has a similar mass as water molecules. The mean squared velocity of the ion in thermal equilibrium does not decay but remains at 3 kT/m (where k and T are the Boltzmann constant and temperature in Kelvin). This background motion of the ion is brought about by random forces, caused by incessant collisions with the surrounding molecules. Thus, a random or fluctuation force $\mathbf{F}_\mathrm{R}$ needs to be added to the right-hand side of Eq. (30) to account for the motion of an ion performing Brownian motion

$$m\frac{d\mathbf{v}}{dt} = -m\gamma\mathbf{v} + \mathbf{F}_\mathrm{R} \tag{31}$$

Equation (31), known as the Langevin equation, is the fundamental equation that describes the random motion of ions in an electrolyte solution. Both the dissipative and fluctuating

forces stem from the same underlying mechanisms, namely, the random bombardment of ions by water molecules in thermal motion, and their interrelationship is described by the fluctuation–dissipation theorem of statistical mechanics [58, 59].

The above description of the Langevin equation applies to ions freely diffusing in water. For ions in the vicinity of a channel, there is an additional, systematic force that influences their motion, namely, the electric force. It originates from four different sources. First, there is the electric field resulting from the membrane potential. Second, there are fixed charges in the channel protein, and the electric field emanating from them will add to the field generated by the membrane potential. Third, charges carried by all the ions in electrolyte solution contribute to the total electric field. Finally, whenever any of these ions comes near the protein wall, it induces surface charges of the same polarity at the water–protein interface. This last component of the force exerted on an ion plays a crucial role in influencing the motion of an ion attempting to traverse across a narrow pore formed by the protein wall. Each of these four components of the electric force acting on an ion needs to be computed, summed, and added as a third term to the right-hand side of Eq. (31).

For the basic steps in the solution of the Langevin equation and the implementation of the equation in the Brownian dynamics algorithm, see Refs. [60–62]. When the random force featuring in Eq. (31) cannot be considered uncorrelated in time, as is required in the Brownian dynamics approach, then it becomes necessary to invoke the concept of memory function, and the resulting equation is known as the generalized Lagevin equation [59]. Algorithms for generalized Langevin dynamics are given in Refs. [63, 64].

2.3.2. Brownian Dynamics Simulations in Ion Channels

To carry out Brownian dynamics simulations of ion channels, one needs to specify the boundaries of the system. This is a relatively simple problem for one-dimensional Brownian dynamics simulations [9, 65, 66], but requires addition of reservoirs to the channel system in the more realistic case of three-dimensional Brownian dynamics simulations. Here we describe a simple stochastic boundary that has been used successfully in applications of Brownian dynamics simulations to a number of ion channels [67–72].

Figure 1 shows a schematic illustration of a Brownian dynamics simulation assembly. An ion channel representing the potassium channel is placed at the center of the assembly. The positions of all the atoms forming the channel are give by its x-ray structure, and the charge on each atom is assigned. Then, a large reservoir with a fixed number of K^+ (or Na^+) and Cl^- ions is attached at each end of the channel (Fig. 1A). The membrane potential is imposed by applying a uniform electric field across the channel (Fig. 1B). This is equivalent to placing a pair of large plates far away from the channel and applying a potential difference between the two plates. Because the space between the electrodes is filled with electrolyte solutions, each reservoir is in isopotential. That is, the average potential anywhere in the reservoir is identical to the applied potential at the voltage plate on that side. A potential drop thus occurs across the channel. When an ion strikes the reservoir boundary during simulations, it is elastically scattered back into the reservoir. This operation is equivalent to letting an ion enter the reservoir whenever one leaves the simulation system. Thus, the concentrations of ions in the reservoirs are maintained at the desired values at all times. During simulations of current measurements, the chosen concentration values in the reservoirs are maintained by recycling ions from one side to the other whenever there is an imbalance due to a conduction event. This process mimics the current flow through a closed circuit.

The number of ions that must be placed in each reservoir for a chosen concentration depends on the size of the reservoir. Because the computational cost is directly proportional to the number of ions in the simulation system, it is desirable to have a small reservoir. At the same time, it must be large enough such that the ions in the system are in conditions similar to those in bulk electrolyte solutions. For example, the number of ions near the entrance of the pore should fluctuate according to the binomial distribution. To meet these requirements, an elaborate treatment of boundaries using a grand canonical Monte Carlo method was proposed [73]. Subsequently, Corry et al. [74] showed that, provided the dimensions of the reservoirs are about 3–4 Debye lengths, the simple stochastic boundary as described above gives the same results as the more sophisticated method proposed by Im et al. [73].

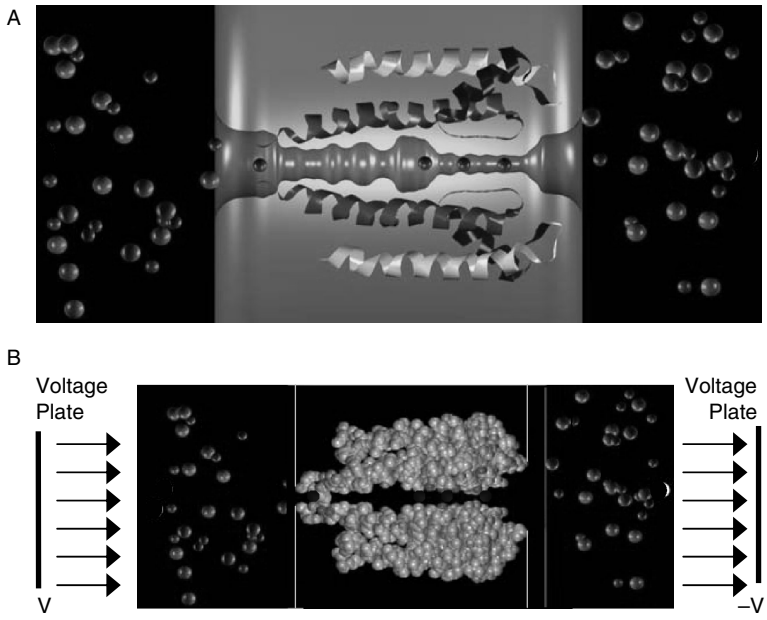

Figure 1. Simulation system using the model potassium channel. (A) Two of the four subunits of the full experimentally determined KscA potassium channel are embedded in a medium of a low dielectric medium, representing the lipid bilayer. To carry out Brownian dynamics, a large reservoir containing a fixed number of K^+ and Cl^- ions is connected to each end of the channel. (B) The potential across the channel is created by applying a constant electric field. This is equivalent to applying a potential difference across two plane plate, located at a long distance away from the channel. Reprinted with permission from [71], S. H. Chung et al., *Biophys. J.* 82, 628 (2002). © 2002, Biophysical Journal.

In Brownian dynamics simulations, the Langevin equation is solved repeatedly to trace the trajectory of every ion in the assembly. Snapshots of the simulation system are taken at short time intervals for millions of time-steps. At each time-step, the Langevin equation is integrated to obtain the velocity of each ion to determine to which position the ion will move in the next time-step. Once the magnitude and direction of the force acting on each ion is computed, then one can determine which position each ion would have moved to in a short time interval. The new coordinates of all ions in the assembly are deduced, and the calculation is repeated. By repeating this process for a sufficiently long period of time, usually many microseconds, one can deduce how many ions move across the channel in a fixed period of simulation time. Because of the random and frictional forces featuring in the Langevin equation, the procedure for integrating Eq. (31) to obtain the velocity and position of the particle is somewhat complicated. For the detailed methods for integrating the Langevin equation, the reader is referred to Hoyles et al. [62] and Kuyucak et al. [15].

The choice of the time-step is very important for the reliability of Brownian dynamics simulations. If the time-step is chosen too short, the number of times the Langevin equation needs to be solved for a given simulation time increases. On the other hand, the accuracy is compromised if the time-step is too long, although the computational cost is reduced. To understand how a particle undergoing Brownian motion behaves, we integrate Eq. (31) twice to obtain the expression for the mean square displacement [58]

$$\langle x^2 \rangle = \frac{2kT}{m\gamma} t - \gamma^{-1}[1 - \exp(-\gamma t)] \tag{32}$$

Here γ^{-1} is the relaxation time constant, which corresponds to the time required for a particle that is suddenly displaced to relax back to the original equilibrium position. For K^+ and Cl^-, γ^{-1} is about 30 fs. If we look at a potassium ion once every hundred of fs, (t is much larger than γ^{-1}), its mean square displacement becomes proportional to t

$$\langle x^2 \rangle = \frac{2kT}{m\gamma} t \tag{33}$$

In other words, the ion behaves like a diffusing particle executing a random walk. In contrast, if we examine the same ion at short time intervals, say a few fs (t is much smaller than γ^{-1}), the mean square displacement is

$$\langle x^2 \rangle = \frac{kT}{m} t^2 \tag{34}$$

That is, the ion in a short initial time interval behaves like a free particle moving with the constant thermal velocity of $(kT/m)^{1/2}$.

In implementing the Brownian dynamics algorithm for ion channels, we need to consider the behavior of ions in these short and long time intervals. When the force experienced by an ion is changing rapidly, as it is when the channel geometry undergoes sudden changes, it is desirable to use a short time step of 1–2 fs. On the other hand, a long time-step of up to 100 fs can be used in the reservoirs with no loss of accuracy. In the algorithm of Chung et al. [69], a short time step of 2 fs is used when an ion is in the channel region where the force is expected to change rapidly, and a long time step of 100 fs is used when an ion is elsewhere. If an ion is in the channel at the beginning of a 100-fs period, it is simulated by 50 short time-steps instead of one long time-step; so synchronization among the ions is maintained. One can simplify the algorithm by omitting the inertial term $m[d\mathbf{v}/dt]$ from Eq. (31) and take time-steps larger than the relaxation time constant. Because of its simplicity, this form is sometimes used in the literature [73]. Its applicability to ion channels, however, is limited because the rapidly changing forces inside a channel demand use of short time steps.

2.3.3. Validation of the Brownian Dynamics Algorithm

The behavior of the interacting ions deduced from the Brownian dynamics simulations accords with physical reality. Figure 2 shows the mean square displacement $\langle x^2 \rangle$, the velocity distribution, and the velocity autocorrelation function $\langle v(0)v(s) \rangle$ obtained from one simulation lasting 500,000 time-steps. Theoretically, $\langle x^2 \rangle$ should be a linear function of time as given in Eq. (33). The measured slopes for Na^+ and Cl^- shown in Fig. 2A (solid lines) are about 7% lower than the predicted values for a bulk solution, which is due to ions scattering back from the boundary, retarding their free diffusion. The velocity distributions of Na^+ and Cl^- in the system are shown in Fig. 2B. From the equipartition theorem, these distributions should be Maxwellian. The measured distributions (circles) match closely those computed from the theoretical distribution (solid lines). Theoretically, the velocity autocorrelation function should be of the form:

$$\langle v(0)v(s) \rangle = \frac{kT}{m} \exp(-\gamma |s|) \tag{35}$$

Thus, regardless of the initial velocity, the successive velocities will be correlated over a time interval on the order of γ^{-1}, the relaxation time constant of the ion. The measured functions (circles) shown in Fig. 2C decay exponentially, as predicted from Eq. (35) (solid lines). Thus, we conclude that Brownian dynamics simulations can faithfully characterize the motion of ions in a solution confined to a small reservoir.

2.3.4. Uses of Brownian Dynamics in Ion Channels

The ability to compute current flow across ion channels confers a distinct advantage to Brownian dynamics simulations compared to other simulation techniques. Thus, two obvious applications of Brownian dynamics in ion channels are in calculation of the current–voltage and conductance–concentration curves, which can directly be compared to the physiological measurements to assess the reliability and predictive power of the method. By simulating a mixture of ions, one can also study selectivity ratios of ions. Because ions with the same valence are treated on an equal footing in Brownian dynamics, this can be used in a straightforward manner only in studies of valence selectivity. For monovalent ions, one has to supplement the potential profiles of ions with free-energy differences obtained from molecular dynamics simulations.

In addition to simple counting of ions crossing the channel, one can carry out a trajectory analysis of ions in the system to determine their average concentrations. This is useful in

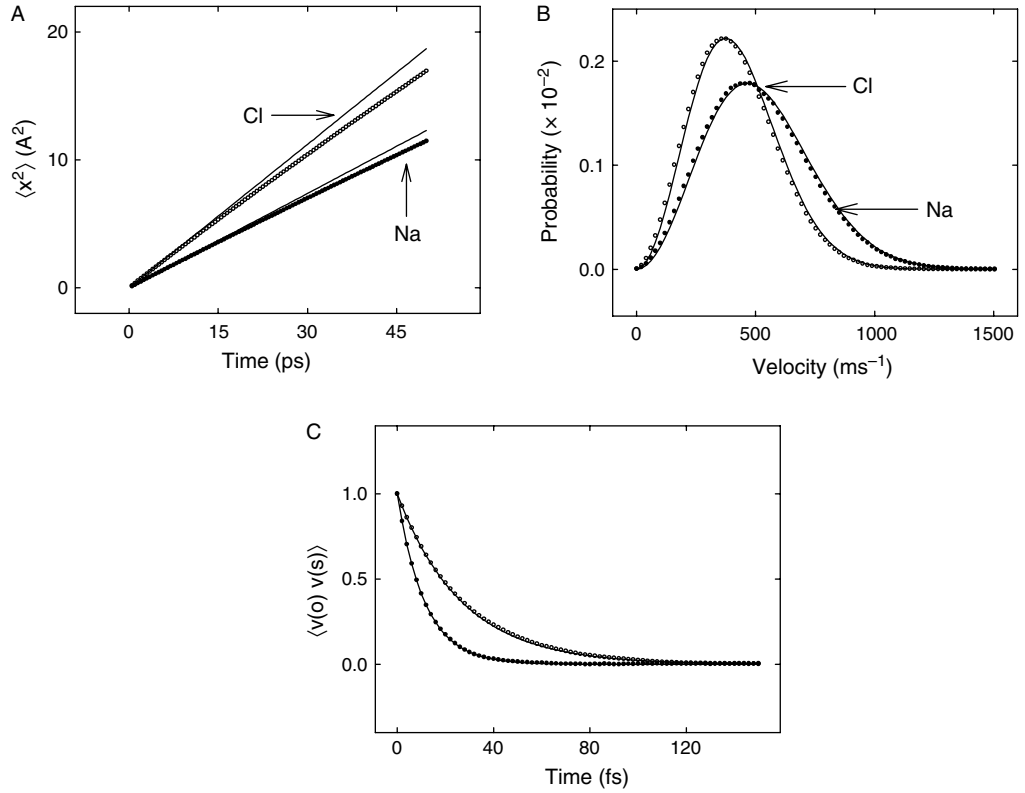

Figure 2. Validation of the Brownian dynamics algorithm. Results of the Brownian dynamics simulations are indicated by open circles for chloride ions and filled circles for sodium ions. (A) The mean-square displacements of ions measured during a simulation period is compared with the diffusion formula, $\langle x^2 \rangle = 2D\ t$ (solid line). (B) The velocity distributions of ions are compared with the Maxwellian distribution (solid line) (C) Comparison of velocity autocorrelation functions of ions with Eq. (35). Reprinted with permission from [67], S. C. Li et al., *Biophys. J.* 74, 37 (1998). © 1998, Biophysical Journal.

finding the binding sites and the average number of ions in the channel, both of which are experimentally observable quantities. Blocking of channels by larger molecules or divalent ions can be studied in a similar manner in Brownian dynamics. A prime example is the mole fraction effect, where increasing concentration of one type of ions leads to a reduction in the conductance of another. More refined analysis of Brownian dynamics trajectories can reveal the important transitions that take place during conduction events. This would be very important in interpreting the results of simulations in terms of the rate theories. Alternatively, one can animate the trajectories of ions obtained from the Brownian dynamics simulations and directly watch the permeation of ions in real space-time.

2.3.5. Limitations of Brownian Dynamics

Brownian dynamics makes one very important simplifying assumption. That is, water is treated not explicitly but as continuum. This is both the strength and the limitation of the method. With this simplification, it is possible to trace the trajectories of about 100 ions interacting with a dielectric boundary for hundreds of microseconds, a period long enough to deduce the conductance of an ion channel. A crucial issue is whether such a continuum approximation in a narrow, biological nanotube can be justified or not. Molecular dynamics studies of water confined in narrow pores have shown that the boundary imposes an order on the water molecules reducing their polarizability significantly [75–78]. From these studies, it appears that one should use very low values of ε for channel waters in solving Poisson's equation. The role of the dielectric constant in this context, however, is simply to reduce its field by $1/\varepsilon$. Thus, in choosing an effective ε value for channel waters, one has to consider by how much the screening of an ion's field is reduced in a channel compared to the bulk

environment. As long as the first hydration shell of ions remains intact in a channel, use of continuum electrostatics with an ε closer to the bulk value may be justified. This criterion is generally satisfied in biological ion channels, including the narrow selectivity filter regions where protein atoms substitute for water completing the solvation shell. A justification of these ideas and extraction of effective ε values from molecular dynamics simulations or otherwise remain as future problems.

In Brownian dynamics, it is assumed that the water–protein interface is rigid and that the positions of atoms forming the channel do not change. Proteins forming channels are certainly not static, but whether their motion or flexibility plays an important role in ion permeation is not known. Such motions are unlikely to be relevant, as large conformational changes of proteins is a much slower process than ion permeation. Nevertheless, the effects of structural polarizability on the dynamics of ion permeation needs to be explored both experimentally and from molecular dynamics simulations. If found to be important, some of the motions of the protein, such as the bending of carbonyl groups, can readily be incorporated in Brownian dynamics modeling of ion channels.

Finally, as pointed out above, size-dependent selectivity among ions with the same valence cannot be understood within the Brownian dynamics framework, and one has to appeal to molecular dynamics or semimicroscopic Monte Carlo simulations [79] for that purpose.

2.4. Molecular Dynamics

2.4.1. General Formalism

Molecular dynamics has now become one of the important tools in modeling of biomolecular systems [80], and availability of several user-friendly packages such as AMBER [81], CHARMM [82], GROMOS [83], and GROMACS [84] have made the method accessible to any researcher. With the increasing speed of modern computers, it may eventually become possible to study the biological processes at a microscopic level and relate the function of a biological ion channel to its underlying molecular structure.

In molecular dynamics simulations, we follow the trajectories of N particles interacting via a many-body potential $V(\mathbf{r}_1, \mathbf{r}_2, \ldots, \mathbf{r}_N)$ using Newton's equation of motion:

$$m_i \frac{d^2\mathbf{r}_i}{dt^2} = \mathbf{F}_i \tag{36}$$

where m_i and $\mathbf{r}_i$ denote the mass and position of the ith particle, and the force on it is given by the gradient of the potential V. Because all the atoms in the system (including water molecules) are represented explicitly in molecular dynamics, there are no frictional or random forces to deal with as in stochastic dynamics. This makes the integration of Eq. (36) rather trivial—given the positions and velocities of the particles at time t, at a later time $t + \Delta t$ they are updated to

$$\begin{aligned} \mathbf{r}_i(t + \Delta t) &= \mathbf{r}_i(t) + \mathbf{v}_i(t)\Delta t + \frac{\mathbf{F}_i(t)}{2m_i}\Delta t^2 \\ \mathbf{v}_i(t + \Delta t) &= \mathbf{v}_i(t) + \frac{\mathbf{F}_i(t)}{m_i}\Delta t \end{aligned} \tag{37}$$

although in practice more sophisticated algorithms are typically used. At every time step, the potential function is recalculated using the new positions of the particles, and this process is iterated for a number of steps until a statistically satisfactory data set is generated. The trajectory data thus generated are stored at certain intervals, which are analyzed later to determine the structural and dynamical properties of a system. Quantities such as free energy, mean square displacement, radial distribution, and other correlation functions are calculated from an ensemble average over several simulations or parts of a long simulation.

The interactions between all atoms in the system are described by empirical potentials. An example of a frequently used potential function is:

$$V(\mathbf{r}^N) = \sum_{\text{bonds}} \frac{k_i}{2}(l - l_{i,0})^2 + \sum_{\text{angles}} \frac{k_i}{2}(\theta_1 - \theta_{i,0})^2 + \sum_{\text{torsions}} \frac{V_n}{2}[1 + \cos(n\omega - \gamma)] + \sum_{i=1}^{N}\sum_{j=1}^{N}\left\{4\varepsilon_{ij}\left[\left(\frac{\sigma_{ij}}{r_{ij}}\right)^{12} - \left(\frac{\sigma_{ij}}{r_{ij}}\right)^{6}\right] + \frac{q_i q_j}{4\pi\varepsilon_0 r_{ij}}\right\} \tag{38}$$

This potential function contains harmonic terms for bonds and angles, a cosine expansion for torsion angles, and Lennard–Jones and Coulomb interactions for nonbonded interactions. The constants k_i are harmonic force constants, l_i, is the current, $l_{i,0}$ the reference bond length, θ_i the current, $\theta_{i,0}$ the reference angle, V_n, n, γ, and ω describe dihedral angles (rotations around a central bond), ε and σ are Lennard–Jones parameters (a different pair for each possible combination of two different atom types), q_i and q_j are (partial) atomic charges, and r_{ij} is the distance between two atoms. Using this potential function, the forces (the derivative of the potential with respect to position) on all atoms in the system of interest are calculated and used to solve classical equations of motion to generate a trajectory of all atoms in time. An example of a system is shown in Fig. 3: a simulation of a model of the peptide channel alamethicin in a realistic environment consisting of lipids, water, and ions.

The primary result of the simulation is a trajectory of all atoms in time, from which specific details of the system can be analyzed. This is an exciting idea, because atoms can be followed as they move in real time on a timescale of up to ~100 ns, although longer simulations have also been reported. In principle, any properties that depend on coordinates, velocities, or forces can be calculated, given sufficient simulation time. No assumptions are required about the nature of the solvent, there is no need to choose dielectric boundaries because all atoms are explicitly present, and in principle all interactions (water–ions, water–protein, water–lipid, lipid–protein, etc.) are incorporated. This method automatically includes the dynamics of the ion channel protein itself as well as any dynamic effects of the lipids on the ion channel.

Molecular dynamics simulations have been applied by many groups, to a large selection of ion channels as well as to homology models of complex ion channels [14, 85]. Molecular dynamics simulations so far have been useful for a number of problems:

1. Molecular dynamics simulations have shown that the properties of water and ions in narrow channels change significantly compared to bulk. In particular, in many cases

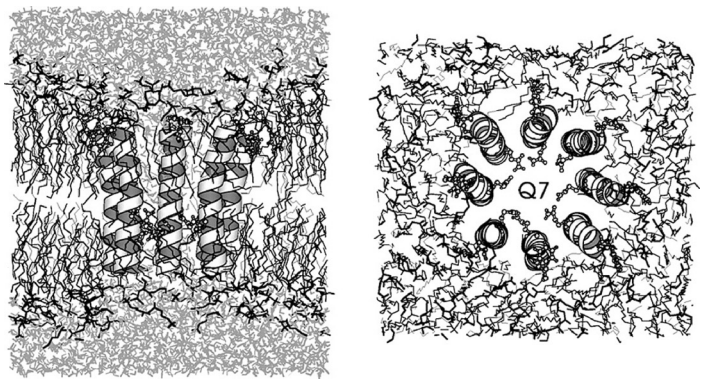

Figure 3. Snapshot of the alamethicin N8 system starting structure after a 25-ps run with position restraints on the peptide. Gln-7 and Phl-20 are drawn as ball and stick, the rest of alamethicin as ribbons, and the phosphatidylcholine headgroup is highlighted in the lipids. Reprinted with permission from [96], D. P. Tieleman et al., *Biophys. J.* 83, 2393 (2002). © 2002, Biophysical Journal.

water molecules are strongly oriented due to local electric fields from the protein. Examples of this may be found in porin [77] and channels formed by parallel helix bundles [14]. In addition, water and ion diffusion coefficients are significantly lower than in bulk, which is relevant for coarse-grained simulations.
2. Molecular dynamics simulations have provided insight into the actual process of ion motion in potassium channels, as well as into local structural changes that may explain the experimentally observed differences between sodium and potassium in the potassium channel or different types of ions in the gramicidin channel (see below).
3. Molecular dynamics simulations have been useful to construct models of channels for which the structure is not known, when such simulations are combined with other modeling techniques and experimental data [86, 87].
4. Molecular dynamics simulations have begun to give detailed insight into the interactions of small molecules and toxins with ion channels [88].
5. Molecular dynamics simulations can be used to make models of states of ion channels that are not present in crystal structures such as the KcsA potassium channel [71, 89].
6. Molecular dynamics simulations give insight into the effect of the environment (lipids) on the channel protein and *vice versa* [90, 91]. This is an important aspect because there are few other techniques available to study this directly.
7. Molecular dynamics simulations can be used to provide parameters and other information for more coarse-grained simulations that can directly be linked to macroscopic properties such as selectivity and current–voltage curves that can experimentally be measured. This is potentially a very powerful use of molecular dynamics simulations that has been applied in a number of cases. Two recent examples can be found in interesting studies of OmpF [92] and the KcsA potassium channel [93].

2.4.2. General Properties of Water, Ions, and Protons in Ion Channels

Water Water properties in narrow spaces differ from bulk water in a number of ways depending on such details as the geometry of the space, polarity, and the local electrostatic potential. Because water motions are fast and fall well within the timescale accessible by molecular dynamics simulations, many researchers have described water properties in a range of channel proteins as well as in simplified models of pores. In particular, the diffusion coefficient of water in narrow pores, its orientation, and its behavior in single-file conditions and in pores lined by hydrophobic residues have received considerable attention.

Diffusion Coefficients In general, inside narrow pores, water diffusion coefficients are found to be lower. The exact degree of reduction depends on the details of the environment, as well as to some extent on the method used to calculate the diffusion coefficient. Diffusion coefficients measured from the mean square displacement show a radius-dependent decrease of up to a factor of 10 compared to bulk, as shown in Fig. 4 [14].

Strictly speaking, these values are not diffusion coefficients because the Einstein relation used to calculate them is only valid in isotropic solutions. Instead, these values contain a significant component due to the local thermodynamic potential, which one can correct for. This becomes particularly important in permeation theories that require both local diffusion coefficients and the potential of mean force [92]. The "true" diffusion coefficients appear typically less reduced compared to bulk than values obtained from the Einstein relation. Single-file diffusion (isotropic in one dimension) follows a different scaling law, in which the mean square displacement is proportional to the square root of time rather than time itself. This can be verified in simulations of nanotubes. The behavior of water transport through carbon nanotubes and model hydrophobic channels has been characterized in great detail [94, 95].

Water Orientation Inside Channels Strong local electric fields are present in many channels. Examples are porin [77], in which the narrowest part of the pore is lined on one side by positively charged residues and on the opposite side by negatively charged residues, and channels formed by parallel alpha-helices such as alamethicin [96], as shown in Fig. 5.

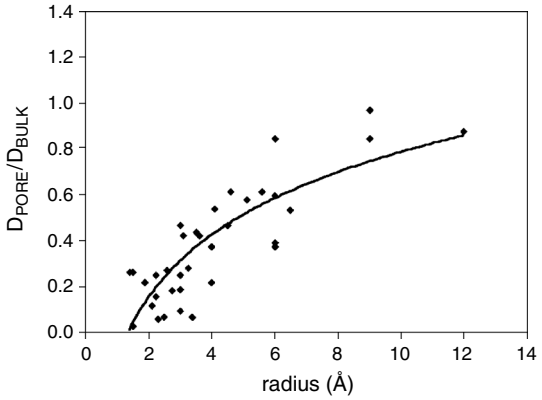

Figure 4. Water diffusion in pores. The ratio of self-diffusion coefficient of water molecules in pores to water in the bulk state (D_{pore}/D_{bulk}) is plotted as a function of pore radius. The data is a compilation summarizing results from simulations of water in smooth cylindrical cavities, simple hydrophilic cylinders, model protein pores, alamethicin channels, models of the nicotinic acetylcholine receptor, and the KcsA potassium channel. The fitted line is simply to guide the eye. Reprinted with permission from [14], D. P. Tieleman et al., *Q. Rev. Biophys.* 34, 473 (2001). © 2001.

These channels show a remarkable degree of water orientation due to interactions with charged residues or the helix dipole moments.

More generally, narrow channels necessarily distort the hydrogen bonding network of bulk water. Perhaps more interestingly, hydrophobic walls or protein walls in general cause a range of new phenomena on a nanoscale that have received considerable attention recently.

Water in Hydrophobic Pores Many biological channels appear to have water-filled pores lined by hydrophobic residues. This has been observed in proteins as varied as rhodopsin, aquaporins, the mechanosensitive channel (known as MscL), and the nicotinic acetylcholine receptor [94]. This seems counterintuitive at first sight, but one possible reason for the presence of these hydrophobic channels is that a hydrophobic pore allows control of gating by reversible filling and emptying. Several simulation papers have studied the behavior of water in such hydrophobic channels in simple model systems. One such system is the carbon nanotube [95]. This tube alternates between completely filled and completely empty, with very rapid filling and emptying.

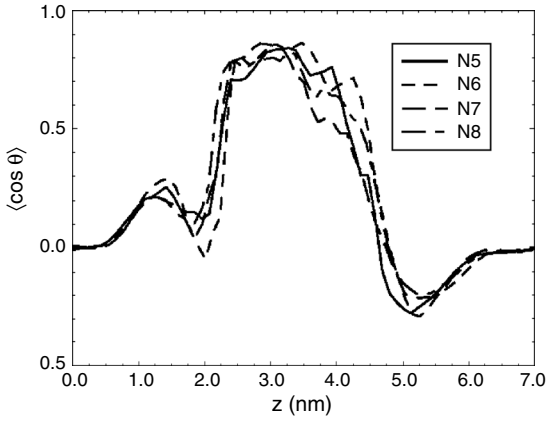

Figure 5. Orientational order of water molecules along the pore axis for N5, N6, N7, and N8 alamethicin model bundles consisting of five to eight helices. The N4 channel does not form a continuous channel, but the orientation of the water molecules is similar. The peaks at 1.5 and 5.5 nm are due to ordering of water molecules against the lipid interface with the hydrogen atoms pointing toward the bilayer center and the oxygen atoms pointing toward the water layer. Note that details of the orientation profile depend on the details of the treatment of electrostatic interactions. Reprinted with permission from [96], D. P. Tieleman et al., *Biophys. J.* 83, 2393 (2002). © 2002, Biophysical Journal.

A second approach uses "methane" spheres to build a channel, in which the polarity of the walls can be tuned by added dipoles. Beckstein et al. [94] performed simulations of an artificial channel in a membrane made of "methane-like" atoms, basically hydrophobic spheres that were harmonically restrained to generate pores of varying lengths and geometry (see Fig. 6). They found that there is a limiting radius of the pore below which water no longer fills the channel. Only a slight increase in the radius will make the channel fill with water. Introducing dipoles in the channel walls to make the pore lining more hydrophilic makes it more favorable for water to fill the pore. Interestingly, the pore seems to fill and empty in rapid bursts [97]. This appears to be due to density fluctuations in the bulk solution [94].

A third recent study considered water dynamics in a narrow, perfectly cylindrical channel in a dielectric slab [98]. This study solved a number of technical problems with combining atomistic detail (water) with continuum electrostatics concepts (low dielectric slab as membrane). It also showed that at a certain (realistic) threshold radius, the channel fills intermittently with water. The probability of this happening increased strongly when an ion was present, which might also be related to gating mechanisms.

Ions Molecular dynamics simulations allow a detailed investigation of ion diffusion coefficients, binding sites in channels, and permeation pathways. Umbrella sampling and free-energy perturbation have been used in several ion channels to calculate potentials of mean force for ion permeation, which give the energetic barriers and wells that determine diffusion through a channel. The KcsA potassium channel and gramicidin A are the most crucial test grounds for such simulations. Several groups have drawn attention to the extreme sensitivity of simulation results on ion–water and ion–protein interaction parameters [14, 85, 99, 100]. The sensitivity arises because the key determinant of ion behavior in narrow channels is the difference in solvation free-energy between the ion in solution and in the protein, a difference between large numbers. When comparing different ions, the relative difference in this quantity becomes important, which is a difficult balance to correctly parameterize.

Despite these difficulties, several groups have reported similar results for the different interactions between sodium and potassium and the selectivity filter of the KcsA potassium channel. There now are several detailed free-energy calculations of sodium and potassium in the selectivity filter of the potassium channel [93, 101, 102]. Berneche and Roux [102] specifically parameterized the interactions of potassium with the carbonyl oxygen in the filter to reproduce interaction energies and distances of small molecule fragments and pointed out several inconsistencies in the interaction parameters between ions and water and ions

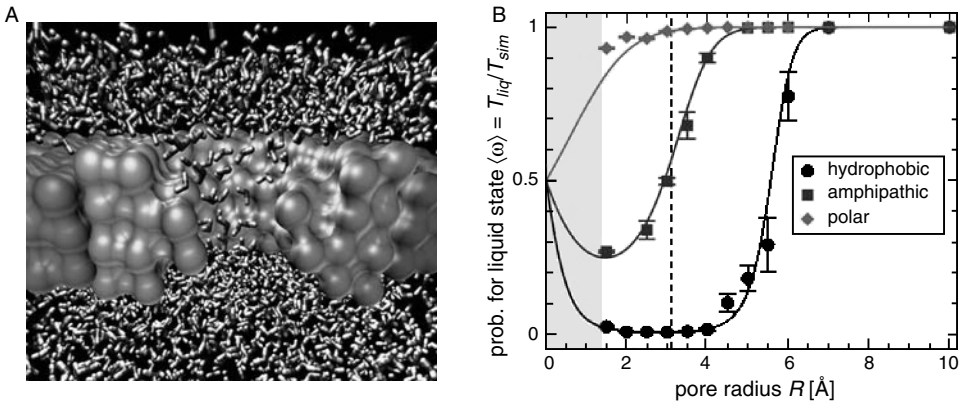

Figure 6. Hydrophobic gating in a model nanopore. (A) A simple model of a nanopore (cyan), embedded in a membrane-mimetic slab (gold), with water molecules (red/white) on either side and within the pore. (B) Pore openness versus radius for a hydrophobic nanopore (black) compared with a nanopore with a polar lining (red). The simulations ranged from 52 to 164 ns in length. The polar lining was formed by two dipoles of magnitude 1.52 Å aligned parallel to the pore lining. The vertical broken line represents the pore radius in the gating region of the (closed) nicotinic acetylcholine receptor. Reprinted with permission from, O. Beckstein et al., *FEBS Lett.* 555, 85 (2003). © 2003, FEBS Letters.

and protein fragments in common force fields. The KcsA potassium channel is of particular interest because the relative occupancy of different monovalent cations in the different sites in the filter is known [103]. In gramicidin A, the interactions are yet again different because the carbonyl dipoles do not point directly at the permeating ions [104]. It is quite challenging (and might not be possible) to develop universal parameters for ions, protein backbone, and water in a classical molecular dynamics context that correctly reproduce all the relevant interactions.

Despite these difficulties, many simulations of gramicidin A have identified the same binding sites, and excellent results have been obtained for finding binding sites for potassium in the KcsA potassium channel [71, 102] and, based on these results, the conductance of the KcsA potassium channel [105]. The bacterial porin OmpF has also been a useful test system for simulations, and details of ion parameters are less likely to be crucial in this large pore in which ions are always solvated by water [92]. Simulations of alamethicin models in different salt concentrations have shown that several ions are nearly permanently present in the channel [106], suggesting ways to engineer channel versions with altered selectivity.

Continuum theories often require diffusion coefficients as input. These can be calculated from molecular dynamics simulations, and similar results are found as for water (see above; the same caveat with regards to the method used to calculate diffusion coefficients applies in this case).

Protons Several smaller channels conduct protons, including gramicidin A, the Influenza A M2 channel, and the engineered LS2 channel. Proton transport presents a special challenge to molecular dynamics simulations because protons move between different water molecules and are not easily treated by a classical potential function. There have been several approaches to extending classical simulations to include protons. The simplest method is to infer the possible behavior of a proton from the behavior of water, which is treated with standard classical potential functions. Although simple, this is not a direct way of studying the behavior of protons.

A next step up in complexity is to use a special water model that can dissociate. Several papers by Pomes and coworkers have investigated proton transport in a number of environments, including gramicidin A, using the PM6 water model [107]. PM6 is a polarizable and dissociable empirical force field consisting of O^{2-} and H^{+} moieties [108]. Voth and coworkers [109, 110] have applied a different method to model proton channels and to models of the Influenza A M2 channel [109, 110]. This model is based on the empirical valence bond (EVB) theory of Warshel [111].

A relatively new method used to simulate proton transport is the QHOP method of Lill and Helms [112], used by de Groot et al. [113] to study proton selectivity in aquaporin 1 (Aqp1), or rather to find an explanation why the water channel aquaporin does not conduct protons. This important problem has recently attracted significant attention, with two other papers presenting similar calculations using different methods, both pointing at electrostatic effects as the reason why protons are not readily transported by aquaporins, although there still are significant differences in interpretation [93, 111, 114].

Finally, one of the most advanced quantum mechanical methods used in channels might be the Car–Parinnello method, a molecular dynamics method that includes part of the system in quantum mechanical detail (using plane wave-based density functional theory, in this case). Dellago et al. [115] have compared the Car–Parinnello molecular dynamics method with the MS-EVB (multi-state empirical valence bond) model in proton transport through carbon nanotubes over short periods of 5–10 ps. Both methods gave comparable results, but the MS-EVB method is much cheaper computationally. No doubt we will see further applications of both these methods to ion channels in the near future.

2.4.3. Limitations of Molecular Dynamics

Despite the power of molecular dynamics due to its ability to provide detailed microscopic dynamics, there are several important caveats and limitations that have to be taken into account. An obvious limitation is the combination of system size and simulation length, which is mainly determined by available computer power and software efficiency. In particular, the

maximum timescale of the order of hundreds of nanoseconds is not enough to determine accurately the average number of ions passing through a channel, except for very wide channels such as porins or simplified geometrical models. This means that by timescale alone, one of our primary objectives, connecting atomic models with current–voltage curves, is still mostly out of reach of molecular dynamics simulations. Obviously, current–voltage curves by direct molecular dynamics simulation would require a number of stimulations at different external voltages.

This in itself is not trivial; certain important aspects of ion channel function are hard to incorporate in molecular dynamics simulations of periodic systems with tens of thousands of atoms. One problem is that incorporating transmembrane potential differences is not straightforward, although a reasonable and promising approximation has been developed [116, 117]. Clearly, this is crucial if we want to calculate current–voltage curves. A second problem is that ionic concentrations are difficult to model, but in many cases essential for the behavior of complex ion-channel proteins. Even uniform low-salt concentrations are not straightforward to represent in a simulation, because it is difficult to sample the motions of the 27 K^+ and 27 Cl^- ions that would make up a 0.15 M KCl solution in a simulation with 10,000 water molecules. Such a simulation would also ignore the effect that the lipids have on the local salt concentration near the bilayer [118], which differs significantly from the bulk concentration. Biologically relevant concentrations of calcium or protons are even more problematic: in a typical simulation system, a physiological calcium concentration in the micromolar range would correspond to much fewer than one ion. Concentration gradients are also not routinely simulated, because the use of periodic boundary conditions typically means there is only a single water phase. Although this is not a fundamental problem, simulations become significantly more complex if two explicit water phases with two different ion concentrations would be incorporated in the model [119].

Modeling the effect of pH has similar problems with concentration and the additional problem that it is hard to model effectively proton transfer between different groups in a classical potential. Usually, pH is incorporated by calculating the pK_a of ionizable residues followed by adjusting the protonation state of ionizable amino acids according to the desired pH, although this is not a trivial calculation [120].

There are also limitations inherent in the specific choice of algorithms used. For example, it is now quite clear that electrostatic interactions must be accurately calculated, but due to their $1/r$ dependence (long-ranged compared to the system size) this entails a certain degree of approximation. Several methods have been proposed [99, 121], the most popular of which currently is Particle Mesh Ewald [122], although this may not be the final answer for membrane systems due to its artificial symmetry.

More fundamentally, the simple potential functions used might not be accurate enough for important details of ion–protein interactions across a range of ions [100]. Although any potential energy function could be used in principle, including much more complex versions than the one given in Eq. (38), parameterizing more complex functions is a daunting task, and there might not be sufficient experimental data to test the parameters. In principle, one could treat the entire system (channel, water, ions, membrane) quantum mechanically, taking the distribution of all electrons in the system into account. This is currently not possible in practice and in general not desirable even if it would be possible, because it seems unlikely electronic detail everywhere in the model is relevant for the process (ion conduction) that we would like to study. Mixed quantum mechanics and molecular mechanics simulations are increasingly used in computational studies of proteins, such as enzymes in which only the active site is treated by quantum mechanics, often by density functional or semiempirical methods [123], or rhodopsin where the chromophore and its direct environment are treated by quantum mechanics [124]. This approach has not been widely applied to ion channels [125] and, indeed, it remains unclear whether this level of detail will prove necessary.

Finally, the starting models used for simulations are rather crucial at the moment. Most simulations of ion channels have been carried out on a handful of high-resolution structures, including gramicidin A [126], OmpF [127], the mechanosensitive channel MscL [128],

and the KcsA potassium channel [129]. From an ion-channel perspective, the KcsA potassium channel is by far the most interesting of these because of its close relationship to physiologically relevant eukaryotic ion channels. The crystal structure initially had a fairly low resolution, which caused some uncertainty in the starting structures for the simulations. More recently simulations based on the 2 Å resolution structure have begun to appear in the literature, permitting a comparison with the 3.2 Å structure [129]. Simulations have also been done on homology models of various channels, in which case it becomes even more important to consider carefully the sensitivity of the results obtained to changes in the model [130].

3. COMPUTATIONAL STUDIES ON ION CHANNELS

Here we highlight some of the computational studies carried out on biological ion channels. We will first discuss in some detail two of the most thoroughly studied ion channels. These are gramicidin A, an antibiotic produced by *Bacillus brevis*, and the KcsA potassium channel, whose x-ray structure has been unveiled recently. In the absence of structural information for biological ion channels, gramicidin A has been the main focus of theoretical investigations for a long time. The recent determination of the crystal structure of the KcsA potassium channel [3] has now shifted the attention to biological ion channels, including potassium channels, the ClC Cl^- channels and the mechanosensitive channels. Because there are only a few computational studies on these channels reported in the literature, they are only mentioned briefly in this chapter.

3.1. The Gramicidin Channel

The gramicidin A pore is formed by a linear polypeptide consisting of 15 hydrophobic amino acids in an alternating L–D sequence. It was one of the first antibiotics to be discovered by Hotchkiss and Dubos [131]. The peptide in submicromolar concentrations increases the conductance of lipid bilayers by more than seven orders of magnitude. This enormous increase in conductance owes to the fact that, in membranes, the dimer of the antibiotic peptide gramicidin A forms a cation-selective pore. To form a pore, two gramicidin peptides link briefly head-to-head by hydrogen bonds between their formyl end groups [132], creating a cylindrical passage across the membrane with length 25 Å and radius 2 Å. This narrow lumen size mandates that solutes even as small as urea are not allowed to move across the pore. When an ionic passage across the membrane is formed, stepwise conductance increases in lipid bilayers can be recorded, each channel-opening event lasting between 30 ms and 60 s [133–136]. Gramicidin A has long served as a model for theoretical work on ion channels, partly because of its simple structure and partly because it was the only high-resolution structure known. There is a vast literature on theoretical studies of gramicidin A, and we only present a few papers that illustrate important points learned from gramicidin A.

Its physiological properties are characterized by linear current–voltage curves and relatively large half-saturation concentrations. These observations point to a lack of substantial barriers within the channel. In addition, NMR studies indicate well-defined binding sites near the pore entrances. This wealth of functional data has been matched with an atomic resolution structure since 1971 [132]. For these reasons, the gramicidin channel has played a prominent role in development of permeation models in ion channels. There is extensive literature on modeling of the gramicidin channel, which can be traced from several review articles [10, 11, 126, 137–142].

3.1.1. Semimicroscopic Studies

Modeling of the gramicidin channel evolved from simple electrostatic calculations with rigid dielectric boundaries [143–145] to complicated all-atom molecular dynamics simulations with the channel imbedded in a lipid bilayer and solvated with water [146–148]. Some of the outstanding issues in the gramicidin channel that have been investigated using various theories will briefly be addressed in this chapter.

It is not entirely clear if the lower resolution permeation theories such as the Poisson–Nernst–Planck equations [12, 13] and Brownian dynamics simulations [9, 68, 69], in which the forces are calculated from Poisson's equation, can reliably be applied in modeling the gramicidin channel [10, 11, 35]. First, inferences made from macroscopic electrostatics are valid only in the regions that are large compared to the diameters of water and ion molecules. In the gramicidin channel, whose radius is only 2 Å, the representation of the dielectric as a continuous medium is a poor approximation. Moreover, the water molecules form a linear chain in the pore. Second, these theories assume that the structure of the channel remains rigid, not influenced by the presence of a permeating ion, although the recent nuclear magnetic resonance experiments appear to justify this assumption [149, 150]. Despite these reservations about the applicability of the continuum theories to this channel, the Poisson–Nernst–Planck theory has recently been applied to it, giving an apparently successful description of the current–voltage relations [44–46].

Using Brownian dynamics simulations, Edwards et al. [151] deduced the potential energy profile encountered by permeating ions that correctly reproduces the experimental observations. An example of a potential profile for a K^+ ion constructed from this inverse method is given in Fig. 7A. The profile they derived has two energy wells with the depth U_w, separated by a central barrier with the height U_b. These are two parameters that needed to be determined from the Brownian dynamics simulations by fitting the calculated conductance under

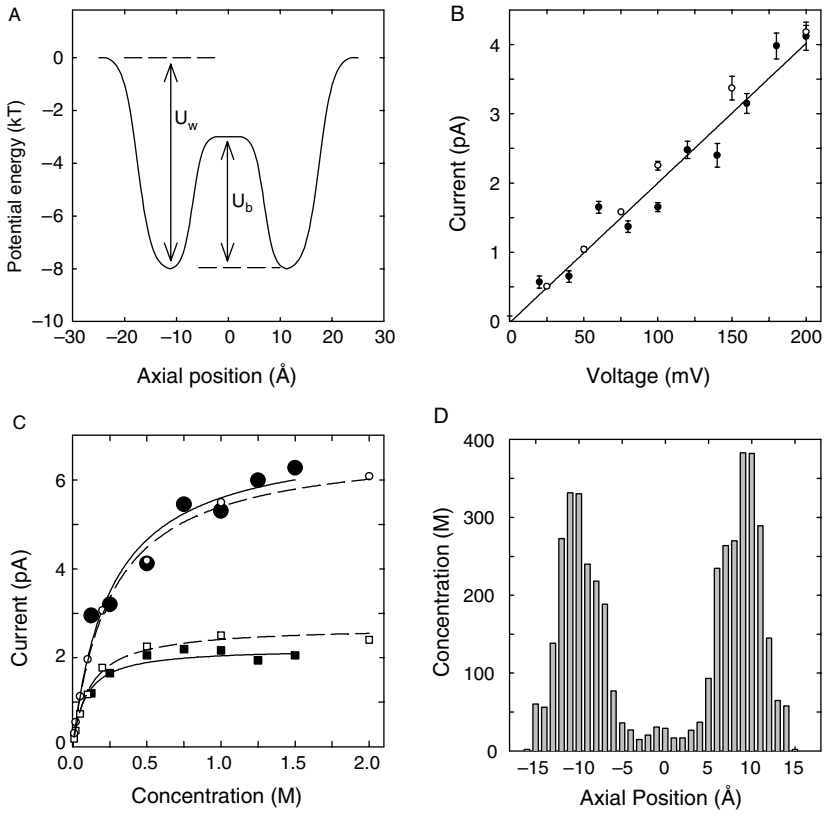

Figure 7. Properties of the gramicidin channel deduced from Brownian dynamics simulations. (A) When the shape of the potential profile experienced by a K^+ ion moving across the pore shown in the figure is incorporated into Brownian dynamics, the simulated results closely match the experimental observations. (B) The current–voltage relationship obtained with Brownian dynamics simulations by using 500 mM KCL (filled circles and solid line) is compared with the experimental data of Andersen (open circles). (C) The current–concentration curves are obtained with two different applied potentials, 100 mV (bottom curve) and 200 mV (top curve). The experimental data of Andersen are superimposed on the figure (open circles). Both simulated and experimental data are fitted with a Michaelis–Menten curve. (D) The dwell histogram for K^+ ions in the pore is obtained with no applied potential. Reprinted with permission from [151], S. Edwards et al., *Biophys. J.* 83, 1348 (2002). © 2002, Biophysical Journal.

different applied potentials and concentrations to the available physiological data. In the profile illustrated in Fig. 7A, these two parameters, U_w and U_b, are 8 kT and 5 kT, respectively. The current–voltage–concentration profiles obtained with Brownian dynamics simulations using the profile illustrated in Fig. 7A are shown in (B) and (C). A current–voltage curve obtained from simulation of a symmetrical 500 mM KCl solution (filled circles) is compared with the experimental measurements (open circles) in Fig. 7C. The current saturates at two applied potentials: 100 mV (bottom curve of C) and 200 mV (top curve of C). The experimental data of Andersen are superimposed on the figures (open circles). The calculated curves, fitted with Michaelis–Menten curves, follow the experimental results closely at both driving potentials. The calculated half-saturation value of 250 mM is in good agreement with the experimental value of 230 mM at 200 mV. The corresponding values at 100 mV are 90 mM (simulated) and 105 mM (experimental). Figure 7D shows the concentration profiles of K^+ ions in the gramicidin channel obtained from a symmetric 500 mM KCl solution. The ion concentration is very large at the binding sites and depressed in the middle. There are on average 0.75 ions at each site, indicating that the channel is often multiply occupied. Thus, a satisfactory description of the data can be obtained from the energy profile illustrated in (A).

3.1.2. Molecular Dynamics Studies

In a pioneering study, Åqvist and Warshel [152] calculated a free-energy profile for sodium in the gramicidin channel based on the electrostatic protein-dipoles-Langevin-dipoles (PDLD) model, a semimicroscopic model midway between an all-atom representation and a continuum model, and found reasonable well depths and barriers. They compared the results from this model with free-energy perturbation calculations of the solvation of Na^+ in bulk water and inside the channel, yielding similar results when the induced dipoles due to the low dielectric membrane environment were taken into account. An important aspect of this work is that the low dielectric environment from the membrane was taken into account explicitly. This allows an estimate of the significant effect of this term (about 10 kcal/mol), which has not always been included in later simulations.

Several molecular dynamics simulations have suggested that ion permeation is coupled to motions of the channel. The backbone of the gramicidin peptide exhibits some flexibility with the carbonyl oxygens swinging up to 10–20° [147, 153] to provide adequate solvation for a nearby ion. Roux and Karplus [11] found that there is a "peristaltic" change in conformation as a cation passes along the channel, displacing the carbonyl oxygens of the peptide backbone toward the channel axis. Deformability of the channel seems to play an important role in the dynamics and energetics of permeation of the channel by water and by ions. However, recent high-resolution nuclear magnetic resonance studies of cation transport in the gramicidin channel [149, 150] find that the gramicidin peptide remains rather rigid upon cation binding, and the ion is solvated by just two carbonyl oxygens and two water molecules. A reaction path simulation by Elber et al. [154] also showed that the motion of a permeating sodium ion is coupled to motions of water and the channel. Their calculations suggest that Na^+ does not take a straight path through the channel and questions the validity of a potential of mean force calculation for a single ion at different locations in the channel.

De Groot et al. [155] used molecular dynamics simulations to explain why a particular form of gramicidin makes an excellent water channel. Gramicidin A is found in at least two different forms, and there has been some controversy regarding which form is the main ion channel form, although the so-called head-to-head dimer is now almost universally thought to be the ion channel form [156]. The simulations of de Groot et al. [155] suggest that by removing a formyl group from the N-terminus, the double helix form rather than the head-to-head dimer becomes dominant and is a better channel for water transport.

The gramicidin channel was used to test the effect of the anesthetic halothane on its structure and dynamics [157]. Interactions of membrane-soluble anesthetics with ion channels could be a general mechanism for certain forms of anesthesia. They found some changes in the dynamics of the channel in the close presence of halothane, which might be a mechanism for general anesthetics that could modulate ion channels in neuronal membranes in a similar fashion.

The ability to obtain accurate potentials of mean force for ion permeation is crucial to link atomistic simulations to macroscopic observables like current–voltage curves. To date, all such molecular dynamics calculations have lead to central energy barriers that are too high to allow ion permeation through the gramicidin channel at the observed rates. To give an example, the lowest translocation barrier calculated for Na^+ ions is about 20 kT [158, 159], which would completely suppress flow of ions. The height of this central barrier is reduced somewhat when several corrections are made to take into account the finite size of the simulation box and the underestimated dielectric constant of the lipid interior [160]. However, a reduction in the height of the central barrier is not sufficient large to replicate accurately the experimental data.

Molecular dynamics simulations deduce the locations of the binding sites in the gramicidin channel consistent with the experiments. The selectivity sequences among monovalent cations, calculated from the free-energy differences, are in agreement with the experimental sequence $Cs^+ > K^+ > Na^+ > Li^+$ [161, 162]. Through the gramacidin channel, the larger ions with smaller hydration energies conduct better, just as in bulk electrolytes.

There are now several high-resolution structures of gramicidin A, solved under different experimental conditions by different methods, that differ in some structural details. Allen et al. [104] simulated two recent structures, one from solid-state nuclear magnetic resonance [163] and the other from solution nuclear magnetic resonance in micelles [164]. These structures differ in side-chain rotamers as well as in backbone structure. Extensive molecular dynamics simulations (100 ns) have shown that both these structures are relevant, but exist in a dynamic equilibrium. They were able to calculate the relative population of the two states and also showed that relaxation of the structure has a significant effect on the size of the barrier for ion permeation. A "relaxed" structure from molecular dynamics simulations has a lower barrier for cation permeation and gives better agreement with the experimental conductance rates than calculations based on the high-resolution structure directly [104]. This somewhat alters the results of Allen et al. [104] who compared the potential of mean force for cation permeation based on simulations of gramicidin A with different force fields. These simulations gave too high a barrier, which might therefore be related to properties of the structure used for these simulations [104].

With the appearance of the crystal structure of the KcsA potassium channel, the theoretical interests in the gramicidin channel have appreciably diminished. Nevertheless, because the gramicidin channel has such a simple structure and is so rich in physiological data, it can still play an important role in the development of permeation models. After all, if a model works in the more complicated case of KcsA but fails in the case of gramicidin A, it would lose much credibility.

3.2. The KcsA Potassium Channel

The unraveling of the crystal structure of the KcsA potassium channel by Doyle et al. [3] at 3.2 Å resolution was a landmark event that will have a lasting impact on ion channel studies. As the KcsA potassium channel is the first biological ion channel whose tertiary structure has been elucidated, it has been a prime target for simulation and modeling studies. These include the mechanisms underlying the permeation of ions across the channel, the basis of ion selectivity, and the conformational changes that occur in the KcsA protein when the channel opens. The KcsA potassium channel and other bacterial channels share their main features with eukaryotic potassium channels, based on evidence from toxin binding studies [165], conductance measurements [166], and from direct substitution of the KcsA filter in Shaker and inward rectifier potassium channels [167]. This last experiment is especially impressive: replacing the entire pore section of the voltage-gated Shaker channel by the pH-gated KcsA results in a voltage-gated hybrid channel. Very recently, Morais-Cabal et al. [168] succeeded in refining the crystal structure of KcsA to 2.0 Å, which allowed direct observation of the binding sites of K^+ ions in and near the selectivity filter, as well as the water molecules that are coordinated with these K^+ ions [169]. These latest results could have ramifications in much wider fields as they turned the KcsA channel into a microscopic laboratory for studying the ion–water–protein interactions.

Additional potassium channel structures have confirmed that the central pore region is quite conserved structurally. MthK is a calcium-gated potassium channel that was trapped in the open state by the presence of calcium [170]. KirBAC is an inward rectifying channel that was crystallized in a closed state [171], and KvAP is the first voltage-gated channel to have its high-resolution structure solved [172, 173]. This structure has led to very interesting controversies because of the unexpected orientation of the S1–S4 domain, which contains the voltage sensor [174].

3.2.1. The Structure of the Potassium Channel

The structure of the KcsA potassium channel determined from x-ray diffraction consists of 396 amino acid residues, or 3504 atoms excluding polar hydrogens. The overall shape of the channel resembles a truncated cone with a central pore running down the center, as shown in Fig. 8. The wider end of the cone corresponds to the extracellular mouth of the channel. The transbilayer pore is formed by a bundle of eight transmembrane helices, four M1 and four M2 helices. The selectivity filter with the potassium channel signature motif TVGYG (threonine-valine-glycine-tyrosine-glycine) is located near the extracellular mouth of the channel. This filter contains distinct ion binding sites that are well resolved in the crystal structures. Below the selectivity filter is a central water-filled cavity, which also shows a well-resolved ion-binding site in the high-resolution structure. The pore-lining M2 helices constrict the intracellular mouth to form a gate region. In this region, the pore radius falls to about 1.1 Å, that is less than the Pauling radius of a K^+ ion, 1.3 Å.

The KcsA potassium channel is known to be activated at low intracellular pH [175, 176]. Paramagnetic spin resonance studies [177, 178] have indicated that the crystal structure of the KcsA potassium channel corresponds to a closed conduction state, and the transmembrane helices forming the intracellular pore move away from the channel axis during gating. Also, in the crystal structure, the radius of the narrowest section of the pore on the intracellular side is 1.2 Å, smaller than the radius of the potassium ion (1.33 Å). To study the conductance properties of the channel, therefore, one needs to construct an open-state model by increasing the intrapore radius of the structure.

In the crystal structure, K^+ ions are observed to occupy four sites in the filter region with approximately equal probabilities [168]. These sites are in between the planes defined by the carbonyl and hydroxyl oxygens of the Y_{78}, G_{77}, V_{76}, and T_{75} residues. Thus, a K^+ ion in one

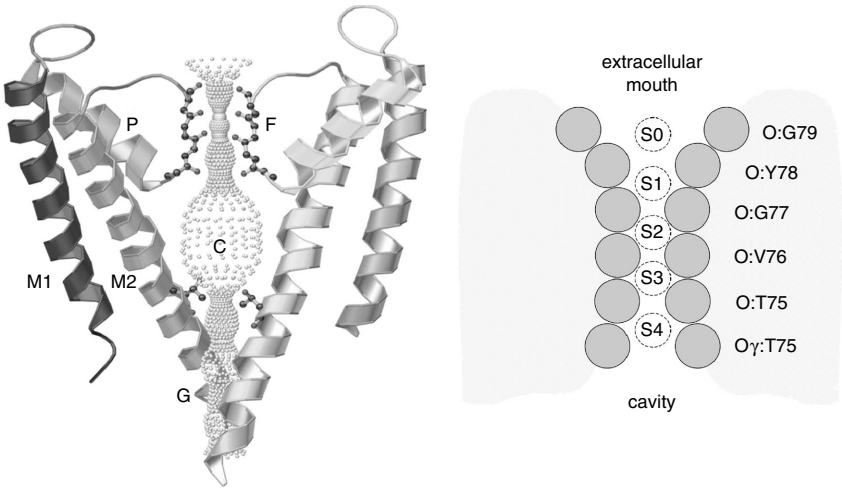

Figure 8. The bacterial (KcsA) potassium channel. (A) Two of the four subunits are shown, viewed perpendicular to the pore axis, with the selectivity filter at the top of the diagram and the intracellular gate region at the bottom. The lining of the channel is shown as a dotted surface. The M1, M2, and P helices are labeled, along with the selectivity filter (F), the central cavity (C), and the intracellular gate (G). (B) The ion binding sites (dotted circle) in the selectivity filter, together with the carbonyl oxygens (gray balls) of the residues lining the pore are indicated. Modified with permission from [14], D. P. Tieleman et al., *Q. Rev. Biophys.* 34, 473 (2001). © 2001, Biophysical Journal.

of these sites is solvated by eight oxygens from the neighboring residues. A similar eightfold coordination of ions with water molecules is observed in the cavity and at the extracellular mouth of the channel [169]. These results are interpreted as two K^+ ions, with a water molecule between them, permanently occupying either the sites 1–3 or 2–4, and oscillating between these two configurations without any significant free energy barriers. Appearance of a third K^+ ion in the filter disrupts this equilibrium, starting a conduction event. The fact that K^+ ions are eightfold coordinated with oxygen atoms at all sites from entry to exit makes the permeation process through the filter energetically very smooth, especially during the critical dehydration and rehydration steps.

3.2.2. Brownian Dynamics Studies of Ion Permeation

To determine currents flowing across the channel, several groups [69, 71, 72, 99, 105, 179] have carried out Brownian dynamics simulations on the KcsA channel using the experimentally determined channel structure. A qualitative picture of the permeation dynamics can be gleaned from the energy landscape encountered by an ion moving across the channel. Figure 9A illustrates the potential energy of a potassium ion brought into the channel from the intracellular reservoir in the absence of other ions [71]. The energy well experienced by a single ion is deep, reaching 67 kT within the selectivity filter with respect to the intracellular reservoir. The well is deep enough to accommodate two ions. Figure 9B shows the energy profile experienced by a third ion entering the channel already housing two ions. The position of the resident ions when the test ion reaches the center of the channel ($z = 0$ Å) is indicated as upward arrows. In constructing this profile, the resident ions in the channel are allowed to adjust their positions so that both axial and radial components of the force

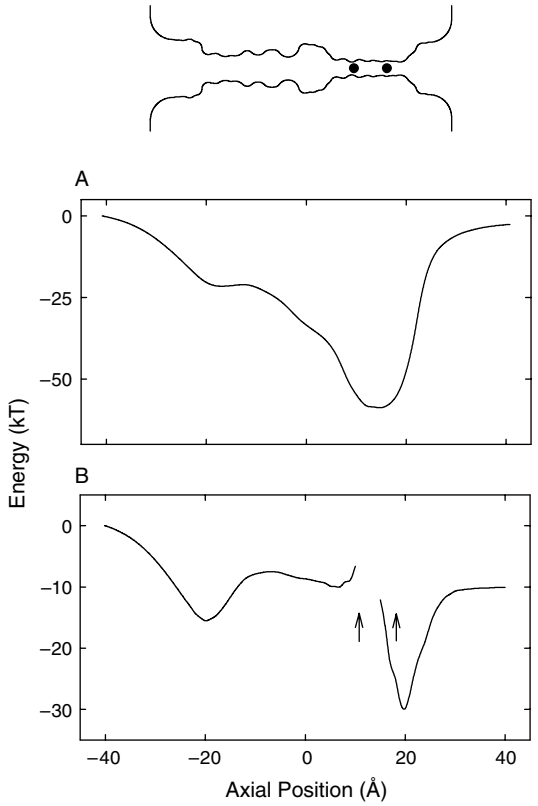

Figure 9. Electrostatic energy profile of an ion traversing the potassium channel. (A) The profile reveals potential energy encountered by a single K^+ ion as it moves across the pore. (B) The potential energy profile is constructed for a third K^+ moving from the intracellular end of the selectivity filter to the extracellular space, given that the filter is already occupied by two resident ions. The locations of the resident ions are shown as filled circles in the inset. Reprinted with permission from [71], S. H. Chung et al., *Biophys. J.* 82, 628 (2002). © 2002, Biophysical Journal.

on them are minimized. Thus, the potential profile for multiple ion systems corresponds to the total electrostatic energy required to bring in the charge on the test ion from an infinite distance in infinitesimal amounts. With two ions in the selectivity filter, a third ion entering the channel sees an energy well, created by the mouth dipoles near the intracellular entrance. The ion needs to overcome a central barrier of 7–8 kT to move toward the wide cavity region. This is expected to be the rate-limiting step for conduction. Once in the cavity, the stable equilibrium established by the resident ion is disrupted, and the outermost ion is expelled from the channel. The electrostatic profiles illustrated in Fig. 9 ignore the influence of ionic atmosphere and other dynamic effects such as entropy. Because anions do not enter the channel, neglect of the counter ions is justified. From the profile illustrated in the figure, it is clear that conduction will not take place unless there are two or three resident ions in the channel. For a single ion to traverse the selectivity filter, it has to gain an energy of nearly 70 kT to exit the energy well shown in Fig. 9A.

Brownian dynamics simulations carried out by Chung et al. [71] show that there are three regions in the selectivity filter and cavity where K^+ ions dwell preferentially, as illustrated in the histogram in Fig. 10. To construct the histogram, the channel is divided into 100 thin sections, and the average number of ions over a simulation period of 0.1 μs is plotted. The locations of their maxima are indicated schematically in the inset. The location of their maxima are $z = 4.5$ Å (inside the cavity), 12.3 Å (near the T_{75} carbonyl oxygen), and 19.2 Å (near the Y_{78} carbonyl oxygen). Also, there is another prominent peak in the histogram, centered at -21 Å. Here, guarding the intracellular gate are four negatively charged amino acid residues (E_{118}). The average number of ions is 2.9 in the selectivity filter and the cavity and 0.9 near the intercellular entrance. The ion in the cavity region tends to reside mostly off-axis, as a result of the strong interaction with the oxygen atoms of the T_{74} residue at the base of the pore helix. The positions where ions dwell preferentially are in close agreement with the positions observed in Rb^+ x-ray diffraction maps [3].

There is now a general consensus on the process by which a conduction event across the potassium takes place. The most common situation in the conducting state of the channel has one ion in the left (intracellular) half and two ions in the right (extracellular) half. The ion waiting near the intracellular mouth overcomes a small energy barrier in the intracellular pore to enter the chamber region. Because this system is unstable in the presence of an applied potential, the rightmost ion is ejected from the channel. Another ion enters the intracellular mouth, leaving the system in its original configuration. Naturally, conduction

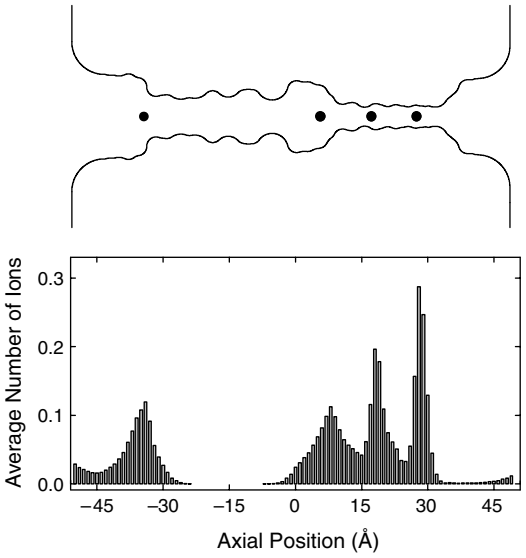

Figure 10. Average number of ions in the potassium channel. The channel is divided into 100 sections, and the average number of ions in each section is calculated over a simulation period of 1 μs. The inset shows the locations of the binding sites (filled circles) in the channel. Reprinted with permission from [71], S. H. Chung et al., *Biophys. J.* 82, 628 (2002). © 2002, Biophysical Journal.

of ions depends on their concentration, applied potential, and the ionization state of the charged residues at the channel entry, and many other states can be involved in the conduction process depending on the values of these variables. For example, at high concentrations and potentials, before the outermost of the three ions on the right side of the channel is ejected from the channel, a fourth ion may enter the left side of the channel. A common feature of all these conduction events is that the presence of 3 K^+ ions on the right side of the channel triggers a conduction event. This prediction of the Brownian dynamics simulations on the mechanism of ion permeation across the filter region has been confirmed by the latest experiments on the KcsA channel [168].

In Fig. 11, the current–voltage and current–concentration curves obtained from Brownian dynamics simulations are shown [71]. The radius of the intracellular gate is fixed at 4 Å. The outward conductance at 150 mV is 147 $\pm$ 7 pS. The relationship is linear when the applied potential is in the physiological range ($V < 150$ mV) but deviates from Ohm's law at a higher applied potential (Fig. 11A). In broad agreement with those determined experimentally [166, 175, 180–182], the current saturates with an increasing ionic concentration (Fig. 11B). This arises because the average time τ it takes for an ion to transit the channel has two components: the time needed for an ion to access the channel (τ_1), and the time it takes an ion to traverse the channel (τ_2). The first process, τ_1, is dependent both on the electric field E across the channel and the ionic concentration $[c]$ in the reservoir, whereas the second process, τ_2, depends solely on the electric field. Thus,

$$\tau_1 = \frac{k_1}{[c]E}, \qquad \tau_2 = \frac{k_2}{E} \tag{39}$$

where k_1 and k_2 are constants. The current carried by K^+ ions across the channel is

$$I = \frac{e}{(\tau_1 + \tau_2)} = \frac{eE}{k_1/[c] + k_2} \tag{40}$$

For large concentrations, Eq. (40) approaches a maximum value that we denote by $I_{\max} = eE/k_2$. Factoring out k_2 and letting $K_s = k_1/k_2$, Eq. (40) can be written in the form

$$I = \frac{I_{\max}}{1 + K_s/[c]} \tag{41}$$

This is the Michaelis–Menten equation, which adequately describes the current–concentration curves obtained from ionic channels. As an example, we give the average times it takes for an ion to move through the various sections of the channel with an applied potential of 250 mV and concentration of 300 mM: the time it takes for an ion to enter the channel from the intracellular side is about 5 ns, the time for this ion to transit across

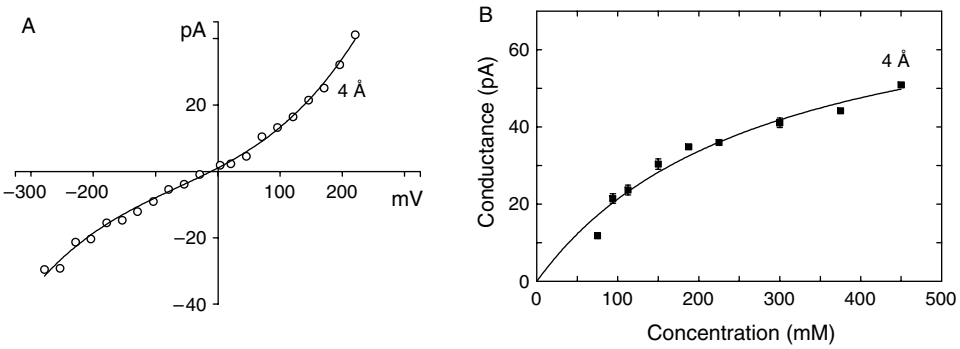

Figure 11. The current–voltage–concentration profile of the potassium channel with the intrapore radius of 4 Å. (A) The magnitude of current passing through the channel with symmetrical solution of 300 mM KCL in both reservoirs is plotted against the applied potential. (B) The outward current are obtained with symmetrical solutions of varying concentrations of KCl in the reservoirs. Reprinted with permission from [71], S. H. Chung et al., *Biophys. J.* 82, 628 (2002). © 2002, Biophysical Journal.

the channel to reach the cavity is 6 ns, and finally, the time for the right-most ion to exit the filter is less than 1 ns. The last two processes, being independent of concentration, are the rate-limiting steps in conduction at high concentrations. It is worth emphasizing that permeation across the filter is much faster than in other parts of the channel. Thus, although the filter plays a crucial role in selecting the K^+ ions, its role in influencing their conductance properties is minimal.

There are many different types of potassium channels, which differ widely in their conductances and gating characteristics [8]. Conductance levels of various types of potassium channels range from 4 to 270 pS. Despite this diversity, they all share the common feature of being highly selective to potassium ions. The amino acid sequence of the peptide chains lining the selectivity filter of all potassium channels is known to be highly conserved [3, 165, 167, 182, 183]. This has important ramifications for modeling of other potassium channels because one can start from the KcsA structure as a template. An example of this approach is the work of Chung et al. [72]. A simplified model of the KcsA channel was developed that reproduced the calculated properties of the atomic-detail model. Then, using such simplified models, they studied how changes from this structure influences its permeation properties. A model channel is generated by rotating the solid curve shown in Fig. 12A around the symmetry axis by 180°. The shape of the channel corresponds approximately to that of the open-state KcsA channel with the full atomic details (see Inset of Fig. 12). Sets of dipoles of various strengths with fourfold symmetry, shown as filled circles and diamonds in Fig. 12A, are placed on the simplified channel model such that their net effect on an ion traversing

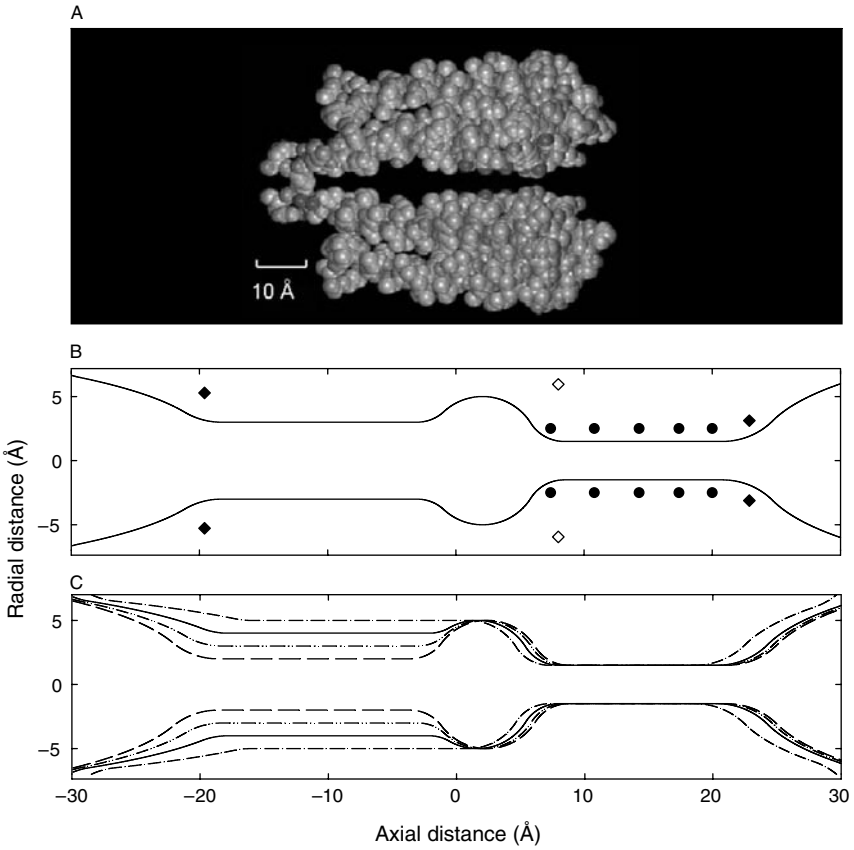

Figure 12. Models of potassium channels. (A) Two of the four subunits of the KcsA potassium channel are shown. (B) The shape of the channel is modified such that the minimal radius of the pore is 3 Å. Solid line shows the outline of a simplified model channel. The positions of dipoles on the channel wall are indicated. Filled circles are 10 of the 20 carboynl and hydroxyl oxygen atoms, open diamonds are N termini of the helix dipole, and filled diamonds are mouth dipoles. (C) Outlines of a set of model channels are superimposed. The radius of the channel facing the intracellular space (left side) is systematically changed from 1.5 to 5.0 Å. Reprinted with permission from [72], S. H. Chung et al., *Biophys. J.* 83, 263 (2002). © 2002, Biophysical Journal.

the pore will be approximately the same as that of an ion traversing the atomic-detail model. Starting from the prototype channel, the aperture of the intracellular pore entrance is expanded from 1.5 to 5.0 Å in steps of 0.5 Å, as shown in Fig. 12B.

The potential energy profiles, obtained in the presence of two resident ions in the selectivity filter, are illustrated in Fig. 13A for three channels with radii 2, 3, and 4 Å. Two prominent features of these profiles are the energy barrier centered at $z = -10$ Å and the accompanying well at $z = -20$ Å. The height of the energy barrier ΔU an ion needs to traverse the channel from left to right decreases progressively from 7.7 to 0.8 kT as the radius

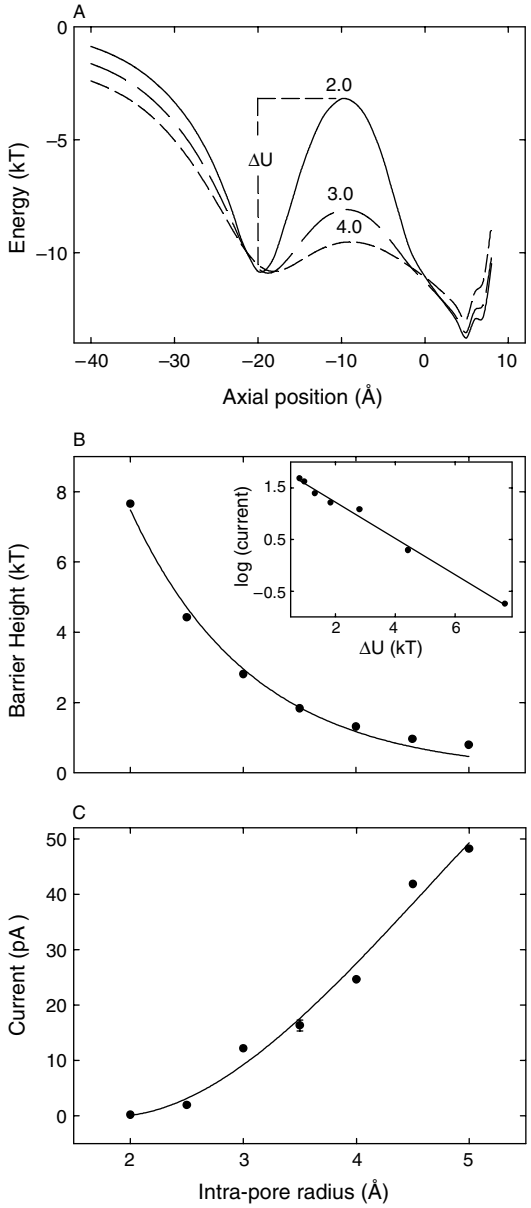

Figure 13. Rate-limiting factors in outward currents across potassium channels. (A) Potential energy profiles encountered by an ion traversing along the central axis of the channel when there are two other ions in or near the selectivity filter are shown for the channels with radii 2 Å (solid line), 3 Å (long-dashed line), and 4 Å (dashed line). Ions need to climb over the energy barrier, whose height is denoted as ΔU, to move across the channel. (B) The barrier height ΔU is plotted against the intrapore radius. In the inset, the outward current in the logarithmic scale is plotted against ΔU. (C) The dependence of outward channel currents on the intrapore radius of the channel is illustrated. The applied field to obtain the current is 2×10^7 V/m. Reprinted with permission from [72], S. H. Chung et al., *Biophys. J.* 83, 263 (2002). © 2002, Biophysical Journal.

of the intrapore gate is widened from 2 to 5 Å (Fig. 13B). For an outward conduction to take place, an ion sitting in the energy well needs to climb out of the barrier and proceed toward the central cavity. Thus, the enhancement in the barrier height is expected to make an ion's transit from the inner well to the cavity harder, thus retarding the conduction rate. In the inset, the log of the current across the channel is plotted against ΔU, which clearly shows the exponential decrease in conductance with the increasing barrier height. As illustrated in Fig. 13C, the current under the influence of an applied electric field of 2×10^7 V/m (about 200 mV) increases steeply with increasing intrapore radius of the channel. The outward current increases from 0.18 to 48 pA as the radius increases from 2 to 5 Å. With an applied field of 10^7 V/m, the outward and inward currents with the 5 Å channel are 21 pA (187 pS) and 33 pA (210 pS), respectively. Thus, changing the radius of the intrapore region from 2 to 5 Å increases the channel conductance by nearly two orders of magnitude, sufficient to explain the range observed in nature. This gives hope that individual potassium channels can be modeled using Brownian dynamics by taking into account available structural and physiological data.

3.2.3. Molecular Dynamics Studies of Ion Permeation

There are now numerous molecular dynamics simulations based on the initial structure reported by Doyle et al. [3], with varying degrees of approximation of the protein and its environment [85, 129, 184]. A simplified model of the KcsA potassium channel with an atomistic filter and the remainder of the protein treated as a hydrophobic continuum was used by Allen et al. [185]. The whole protein, with restraints on parts of the protein to compensate for the missing membrane environment, with water molecules within the pore at either mouth, has been simulated in a number of studies [186]. At the next step up in complexity, the unrestrained protein has been simulated embedded in a bilayer-mimetic environment made up of a "slab" of octane molecules [187] or of "hydrocarbon-like atoms" [101]. Finally, several studies have used a more realistic representation of the environment of the KcsA potassium channel, including a fully solvated phospholipid bilayer [102, 188, 189], and other more recent studies include one using the high-resolution 2 Å structure [129]. Below we summarize some of the results obtained.

3.2.4. Remodeling the Channel Structure

Potassium channels, as well as many other ligand-gated or voltage-gated channels, are controlled by sensitive mechanisms that regulate opening, closing, and in many cases numerous intermediate states. As noted in the previous section, the structure of the KcsA potassium channel [3] is in a closed conformation, so that a natural question is to ask what the open state might look like. Several simulation and modeling papers have tried to address this by various nonequilibrium mechanisms. Biggin and Sansom [190] placed a spherical virtual "balloon" near the intracellular half of the channel that only interacted with the channel, not with water or lipids. By slowly "inflating" this balloon, the channel helices are forced apart, opening the channel, as shown in Fig. 14. Similar methods in creating open-state structures of the potassium channel based on displacing the helices at their narrowest point were used by others [71, 99, 179]. Experimental support for conformational changes came from electron spin resonance measurements on the KcsA potassium channel [177] and from accessibility studies on a voltage-gated potassium channel that show which part of the pore lining helices is accessible from the intracellular side in the open state [191]. An elegant study of the classical phenomenon of N-type inactivation in a voltage-gated potassium channel also suggests the intracellular side of the channel must be able to open quite substantially compared to the KcsA potassium channel [192]. This was confirmed by the crystal structure of MthK, a calcium-gated channel that was crystalized in the presence of calcium, in an open structure [193]. The conformational changes compared to the closed structures of KirBAC and KcsA are quite substantial. Although they are larger than most predictions by simulation, several of the simulated/modeled structures are quite reasonable.

The KvAP channel, another type of the potassium channel, is an interesting case. Voltage gated potassium channels open and close under the influence of the transmembrane

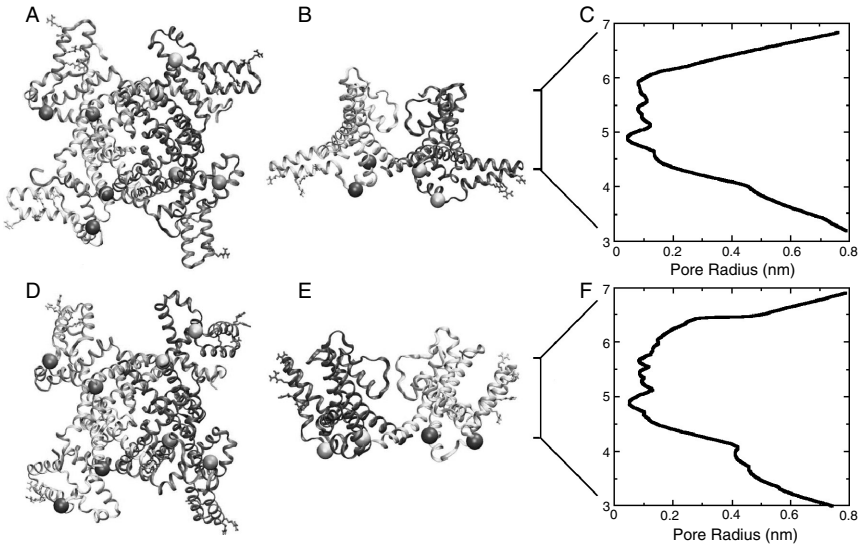

Figure 14. Structures before (A to C) and after (D to F) pulling the tip of the paddle to the extracellular side of the protein. Views are shown from the cytoplasmic side (A and D) and from the plane of the membrane (B and E). Large spheres indicate the positions of the C-alpha carbon of residues S132 and K147 located near the ends of S4 and S5, respectively. As the paddle is pulled up, the S4–S5 linker moves in a clockwise direction (as viewed from the cytosol, A and D), and S132 moves from being below K147 to almost parallel (as viewed from the plane of the membrane, B and E). Curves illustrated in (C) and (F) show the radius of the central portion of the channel. Reprinted with permission from [194], L. Monticelli et al., *FEBS Lett.* 564, 325 (2004). © 2004, FEBS Letters.

potential. They consist of six transmembrane helices, two of which are homologous to other channels whose structures have been solved. It is also known that S4 carries the "voltage sensor," highly conserved arginines that are crucial for voltage-dependence of voltage-gated potassium channels. The recent crystal structures of this channel and its isolated voltage-sensing "paddle" (composed of segments S1 to S4) challenged existing models of voltage gating, but also raised a number of questions about the structure of the physiologically relevant state.

Monticelli et al. [194] investigated a possible gating mechanism based on the crystal structures in a 10-ns steered molecular dynamics simulation of KvAP in a membrane-mimetic octane layer. In this simulation, the structure of the full KvAP protein was modified by restraining the S2–S4 domain to the conformation of the isolated high-resolution paddle structure. After an initial relaxation, the paddle tips are pulled through the membrane from the intracellular to the extracellular side, corresponding to a putative change from closed to open. This simulation suggested that if an exposed S4 helix is moved through the membrane interior, it would likely create large water defects and possibly drag anions with it into the membrane. It also showed that even this extreme motion has little effect on the stability of the pore domain, enforcing the idea that the S1–S4 domain is relatively flexible, as illustrated in Fig. 15.

As simulations reach longer timescales and become more accurate, and as more structural information about different states becomes available, the study of large-scale conformational changes by computer simulation will no doubt become increasingly interesting and might in fact turn out to be one of at most a handful of techniques that can link different structures in time and tie them to their functional roles.

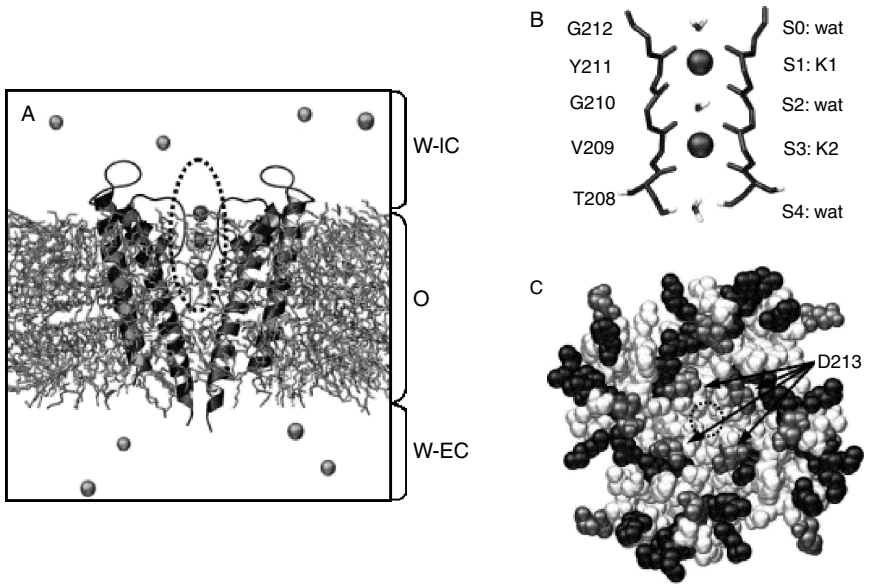

Figure 15. The inner surface of the pore for the three model states: closed (the final structure after 1-ns of simulation based on the crystal structure), expanded (the final structure after simulation Ex3 in the original paper), and relaxed (Rx1 after 11-ns of simulation in the original paper). Reprinted with permission from [190], P. C. Biggin et al., *Biophys. J.* 83, 1867 (2002). © 2002, Biophysical Journal.

3.2.5. Diffusion of Ions in the Channel

Given the presence of multiple K^+ ions within the selectivity filter of the KcsA potassium channel, a number of simulations have looked at the spontaneous motions of different configurations of K^+ ions and water molecules in the filter. Several studies also considered different types of cations in the selectivity filter: Na^+, K^+, Rb^+, Cs^+. Although these simulations are too short, by several orders of magnitude, to give direct information about the conductance of the channel, they provide information about the local interactions in the filter and other parts of the protein. In the crystal structure, the two K^+ ions within the filter occupied S1 and (S3 or S4). The recent 2.0 Å structure actually shows 7 different binding sites, with ion density (at high K^+ concentration) in sites S1–S4 as well as two more sites somewhat outside the filter on the extracellular side and 1 ion in the cavity. Simulations usually have shown K^+ ions at S2 and S4, but sampling and starting structures are an issue.

Interestingly, two independent simulations predicted there was a favorable location for a potassium ion outside the filter, which was confirmed by the recent high-resolution crystal structure [102, 195]. As discussed below, several free-energy calculations have suggested that the difference in free energy between K^+ ions at S2 and S4 and at S1 and S3 is quite low. This is consistent with the high permeation rate of potassium ions.

In multi-nanosecond simulations, concerted motions of the K^+ ions in the filter are usually seen. This is illustrated in Fig. 16, from which it can be seen that the K–W–K (i.e. ion–water–ion) triplet moves in a concerted fashion [195]. This is direct evidence for concerted single-file motion within a potassium channel selectivity filter. Clearly, this complicates attempts to simulate ion flow through potassium channels as a diffusion process. It is also significant that in most simulations, small (generally ~0.5 Å) changes in conformation of the backbone carbonyls occur. In particular, a "flipping" of the carbonyl of V76 is observed. This is likely to be significant, because it suggests that the conformation of the selectivity filter is not static, but can undergo dynamic changes on a timescale comparable to that of passage of the ions through the filter. Indeed, at low potassium concentrations (3 mM), ions are seen in the crystal structure mainly at S1 and S4, with some deformation of the filter consistent with observations in molecular dynamics simulations. Simulations based on the higher resolution crystal structure but using the same force field give very similar results [129, 195].

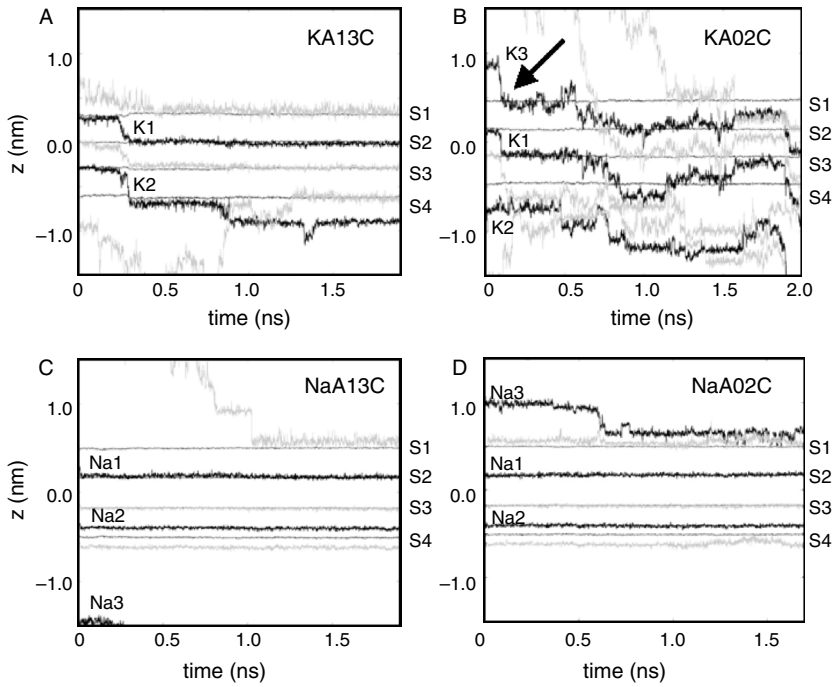

Figure 16. Trajectories (along the pore axis) of K^+ ions (thick black lines) and water molecules (gray lines) for two simulations with different starting configurations in sites S1–S4: (A) KA13C; (B) KA02C. Note that, for clarity, not all water molecules within the filter are shown. The locations on z (pore axis) of the four sites (S1 to S4) defined by the geometric center of the eight oxygen atoms are indicated by the thin black lines. At each point in time, the origin of the coordinate system is defined as the center of gravity of the 16 oxygen atoms that line the selectivity filter. The black arrow in (B) indicates the time at which a K^+ ion enters the selectivity filter from the extracellular mouth (S0) of the channel. Reprinted with permission from [195], I. H. Shrivastava et al., *Biophys. J.* 83, 633 (2002). © 2002, Biophysical Journal.

3.2.6. Energetics of Permeation

A number of groups have used atomistic simulations to explore the energetics of permeation of the KcsA potassium channel. Allen et al. [78] have calculated free-energy profiles for K^+ and Na^+ ions in a simplified model of a potassium channel, based on a channel-shaped hydrophobic pore onto which a model of the KcsA filter is grafted. Their results broadly support the "rigid filter" model of potassium channel selectivity. However, the sensitivity of the results to initial assumptions of the rigidity of the filter is a little unclear. In a subsequent paper, the same authors [196], using a complete model of the protein (but omitting the surrounding bilayer), found that the free-energy differences between K^+ and Na^+ were about half those with the simplified model. Several other groups have calculated potentials of mean force for ions in the selectivity filter. Åqvist and Luzhkov [101] showed that occupancy of sites S2 and S4 of the filter (see Fig. 8B) by two K^+ ions was more favorable (by $\sim$2 kcal/mol) than occupancy of sites S1 and S3. Other configurations were of higher free energy. Thus, a permeation model based on switching of pairs of K^+ ions between these two configurations was proposed. Berneche and Roux [105] used umbrella sampling to calculate a two-dimensional free-energy map describing possible pathways for translocating ions and suggest a plausible mechanism involving correlated motions of at least three ions and water on a relatively flat energy landscape. Based on this map, they used Brownian dynamics simulations to calculate current–voltage curves that gave excellent agreement with experimental measurements of the conductance of the KcsA potassium channel [105]. Combined, these two papers show the power of a hierarchical approach to link atomistic models to macroscopic observables, through potential of mean force calculations.

A another recent study [93] calculated potentials of mean force using free-energy perturbation in KcsA. As such calculations are becoming increasingly feasible on standard

computers, a closer link between microscopic simulations and experimental measurements becomes possible.

3.2.7. Selectivity

Why are potassium channels so selective for potassium over sodium? The key differences between potassium and sodium appear to be only a small difference in radius and in polarizability. On the basis of the x-ray structure of the KcsA potassium channel, it has been suggested that a "rigid" selectivity filter provides stronger cation–oxygen interactions for K^+ ions than for Na^+ ions. Thus, the energetic cost of dehydrating K^+ ions is repaid by ion–protein interactions, whereas ion–protein interactions are too weak to balance the cost of dehydrating Na^+ ions. Several simulations have tried to address this question. The accuracy of ion–protein and ion–water interactions is a key concern for this type of calculation, and errors in common parameters can be quite substantial [197, 198]. For instance, an accurate balance between ion–carbonyl and ion–water interactions is difficult to achieve for different types of cations, and specific parameterization of the filter region has been used by Berneche and Roux [197] and for a different force field for simulations of the voltage gated potassium channel KvAP by Monticelli et al. [194].

The deciding factor for selectivity in channels is that of the free energy of permeation or how the free energy of the system varies as different species of ion pass through the channel. Such calculations can yield the difference between two species of ions at a particular location, in addition to the full potential of mean force for moving a particular type of ion. Allen et al. [196] calculated that the free energy (for a $K^+ \rightarrow Na^+$ transformation) is positive within the filter region, which means it is more favorable for a potassium ion to be in the filter than it is for a sodium ion. However, the exact figure arrived at was somewhat sensitive to the nature of the restraints applied to the filter during the simulation. Åqvist and Luzhkov [101, 199] have performed more detailed free-energy perturbation calculations. Their results also supported the "rigid filter" model of potassium-channel selectivity. However, it should be noted that in all three of these simulation studies, it is not clear that the filter had time to fully "relax" around the different species of cation. Longer molecular dynamics simulations of the KcsA channel with K^+ ions or with Na^+ ions in the filter suggest that the filter may be able to alter its conformation such that Na^+ ions can bind tightly within (and thus block) the filter. The geometry of interaction with Na^+ ions with the filter appears to be different from the geometry of interaction of K^+ ions [129, 195]. Examples of snapshots with Rb^+ and Na^+ in the filter are shown in Fig. 17.

Furthermore, long simulations with either K^+ or Na^+ ions at the extracellular mouth of the filter suggest a degree of selectivity in terms of which ions enter the filter [195, 200]. It is clear that very careful simulations are required to obtain the correct balance of ion–water, ion–protein, and protein deformation energies. There is experimental data for other cations, such as Rb^+ [103, 168]. In principle, these could be simulated too, but they require additional testing of parameters because they are not commonly used in biomolecular simulations.

One of the most recent and quite elaborate studies on the behavior of the selectivity filter and ions in the selectivity filter was carried out by Domene and Sansom [129], in which different cations (Na^+, K^+, Rb^+, Cs^+) were simulated in the high-resolution crystal structure of the KcsA potassium channel. This work can be compared to similar simulations on Na^+ and K^+ in the selectivity filter based on the 1998 crystal structure [195]. These older simulations missed several refinements, such as the inclusion of water molecules behind the selectivity filter. Nonetheless, in both simulations, significant flexibility of the filter was observed, as well as concerted motions of ions and water. In particular, pronounced distortions of the filter occur when no ions are present, which is also found from crystallographic studies at low salt concentration [103]. The two most readily permeant ions, K^+ and Rb^+, are similar in their interactions with the selectivity filter, whereas Na^+ ions tend to distort the filter by binding to a ring of four carbonyl oxygens (see Fig. 17). The larger Cs^+ ions result in a small degree of expansion of the filter relative to the x-ray structure and show some tendency to bind within the gate region of the channel, near the cavity. Although these results are very interesting, it should be kept in mind, however, that ion parameters are difficult to obtain with high accuracy. Further studies in this area would certainly be worthwhile.

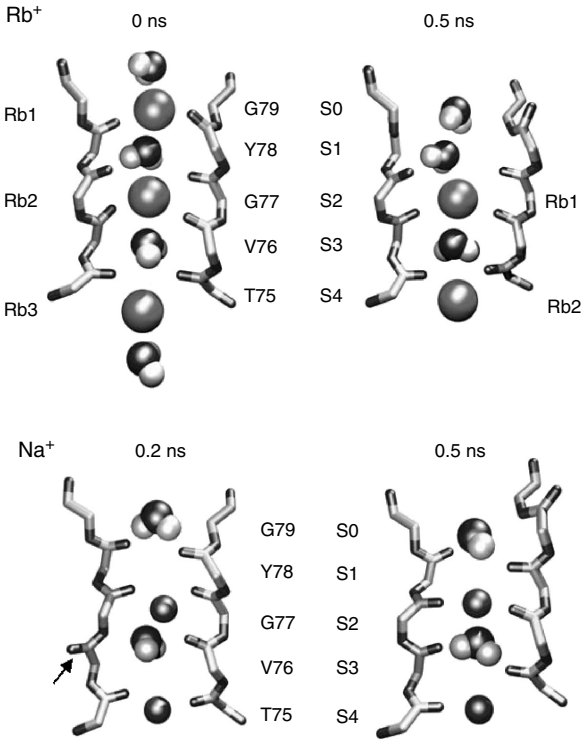

Figure 17. Different effects of cations on the filter, showing snapshots of Rb^+ (Configuration 2) and Na^+ (Configuration 1) in the filter. In both cases, the filter regions (backbone atoms only) of two subunits plus the ions and water molecules within the filter are shown. For the Na^+ simulation, the flip of the carbonyl of V76 is indicated with an arrow. Reprinted with permission from [129], C. Domene et al., *Biophys. J.* 85, 2787 (2003). © 2003, Biophysical Journal.

The recent structure of the calcium-gated potassium channel MthK in an open state suggests which considerable conformational changes take place upon gating. This new structure has not yet been exploited in published simulation studies (it also has a relatively low resolution, which makes simulations more difficult), but this will only be a matter of time. Several groups have built models of what an open version of the KcsA channel might look like, using a variety of methods including purely theoretical methods [190] and extensive mutagenesis with spin labeling for electron spin resonance measurements [178].

3.3. ClC Cl^- Channels

Dutzler et al. [5, 6] unveiled the crystal structure of a transmembrane protein in bacteria, known as the ClC channel, that has subsequently been shown to be a transporter, not an ion channel [201, 202]. Nevertheless, many amino acid sequences of the prokaryotic ClC protein are conserved in their eukaryotic ClC relatives, which are selectively permeable to Cl^- ions. The ClC family of Cl^- channel is present in virtually all tissues—in muscle, heart, brain, kidney, and liver—and is widely expressed in most mammalian cells. By allowing Cl^- ions to cross the membrane, ClC channels perform diverse physiological roles, such as transepithelial transport, control of cellular excitability, cell volume regulation, and regulation of intracellular pH. Genetic alterations of some of these genes are known to be associated with myotonia congenita [203], a muscle disease characterized by stiffness upon sudden movement; Dent's disease [204], an inherited kidney disorder; Bartter's syndrome [205], a salt-wasting renal tubular disorder; and diabetes.

The prototype channel, known as ClC-0, first discovered by Miller [206], is found in *Torpedo electroplax*. Since then, nine different human ClC genes and four plant and bacterial ClC genes have been identified. Many of the salient properties of ClC-type channels have been uncovered using the techniques of molecular cloning and subsequent heterologous expression [207]. Conduction properties differ among the isoforms. For example, the

current–voltage relationship measured from ClC-0 and ClC-2 are linear [206, 208], whereas those measured from other isoforms are either inwardly rectifying (ClC-1) [209] or outwardly rectifying (ClC-3, ClC-4 and ClC-5) [210–214].

The prokaryotic ClC channel is a bulky, large protein, composed of about 14,000 atoms including polar hydrogens. As shown in Fig. 18A, the protein has two independent ion-conducting pathways—it is a double-barreled dimer formed by identical subunits in contact at a broad interface. From the intracellular and extracellular side of the protein, the wide entrances or vestibules in each of the two subunits can be clearly seen (arrows in Fig. 18A). The x-ray structure of the channel, however, represents a closed-state conformation. In the wild-type *Escherichia coli* ClC (EcClC) channel structure, residues from the N-termini of the D, F, and N α-helices constrict the channel, and two of these residues completely block the conduction pore, as shown in Fig. 18B. As we follow the EcClC pore from either the extracellular (top) or intracellular (bottom) opening toward the middle of the pore, it abruptly tapers and vanishes. Thus, before the crystal structure coordinates can be used to investigate the permeation of ions through the channel, a completely open-state structure needs to be created by using molecular dynamics or other means. Moreover, the ion conducting path of the EcClC channel, unlike that of the KcsA channel [3], takes a tortuous course through the protein, instead of being straight and perpendicular to the plane of the membrane. The meandering nature of the ClC pore complicates calculations of the force an ion experiences as it moves through the pore. Perhaps for these reasons, there have been only a few theoretical studies so far that attempt to relate the atomic structure of a ClC channel to the macroscopic properties.

The availability of the x-ray structure of the prokaryotic ClC Cl^- channel has prompted several theoretical investigations. Using a novel computational approach based on the Metropolis Monte Carlo method, Miloshevksy and Jordan [215] trace the ionic pathway through the protein as a Cl^- ion moves along several anion coordinating sites. They also calculate the electrostatic potential energy profiles before and after neutralizing the charges on several key amino acid residues. To carry out an all-atom molecular dynamics simulation of the prokaryotic ClC protein, Cohen and Schulten [216] built an open-state configuration of the channel by moving away the atoms that occlude the pore. They then constructed the profile of the potential of mean force along the ion conducting path.

Because the EcClC protein shares many signature sequence identities with the eukaryotic ClC channels, it is possible to build homology models of these channels based on the structural information provided by Dutzler et al. [5, 6]. With this aim in mind, Corry et al. [217, 218] first altered the x-ray structure of the prokaryotic ClC protein using molecular dynamics to create a set of open-state configurations. They expanded the EcClC conducting pathway to putative open-state by moving the atoms blocking the pore sideways. A set of cylinders of radius 5 Å were set at six points near the centerline of the pore containing the blocking atoms. Atoms inside the cylinders were pushed outward with a strong harmonic force, whereas all other atoms were held near to their initial positions using comparatively

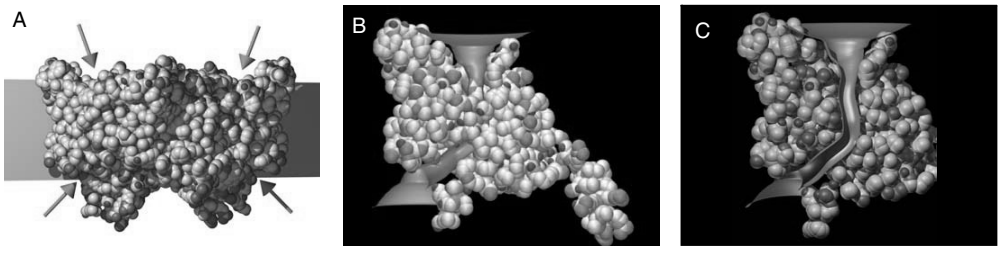

Figure 18. The crystal structure of the bacterial ClC channel. (A) The atomic detail of the crystal structure of the *E. coli* channel shows that the protein is a dimer, composed of two identical subunits. Arrows indicate the pore openings. (B) The front half of one of the two identical subunits is removed to reveal the ion conducting path. Several atoms are occluding the pore. (C) The residues that block the ion conducting path are removed to create an open state model. Modified with permission from [217], B. Corry et al., *Biophys. J.* 86, 846 (2004). © 2004, Biophysical Journal.

weak harmonic constraints. In this way, an open-state channel was molded with a minimum radius of 2.5 Å, which is the smallest radius that would allow passage of both Cl^- and NO_{3^-}, as illustrated in Fig. 18C. The open channel shows that the ClC pore is not axially symmetric like the well-known KcsA potassium channel, but meanders through the protein.

Assuming that the overall structure of the eukaryotic ClC channels, is the same as that of EcClC, Corry et al. [217, 218] converted EcClC to ClC-0 and ClC-1. To do this, they first generated sequence alignments using the ClustalW algorithm, followed by a small amount of manual adjustment, as detailed in Corry et al. [218]. Then, they replaced all nonconserved charged and dipole-containing and pore-lining amino acids to convert EcClC to ClC-0 or ClC-1. Incorporating these homology models into Brownian dynamics, they determined the current–voltage–concentration profiles of ClC-0 and ClC-1. These are illustrated in Fig. 19. The current–voltage relationship of ClC-0 is linear (A), whereas that of ClC-1 is asymmetrical and nonlinear (B). The experimental measurements obtained from ClC-0 [206] are superimposed (open circles) on the simulated data (filled circles). The core conductance is 11.3 ± 0.5 pS, compared to the experimental value of 9.4 ± 0.1 pS. The conductance of ClC-1 obtained from Brownian dynamics simulations is 1.0 pS at -100 mV, much smaller than in ClC-0. At positive voltages, the current across ClC-1 is less than 0.01 pA, until the driving force is increased to $+160$ mV. There are several whole-cell current measurements demonstrating that the ClC-1 channel is inwardly rectifying [209, 219–221], as shown in the inset of Fig. 19B, but no single-channel current–voltage curve for ClC-1 is available in the literature. The estimated value of the ClC-1 conductance is about 1.2 pS [222, 223]. Thus, both the shape of the current–voltage relationship and the conductance determined from Brownian dynamics simulations are in accord with the experimental findings. In Fig. 19, the currents obtained from Brownian dynamics simulations in ClC-0 (C) and ClC-1 (D) by Corry et al. [217], under the applied potential of -80 mV, are plotted against the concentration of Cl^- ions in the reservoirs. The experimental data obtained from ClC-0 are shown in open circles in Fig. 19C and are fitted with a broken line. The solid lines fitted through the data points are calculated from the Michaelis–Menten equation. Again, there is a reasonable agreement between the simulated data and experimental measurements for ClC-0.

Brownian dynamics simulations also reveal the steps involved in ion permeation. As in the KscA K^+ channel, two resident Cl^- ions exist in a stable equilibrium in the ClC channels.

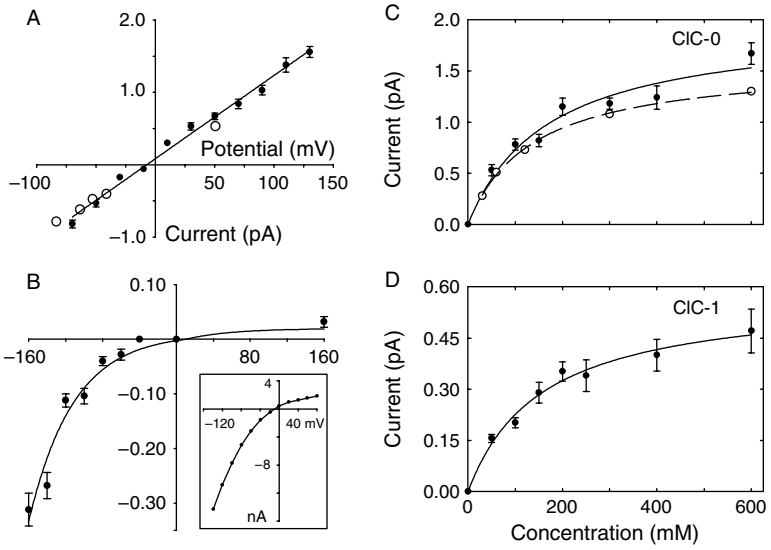

Figure 19. The current–voltage–concentration profiles. The current–voltage relationships for ClC-0 (A) and ClC-1 (B) obtained from Brownian dynamics simulations (filled circles) are compared with the experimental data of Miller [206] (open circles in A) and Bennetts et al. [219]. The outward currents (filled circles) of ClC-0 (C) and ClC-1 (D) are plotted against varying concentrations of NaCl in the reservoirs. The experimental measurements obtained by Tsung-Yu Chen are shown in open circles in (C). Reprinted with permission from [217], B. Corry et al., *Biophys. J.* 86, 846 (2004). © 2004, Biophysical Journal.

When a third ion enters the pore from the intracellular space, this equilibrium is disrupted, and the outermost Cl^- ion is expelled to the extracellular space. The dwell histogram shown in Fig. 20, obtained by counting the average number of Cl^- ions in each thin layer, reveals the regions of the pore where ions preferentially dwell. In both ClC-0 (A) and ClC-1 (B), two ions dwell on the intracellular side of the channel. In the dwell histogram obtained from ClC-1 (Fig. 20B), there is also a third prominent peak, indicating that a third ion spends considerable time in the channel before a successful conduction event occurs.

3.4. The L-Type Calcium Channel

Unlike the KcsA potassium and the bacterial ClC channels, the crystal structure of the calcium channel is not yet available. Thus, to model the calcium channel, one has to solve an inverse problem—in other words, a simplified channel model that captures the essential features of the full atomic details of the protein must be derived through a judicious use of clues from experimental data.

The calcium channel is ubiquitous in excitable cells. The channel is extremely selective against Na^+ ions and exploits a multi-ion Coulomb repulsion mechanism to achieve a high throughput of Ca^{2+} ions. It selects between ions of almost identical radius, the Pauling radii of Na^+ and Ca^{2+} ions being 0.95 and 0.99 Å, respectively. Moreover, the channel permits much larger ions to move across it, such as tetramethylammonium with a radius of about 2.8 Å [224]. Thus, a different mechanism of selectivity from that in the potassium channel must be at play, one that relies on the different charges on the ions. Monovalent ions can permeate the channel in the absence of calcium at much higher levels of conductance than can any divalent ions [225–228], but are blocked when the calcium concentration reaches only 1 μM [225, 229]. These properties of the calcium channel are largely determined by four glutamate residues that line the narrowest segment of the pore, or the selectivity filter.

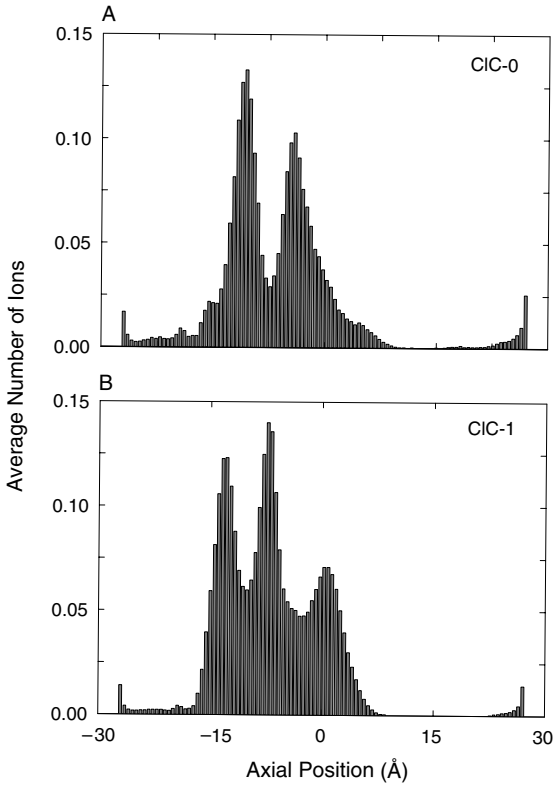

Figure 20. The dwell histograms of ClC-0 (A) and ClC-1 (B). The channel is divided into 100 thin sections, and the average number of ions in each section is calculated over a simulation period (0.4 μs) in the presence of an applied potential of −80 mV. Reprinted with permission from [217], B. Corry et al., *Biophys. J.* 86, 846 (2004). © 2004, Biophysical Journal.

These residues are expected to be highly charged and to strongly bind Ca^{2+} ions in the channel, leading them to block the passage of Na^{+} ions. Mutations of one or more of the glutamate residues lining the selectivity filter have provided many useful insights in selectivity in the calcium channel. The replacement of a glutamate residue with a neutral amino acid severely lowers the conductance of the channel for divalent ions and to a lesser extent for monovalent ions [230]. Also, the block of monovalent currents by divalent ions is severely hampered, only arising at much higher divalent concentrations [231].

Several attempts have been made in the past to construct theoretical models to explain permeation and selectivity in the calcium channel. The first type of proposed models is based on single-file reaction rate theory, in which ions sequentially hop from one site to another [232]. Because of the difficulty in obtaining both high selectivity and throughput with a single binding site [233], these models originally contained two binding sites in which repulsion between ions in neighboring sites increases transit rates [234, 226]. Because the two-site models could not accommodate the mutation data, Dang and McCleskey [235] put forward a new rate model where a single binding site is flanked by lower affinity sites to aid the exit of ions from the central site. Other mechanisms involving single sites have also been developed, such as competition between Ca^{2+} ions for binding sites [231, 236]. Although these models are purely phenomenological and do not take into account the channel shape or charged residues in the protein, they nevertheless have provided many useful insights as to how calcium channels may achieve their selectivity with a high throughput.

Nonner and Eisenberg [42] attempted to relate the observed properties of the calcium channel to its structure with the Poisson–Nernst–Planck theory. They modeled the selectivity filter of the channel as a 10 Å–long cylinder with a radius of 3 Å, to which a 20 Å–long conical vestibule is connected at each end. Four charged glutamate residues, placed along the wall of the cylinder, were allowed to be protonated, and other parameters, such as excess chemical potentials and diffusion coefficients of Na^{+} and Ca^{2+}, were estimated analytically. The results obtained by solving their "extended" Poisson–Nernst–Planck theory accurately reproduce current–voltage relations and block of monovalent currents by divalent ions. The physical basis for the free parameters used to fit the channel data still needs to be elucidated.

Corry et al. [70] proposed a model of the L-type calcium channel, making use of the available information on its structure and conductance properties. Figure 21A shows the transverse section of the three-dimensional model, consisting of inner and outer vestibules and a selectivity filter. The selectivity filter is the most important part of the model and requires a careful design in order to reproduce the observed properties of calcium channels. Two crucial elements, namely, its size and charges on its walls, are determined from the experimental data. The diameter is set to 5.6 Å from the size of tetramethylammonium, the largest permeable ion [224]. The mutation data indicate presence of four negatively charged glutamate residues in the filter region [231]. They modeled the four glutamate residues as four fixed charges located in close proximity, which spread asymmetrically in a spiral pattern 1 Å behind the channel wall. To overcome the large image forces at the intracellular end of the channel, they placed four mouth dipoles, 5 Å in length, with their inner ends 1 Å inside the pore wall. The approximate locations of these charge are indicated in Fig. 21A. Brownian dynamics simulations performed with this model have been very successful in replicating many physiological properties of L-type calcium channels. These include current–voltage curves, saturation of conductance with concentration, selectivity against Na^{+} ions, the anomalous mole fraction effect, attenuation of calcium current by external sodium ions, and the effect of mutating glutamate residues on blocking of sodium current [70].

An intuitive understanding of how these properties follow from the ion-channel interactions can be gleaned from a study of the potential energy profiles of ions in the channel. The ion-channel interaction has basically two components: a repulsive force due to the induced charges on the protein boundary and the electrostatic interaction of the ion with charge residues and dipoles in the channel wall. The simple Coulomb interaction between two ions is modified in the channel environment because they also interact via the surface charges induced by each other. Each of the four potential energy profiles shown in Fig. 21B is constructed by calculating the potential energy of the ion held at a fixed z position and then repeating these calculations at 1 Å steps. With no fixed charges on the protein wall, an ion

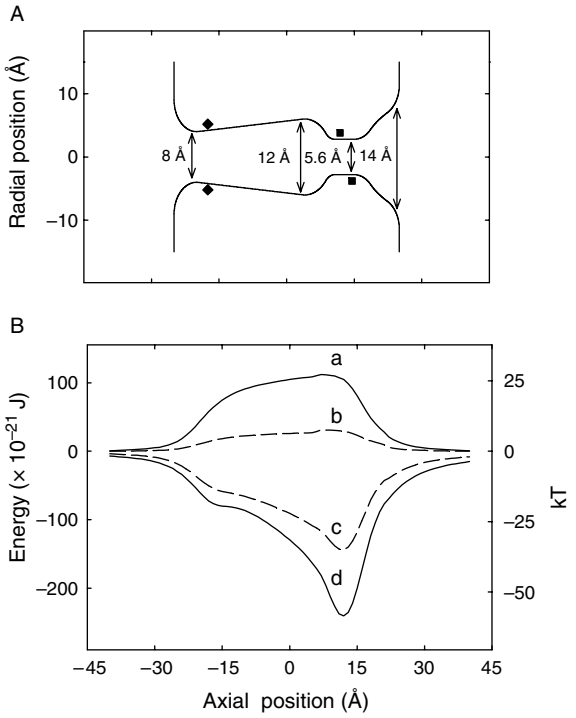

Figure 21. Model calcium channel and electrostatic energy profiles. (A) A three-dimensional channel model is generated by rotating the curves about the central axis by 180°. The positions of two of the four glutamate groups are shown by the squares, and the inner end of two of the four mouth dipoles by the diamonds. (B) Potential energy of an ion traversing the channel is plotted for a Ca^{2+} ion (a) and a Na^{+} ion (b) in the absence of any fixed charges. With the glutamate groups and mouth dipoles included, the profiles are replotted for Ca^{2+} ion (d) and a Na^{+} ion (c). Reprinted with permission from [70], B. Corry et al., *Biophys. J.* 80, 195 (2001). © 2001, Biophysical Journal.

entering the channel meets a steeply rising potential barrier (curve a for a Ca^{2+} ion, curve b for a Na^{+} ion). When the ring of four mouth dipoles and four glutamate charges are included in the model, this barrier is turned into a deep well. The depth of the well is 36 kT for a Na^{+} ion (c) and 58 kT for a Ca^{2+} (d). The well is deep enough so that two Na^{+} ions or one Ca^{2+} would be permanently trapped in the selectivity filter. When a second Ca^{2+} (or a third Na^{+} ion) enters the channel from the extracellular space, two Ca^{2+} (or three Na^{+}) ions can coexist in the filter region in a semistable equilibrium, until the resident ion on the left climbs over a small energy barrier via thermal fluctuations and exits the channel.

Of the many properties of the calcium channels, the most interesting ones are associated with the blocking effects. In the anomalous mole fraction effect, the channel current vanishes at a certain range of Ca^{2+} concentrations in the presence of a fixed 150 mM Na^{+}, as shown in the inset of Fig. 22A. The Brownian dynamics results (Fig. 22A) indicate that the rapid drop and subsequent vanishing of the channel current is due to the blocking of Na^{+} current by Ca^{2+} ions. Once the Ca^{2+} concentration is high enough to allow two Ca^{2+} ions in the filter, the channel starts conducting again but now Ca^{2+} ions instead of Na^{+}. Although sodium ions cannot block calcium, their presence in the vestibule can nevertheless retard entry of a second Ca^{2+} ion necessary for conduction. As illustrated in Fig. 22B, the predicted reduction in the channel current with increasing Na^{+} concentration is in excellent agreement with the experimental data. A final example is the effect of mutating one of the glutamate residues to neutral glutamine on the blocking of Na^{+} current (Fig. 22C). The mutation leads to a reduction in the depth of the potential well compared to the native case so that entry of a Ca^{2+} ion in the channel is delayed, and the blocking occurs at a higher Ca^{2+} concentration. Trends in the data (inset of C) are again reproduced by the Brownian dynamics simulations.

The level of agreement between theory and experiment obtained from Brownian dynamics studies of the L-type calcium channel is substantial and should encourage further

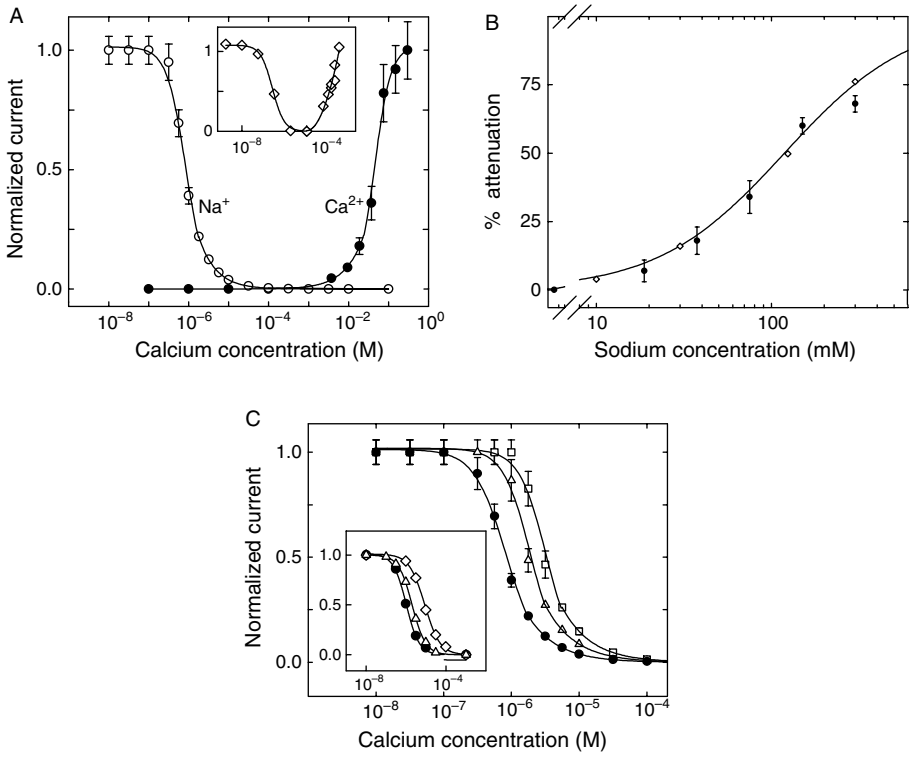

Figure 22. Brownian dynamics simulations of the L-type calcium channel. (A) Simulations accurately reproduce the mole fraction effect. Ca^{2+} (filled circles) and Na^{+} (open circles) current passing through the channel normalized by the maximum value of each is plotted against the Ca^{2+} concentrations while keeping the Na^{+} concentration fixed at 0.15 M. Experimental results [226] are shown in the inset. (B) Ca^{2+} current is attenuated by Na^{+} ions. The percentage reduction in the channel current is plotted against Na^{+} concentration while the Ca^{2+} concentration is fixed at 0.15 M (filled circles). The open diamonds and dotted line show the experimental data [276]. (C) The effect of removing glutamate charges on channel selectivity. The Na^{+} current passing through the channel at different Ca^{2+} concentrations with all four glutamate charges in place (filled circles), the outermost glutamate removed (triangles), and the innermost glutamate removed (squares). Experimental data for wild type (filled circles) and for single glutamate to neutral glutamine mutations of two different residues (triangles and diamonds) are shown in the inset [231]. In all cases a driving potential of −0.2 V is applied. Reprinted with permission from [70], B. Corry et al., *Biophys. J.* 80, 195 (2001). © 2001, Biophysical Journal.

applications of the Brownian dynamics method to modeling of other ion channels with limited structural information.

3.5. Other Biological Ion Channels

3.5.1. Mechanosensitive Channels

Several species of mechanosensitive channels have been identified, and the crystal structures of the large conductance mechanosensitive channel (MscL) from *Mycobacterium tuberculosis* at 3.5 Å and the small conductance mechanosensitive channel (MscS) from *E. coli* at 3.9 Å resoultion have been solved [237]. Both these channels have intriguing properties. The mechanosensitive MscS channel is gated both by tension and voltage and appears to have arginine residues exposed to the membrane that are important for voltage sensing [238]. This is particularly interesting in the context of voltage-gated sodium, calcium, and potassium channels that also contain highly conserved arginines [239]. The MscL channel is sensitive to tension only. It has such a large conductance in the open state it must undergo very substantial conformational changes from the crystal structure, which appears to be closed. The MscL channel is a pentameric protein consisting of two concentric rings of helices. The TM1 helices line the pore, the TM2 helices form the outer ring.

The mechanosensitve MscL channel has been the subject of a significant number of simulation and modeling studies aimed at understanding the gating mechanism, using the crystal

structure or homology models of the *E. coli* MscL (Eco-MscL). The first simulations studied the crystal structure and several mutants to identify mobile and less mobile regions in the structure and to get hypotheses for further experimental studies [240, 241]. The most interesting question is perhaps how the structure changes under the influence of membrane tension. Several hypotheses have been put forward, falling in two broad categories. In the first, the TM1 and TM2 helices might form a larger "barrel." In this scenario, the TM2 helix might be the "tension sensor" and undergo a significant conformational change that eventually causes a change in TM1 as well to open the channel. Another hypothesis assumes that the TM1 and TM2 rings of helices might move together in an "iris-like" motion that opens the channel, analogous to the lens of some cameras, while keeping the direct interactions between TM1 and TM2 helices the same. The net effect in both cases is a sharp increase in the pore radius. This is illustrated in Fig. 23. The first possibility seems to be suggested by molecular dynamics simulations that apply a surface tension to the membrane or an explicit force on the protein directly [241–243], although the TM2 helix is very hydrophobic, and therefore not likely to line a large water-filled pore. The advantage of such simulations is that no preconceived notion of the mechanism is imposed, but a significant drawback is that such high surface tensions or forces are required to see structural changes on a nanosecond timescale that there is a considerable risk of simulation artifacts.

The second mechanism, the iris mechanism, has been investigated by molecular modeling and extensive mutagenesis experiments [244]. The mutagenesis experiments are consistent with this mechanism, and the resulting pore is larger than for the hypothetical barrel stave pore formed by parallel helices. Electron paramagnetic resonance experiments that look at the accessibility to hydrophilic and hydrophobic spin quenchers and the dynamics of every single residue in MscL also support the iris mechanism [245]. Finally, normal mode analyses of both the crystal structure and modeled intermediates also suggest this mechanism [246]. Eventually, a crystal structure of MscL trapped in the open state, which would probably be a mutant that might be based on modeling, might help to explain the different results and to hone further the battery of computational and experimental methods used to obtain models of states that are not directly accessible by high-resolution structural methods.

3.5.2. OmpF

Porins form large trimeric pores in the outer membrane of gram-negative bacteria, which passively transport small molecules down their concentration gradients. OmpF is the best known example of this family. It is a general diffusion pore from the outer membrane of *E. coli* that transports molecules up to ~650 Da. It shows gating behavior, but the molecular basis and the physiological relevance of this phenomenon are poorly understood [127]. OmpF is weakly cation selective, and its selectivity depends on the ionic strength of the solution. Porins have relatively long loops on the extracellular side and short turns on the intracellular side. The L3 loops fold back into the pore and form the so-called eyelet region or constriction zone, as shown in Fig. 24. The arrangement of oppositely charged residues on opposite walls of the narrowest region of the pore creates a strong transverse electrostatic field, which is expected to have a profound effect on the behavior of ions, water, and permeating molecules in this region.

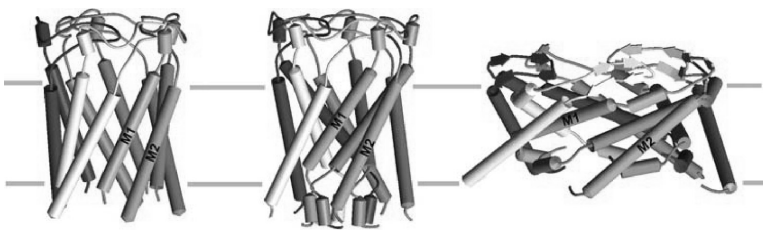

Figure 23. A hypothetical barrel-stave open conformation (left), a closed-state model of *E. coli* MscL built by homology to MscL (center), and a hypothetical tilted open conformation (right) with strong experimental support of Bentazos et al. [274] and Sukharev et al. [275]. Figures provided by Dr. Sukharev.

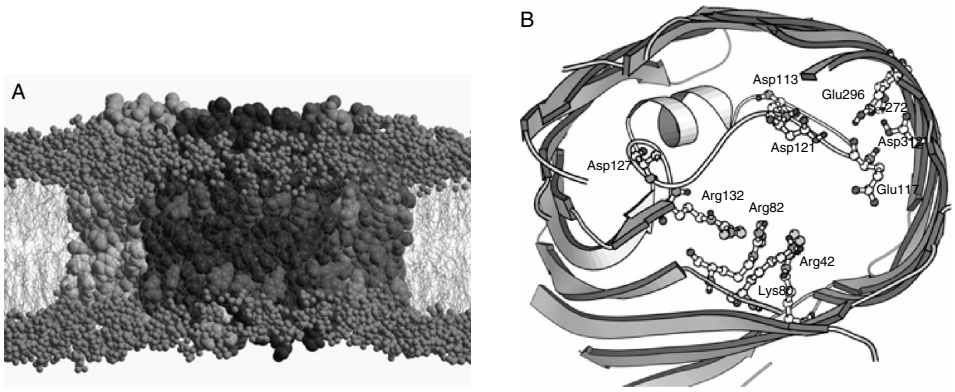

Figure 24. The OmpF porin. (A) In the simulation model, OmpF porin is embedded in a palmitoyl-oleoyl-phosphatidylethanolamine bilayer. The total system contains about 70,000 atoms. (B) In the closeup of the eyelet region of one of the OmpF monomers, there is a significant separation of positive charges and negative charges across the eyelet, resulting in a large local electric field.

OmpF has been extensively studied by electrophysiology methods, although not all of this data is straightforward to interpret in terms of the properties of a single protein. Nonetheless, OmpF is an attractive model pore for calculations because its high-resolution structure is known, as are structures of a range of mutants with altered electrophysiological properties. This combination of high-resolution structures and electrophysiological data allows systematic testing and calibrating of simulation methods.

OmpF has been the topic of a number of realistic molecular dynamics studies [77, 127, 247, 248] as well as Brownian dynamics [92, 249–251] and Poisson–Nernst–Planck calculations [92]. The crystal structure of OmpF embedded in a simulation model for molecular dynamics simulations, including lipids and solvent, is shown in Fig. 16. A molecular dynamics simulation of OmpF in a POPE bilayer [77] was the first simulation of a large protein channel in a full bilayer environment. The 1-ns simulation revealed complex, nonbulk properties of water within the transbilayer pore. Within the pore, water diffusion coefficients were reduced by up to a factor of 10, relative to bulk. The transverse electrostatic field in the pore resulted in a high degree of alignment of the water dipoles. In a more recent study, the orientation of permeating small dipolar molecules was calculated. Both alanine and glucose strongly oriented in the narrow part of the pore, but not appreciably outside this part [247]. Im and Roux [73] described in great detail the permeation of cations and anions obtained from atomistic molecular dynamics simulations of OmpF in a bilayer with 1 M KCl, based on a 5-ns simulation. They found different permeation paths for cations and anions in most of the channel.

This is consistent with a number of Brownian dynamics of ion flow through OmpF that showed that cations and anions follow distinct pathways with little overlap through the pore [92, 251]. It appears that anions require cations to permeate efficiently. OmpF is slightly selective for cations over anions, but ion pair formation counteracts this to some extent. Preliminary simulations of the same system with different salt concentrations and an applied electric field have also been described by Robertson and Tieleman [127].

Although OmpF is a wide pore with a very large conductance, the molecular dynamics calculations so far have not been long enough to calculate reliably a conductance. However, several continuum methods and Brownian dynamics simulations have also been applied to OmpF. A recent study [92] compared ion distributions obtained from the nonlinear Poisson–Boltzmann equation, Brownian dynamics, and molecular dynamics in OmpF. All three methods gave very similar results, with a most conspicuous feature the separation of cations and anions in two distinct sets of pathways through the channel that was observed in the earlier molecular dynamics study. This is interesting, because it shows that treating OmpF as a rigid protein and the solvent as a dielectric constant seems a reasonable approximation, probably because of the large size of the pore. The Poisson–Nernst–Planck theory and Brownian dynamics simulations were used to calculate the conductance and the reversal potential

(a measure of the selectivity of the channel). The Poisson–Nernst–Planck and Brownian dynamics gave similar results, both close to experiment, for the reversal potential, but the former overestimated the conductance by about 50% [92].

OmpF porin is an interesting model system to study the interactions of permeating molecules with the channel. Experimentally, the noise in single-channel measurements of OmpF in the presence of permeating molecules can be analyzed to reveal a large amount of information about the interactions of such molecules. For example, the binding and unbinding of an antibiotic could be followed on a single-molecule level, and molecular modeling was used to suggest where and in which orientation this molecule was binding [252]. Robertson and Tieleman [247] have used biased molecular dynamics simulations in which alanine and methylglucose were pulled through OmpF. Although the pulling rate was significantly higher than the normal permeation rate, structural perturbation of the protein was minimal. During the permeation process, both alanine and methylglucose aligned strongly in the electric field in the eyelet region. Binding of the permeating dipolar molecules in the eyelet region was not observed, which could be because of the small size of the permeating molecules.

3.5.3. Alamethicin

Alamethicin (Alm) is a 20-residue Aib-rich channel-forming peptide, a member of the family of peptaibols. It has intensively been studied by experimental and computational methods (for reviews, see Refs. [14, 96]). There exist several variants, including covalently linked dimers of alamethicin [253] and peptides, in which the Aib residues have been replaced by leucine [254]. Alamethicin forms channels with well-defined conductance levels that correspond to channels formed by different numbers of peptides. Tieleman et al. [96, 255] have done a number of simulation studies in a palmitoyl-oleoyl-phosphatidylcholine lipid bilayer on these and related channel models to examine the conformational stability of $N = 4$ to 8 helix bundle models, and to attempt to link the models with experimental conductance data. These simulations are of duration comparable to the mean passage time of a single ion through such a channel ($\sim$5 ns is equivalent to an ionic conductance of 250 pS at 125 mV). The simulations suggest that the smallest observable conductance probably corresponds to an aggregate of five helices.

Because of its simplicity, alamethicin has also been a useful test system to investigate the effect of different simulation algorithms [96], and for one particular system (N6, a parallel hexameric bundle), a simulation has been extended to 100 ns [96], one the longest simulations on a channel to date. In this fashion we obtained a validated "best guess" model for at least one conductance level of the Alm channel, which should prove useful as the basis for future, more indepth calculations of channel electrostatics and permeation models.

Starostin et al. [256] designed a variant of alamethicin, called K18. In this peptide, the glutamate or glutamine (both occur) in position 18 has been replaced by a lysine that points into the pore, and two alamethicin peptides have been covalently coupled. The resulting peptide shows preferential stabilization of half the channel levels of normal alamethicin, suggesting pairs of helices insert simultaneously and contribute to the channels. This makes it easier to determine the number of helices in a given measured conductance level. A second interesting property of K18 is that it forms channels with a pH-dependent selectivity [257]. Simulations of channel models formed by this peptide suggest why the experimentally determined selectivity for chloride over potassium is modest despite a high positive charge inside the channel. The channel is sufficiently wide for several chloride ions to be present, significantly decreasing the effective charge. This would lower the barrier for potassium ions. Because this channel is relatively simple, molecular modeling and additional simulations could be used to try to predict the effect of different modifications of the pore lining residues. Thus we could design a more anion-selective version of this channel, which could then be synthesized and experimentally tested.

3.5.4. Other Channels Formed by Peptides

In addition to the alamethicin channel already mentioned, simulations have studied a large number of simple channels formed by peptides. In many cases, these studies use only the predicted transmembrane fragment of larger proteins.

LS2 is a synthetic peptide consisting solely of serines and leucines that forms tetrameric proton-permeable helix bundles [258]. Models of LS2 have been built by several groups [259, 260], but critical comparison of these models with experimental conductance data has been difficult.

A second much-studied proton channel is Influenza A M2 (97 amino acids). This protein homo-tetramerizes to form a H^+-permeable channel activated by low pH [261]. M2 is an important system because it is the target of the anti-influenza drug amantadine. It is also important for computational studies because of the large amount of structural biology efforts directed at it, including solid-state nuclear magnetic resonance and site-specific labeling for Fourier-transform infrared (FTIR) spectroscopic measurements. It has been shown that a synthetic peptide corresponding to the single transmembrane helix of M2 will form ion channels in lipid bilayers, and there have been several structural studies of this peptide in lipid bilayers [262–264], as well as a significant number of modeling attempts [109, 265–267]. The pore is quite narrow, containing a number of water molecules, and is constricted toward its C-terminal mouth by the inward-facing His37 residues that are believed to contribute to gating of the channel [268]. Together, these simulations have shown a range of possible structures, but it remains difficult to decide which one is the most accurate structure. The structures vary in crossing angles of the four helices and in other details of the helical packing.

Simulations have also begun to consider proton transport directly, which will be an exciting direction in the future. The pH gating mechanism of M2 is controversial, with two main mechanisms postulated [269]. In one, pore-blocking histidines shuttle protons between two sites on a histidine. In the second, histidines become charged, move away from each other, and thus open the channel. Analyses of experimental data suggests that the first mechanism might be more likely [269], whereas several simulations have suggested the second [270]. No doubt this will receive further attention in the near future. Only very recently has actual proton transport been simulated in this channel, using the MS-EVB theory, but this has not yet included reactions with the histidines [270].

A third example of a peptide channel is the M2δ channel, a channel formed by five peptides with the sequence of the M2 transmembrane helix of the nicotinic acetylcholine receptor [271]. This peptide channel has the approximate conductance of the whole channel and has been studied by simulations [272]. As the structure of the nicotinic acetylcholine receptor is becoming increasingly accurate and now approaches atomistic resolution in the transmembrane domain [273], it seems likely there will be an increase in simulation studies of the transmembrane domains of the nicotinic receptor and ultimately of the entire protein.

Several models have also been made of channels formed by peptides that are part of viral ion channels, such as VPU from HIV and NB from another strain of influenza. Several papers have been reviewed recently elsewhere [268]. A challenge remains as to how to validate models. Simulations typically show major instabilities but can be metastable if a structure is not correct. Probably the most powerful way of validating models would be a method to calculate the conductance of a model, which can be measured very accurately. Unfortunately, despite recent progress, particularly on gramicidin A, OmpF, and KcsA described above, this is not yet possible in a generally reliable way.

4. CONCLUSIONS

There has been an enormous stride in modeling and simulation of ion channels in the past 5 years. This progress has been brought about by a number of factors, including the availability of crystal structures of physiologically relevant ion channels, the obvious relevance of ion channels for biomedical and pharmaceutical research, the comparatively simple function and basic science of ion channels, the development of efficient and sophisticated simulation and modeling software, and the rapid increase in computer power available to an increasing number of researchers. In this review, we have attempted to summarize some of these recent advances in ion channel research. Of the three permeation models currently in use, the Poisson–Nernst–Planck theory can only be applied reliably for biological nanotubes whose

radius is larger than 2 Debye lengths, or about 16 Å. The most appropriate tools for studying ionic channels that are selectively permeable to a specific ionic species are molecular and Brownian dynamics simulations. Brownian dynamics simulations enable calculation of conductance properties, whereas molecular dynamics can provide input and justification for Brownian dynamics as well as explaining finer details such as size-based selectivity. Because molecular dynamics simulations include all atomic detail and can deal with protein flexibility and conformational changes, they have successfully been used in a large number of studies to simulate local changes in structure and diffusion of water and ions, as well as to calculate potentials of mean force for ions in channels that can be used for Brownian dynamics simulations or kinetic theories.

Both methods have unjustified approximations and deficiencies that need to be better understood and improved in future work. For example, the use of continuum electrostatics in calculation of forces in Brownian dynamics simulations needs to be better validated by appealing to molecular dynamics. Here, water is treated as a continuum, and the effects of solvation and the structure of water are taken into account by frictional and random forces acting on ions. Inferences made from macroscopic electrostatics are valid only in the regions that are large compared to the diameters of water and ion molecules. In the narrow, constricted region of the channel, whose radius may be only $\sim$2 Å, the representation of the dielectric as a continuous medium is a poor approximation. Molecular dynamics simulations are limited in timescale, system size, and the accuracy of the description of atomic interactions. It cannot predict channel conductance, which is the most reliably measured quantity. The timescale that is accessible depends mostly on the speed of computers, software, and algorithmic improvements, all of which will combine in the near future to allow simulations of several orders of magnitude longer than currently possible. Similarly, the force fields employed in molecular dynamics simulations need to be improved by including the polarization effects, perhaps using *ab initio* molecular dynamics as a guide in this process.

Because molecular dynamics simulations rely on atomic-detail structure of a channel, accurate structural information is essential for using this tool in structure–function studies. On the other hand, the simplified models used for Brownian dynamics, which may be construed as a simplified representation of the real microstructure of the channel, may adequately summarize the experimental observations and yield a set of testable predictions that can be compared with patch-clamp recordings. Thus, for this purpose, a detailed tertiary structure is not essential for Brownian dynamics—knowledge of the gross shape of the channel and the approximate locations of the charged residues in the channel wall appear to be sufficient for this purpose. Future developments in the field will depend on the success of the protein chemists and structural biologists in resolving high-resolution structures of membrane proteins, as well as a further refinement of computational tools. Thus, one would like to see the development of a new computational tool that combines the two powerful computational techniques currently available—Brownian dynamics and molecular dynamics. In the wide region of the channel and the vestibules, the motion of charged particles can reliably be simulated with the semimicroscopic Brownian dynamics, whereas the motion of the atoms forming the channel wall and the interaction of the permeating ions with water molecules need to be elucidated by molecular dynamics calculations.

ACKNOWLEDGMENTS

S. H. C. is supported by grants from the Australian Research Council, the National Health & Medical Research Council of Australia. D. P. T is an Alberta Heritage Foundation for Medical Research Scholar. Work in D. P. T.'s laboratory is supported by the Canadian Institutes for Health Research and the National Science and Engineering Research Council. We thank our collaborators Toby Allen, Ben Corry, Scott Edwards, Matthew Hoyles, Serdar Kuyucak, Siu-Cheung Li, and Megan O'Mara, who have contributed to the Brownian dynamics and molecular dynamics studies of channels reported in this review, and Marian Zlomislic for her critical comments.

REFERENCES

1. E. Neher and B. Sakmann, *Nature* 260, 799 (1976).
2. O. P. Hamill, A. Marty, E. Neher, B. Sakmann, and F. J. Sigworth, *Pflügers Arch.* 391, 85 (1981).
3. D. A. Doyle, J. M. Cabral, R. A. Pfuetzner, A. Kuo, J. M. Gulbis, S. L. Cohen, B. T. Chait, and R. MacKinnon, *Science* 280, 69 (1998).
4. G. Chang, R. H. Spencer, A. T. Lee, M. T. Barclay, and D. C. Rees, *Science* 282, 2220 (1998).
5. R. Dutzler, E. B. Campbell, M. Cadene, B. T. Chait, and R. MacKinnon, *Nature* 415, 287 (2002).
6. R. Dutzler, E. B. Campbell, and R. MacKinnon, *Science* 300, 108 (2003).
7. R. B. Bass, P. Stropo, M. Barclay, and D. C. Rees, *Science* 298, 1582 (2002).
8. B. Hille, "Ion Channels of Excitable Membranes," 3rd edn, Sinauer Associates, Sunderland, MA, 2001.
9. K. E. Cooper, E. Jakobsson, and P. Wolynes, *Prog. Biophys. Mol. Biol.* 46, 51 (1985).
10. M. B. Partenskii and P. C. Jordan, *Q. Rev. Biophys.* 25, 477 (1992).
11. B. Roux and M. Karplus, *Ann. Rev. Biophys. Biomol. Struct.* 23, 731 (1994).
12. R. S. Eisenberg, *J. Membr. Biol.* 150, 1 (1966).
13. R. S. Eisenberg, *J. Membr. Biol.* 171, 1 (1999).
14. D. P. Tieleman, P. C. Biggin, G. R. Smith, and M. S. P. Sansom, *Q. Rev. Biophys.* 34, 473 (2001).
15. S. Kuyucak, O. S. Andersen, and S. H. Chung, *Rep. Prog. Phys.* 64, 1427 (2001).
16. W. Nonner, D. P. Chen, and B. Eisenberg, *J. Gen. Physiol.* 113, 773 (1999).
17. E. W. McClesky, *J. Gen. Physiol.* 113, 765 (1999).
18. C. Miller, *J. Gen. Physiol.* 113, 783 (1999).
19. D. G. Levitt, *J. Gen. Physiol.* 113, 789 (1999).
20. D. G. Levitt, *Annu. Rev. Biophys. Biophys. Chem.* 15, 29 (1986).
21. J. O'M Bokris and A. K. N. Reddy, in "Modern Electrochemistry," Vol. 1. Plenum, New York, 1970.
22. B. Honig and A. Nicholls, *Science* 268, 1144 (1995).
23. D. G. Levitt, *Biophys. J.* 48, 19 (1985).
24. P. C. Jordan, R. J. Bacquet, J. A. McCammon, and P. Tran, *Biophys. J.* 55, 1041 (1989).
25. M. Cai and P. C. Jordan, *Biophys. J.* 57, 883 (1990).
26. R. Sankararamakrishnan, C. Adcock, and M. S. P. Sansom, *Biophys. J.* 71, 1659 (1996).
27. P. Weetman, S. Goldman, and C. G. Gray, *J. Phys. Chem.* 101, 6073 (1997).
28. C. Adcock, G. R. Smith, and M. S. P. Sansom, *Biophys. J.* 75, 1211 (1998).
29. W. Cheng, C. X. Wang, W. Z. Chen, Y. W Xu, and Y. Y. Shi, *Eur. Biophys. J.* 27, 105 (1998).
30. T. K. Rostovtseva, V. M. Aguilelaa, I. Vodyanoy, S. M. Bezrukov, and V. A. Parsegian, *Biophys. J.* 75, 1783 (1998).
31. M. S. P. Sansom, C. Adcock, and G. R. Smith, *J. Struct. Biol.* 121, 246 (1998).
32. G. G. Dieckmann, J. D. Lear, Q. Zhong, M. L. Klein, W. F. DeGrado, and K. A. Sharp, *Biophys. J.* 76, 618 (1999).
33. K. M. Ranatunga, C. Adcock, I. D. Kerr, G. R. Smith, and M. S. P. Sansom, *Theor. Chem. Acc.* 101, 97 (1999).
34. P. Smejtek, M. Mense, R. Word, and S. Wang, *J. Membr. Biol.* 167, 151 (1999).
35. B. Roux, B. Berněche, and W. Im, *Biochemistry* 39, 13295 (2000).
36. P. Debye and E. Hückel, *Physik. Zeitschr.* 24, 185 (1923).
37. N. W. Ashcroft and N. D. Mermin, in "Solid State Physics." Holt, Rinehart and Winston, New York, 1976.
38. E. Mason and E. McDaniel, in "Transport Properties of Ions in Gases." John Wiley, New York, 1988.
39. J. S. Newman, in "Electrochemical Systems." Prentice Hall, Englewood Cliffs, NJ, 1991.
40. T. F. Weiss, in "Cellular Biophysics," Vols. 1, 2. MIT Press, Cambridge, MA, 1996.
41. D. Chen, J. Lear, and R. S. Eisenberg, *Biophys. J.* 72, 97 (1997).
42. W. Nonner and R. S. Eisenberg, *Biophys. J.* 75, 1287 (1998).
43. D. P. Chen, L. Xu, A. Tripathy, G. Meissner, and R. S. Eisenberg, *Biophys. J.* 76, 1346 (1999).
44. M. G. Kurnikova, R. D. Coalson, P. Graf, and A. Nitzan, *Biophys. J.* 76, 642 (1999).
45. A. E. Cardenas, R. D. Coalson, and M. G. Kurnikova, *Biophys. J.* 79, 80 (2000).
46. U. Hollerbach, D. P. Chen, D. D. Busath, and B. Eisesnberg, *Langmuir* 16, 5509 (2000).
47. U. Hollerbach and R. S. Eisenberg, *Langmuir* 18, 3626 (2002).
48. B. Corry, S. Kuyucak, and S. H. Chung, *Biophys. J.* 78, 2364 (2000).
49. A. Syganow and E. von Kitzing, *J. Phys. Chem.* 99, 12030 (1995).
50. A. Syganow and E. von Kitzing, *Biophys. J.* 76, 768 (1999).
51. A. Syganow and E. von Kitzing, *Eur. Biophys. J.* 28, 393 (1999).
52. P. Graf, A. Nitzan, M. G. Kurnikova, and R. D. Coalson, *J. Phys. Chem. B* 104, 12324 (2000).
53. Z. Schuss, B. Nadler, and R. S. Eisenberg, *Phys. Rev. E* 64, 0361161 (2001).
54. A. Mamonov, R. D. Coalson, P. Graf, and M. G. Kurnikova, *Biophys. J.* 82, 209a (2002).
55. R. D. Coalson, M. G. Kurnikova, P. Graf, and A. Nitzan, *Biophys. J.* 82, 340a (2002).
56. B. Corry, S. Kuyucak, and S. H. Chung, *Biophys. J.* 84, 3594 (2003).
57. B. Nadler, U. Hollerbach, and R. S. Eisenberg, *Phys. Rev. E.* 68, 021905 (2003).
58. F. Reif, in "Fundamentals of Statistical and Thermal Physics." McGraw-Hill Kogakusha, Tokyo, 1965.
59. R. Zwanzig, in "Nonequilibrium Statistical Mechanics." Oxford University Press, Oxford, 2002.
60. W. F. van Gunsteren, H. J. C. Berendsen, and J. A. C. Rullmann, *Mol. Phys.* 44, 69 (1981).
61. W. F. van Gunsteren and H. J. C. Berendsen, *Mol. Phys.* 45, 637 (1982).
62. M. Hoyles, S. Kuyucak, and S. H. Chung, *Phys. Rev. E* 58, 3654 (1998).

63. L. G. Nilsson and J. A. Padró, *Mol. Phys.* 71, 355 (1990).
64. S. Z. Wan, C. X. Wang, and Y. Y. Shi, *Mol. Phys.* 93, 901 (1998).
65. E. Jakobsson and S. W. Chiu, *Biophys. J.* 52, 33 (1987).
66. S. Bek and E. Jakobsson, *Biophys. J.* 66, 1028 (1994).
67. S. C. Li, M. Hoyles, S. Kuyucak, and S. H. Chung, *Biophys. J.* 74, 37 (1998).
68. S. H. Chung, M. Hoyles, T. W. Allen, and S. Kuyucak, *Biophys. J.* 75, 793 (1998).
69. S. H. Chung, T. W. Allen, M. Hoyles, and S. Kuyucak, *Biophys. J.* 77, 2517 (1999).
70. B. Corry, T. W. Allen, S. Kuyucak, and S. H. Chung, *Biophys. J.* 80, 195 (2001).
71. S. H. Chung, T. W. Allen, and S. Kuyucak, *Biophys. J.* 82, 628 (2002).
72. S. H. Chung, T. W. Allen, and S. Kuyucak, *Biophys. J.* 83, 263 (2002).
73. W. Im, S. Seefeld, and B. Roux, *Biophys. J.* 79, 788 (2000).
74. B. Corry, M. Hoyles, T. W. Allen, M. Walker, S. Kuyucak, and S. H. Chung, *Biophys. J.* 82, 1975 (2002).
75. M. S. P. Sansom, G. R. Smith, C. Adcock, and P. C. Biggin, *Biophys. J.* 73, 2404 (1997).
76. M. E. Green and J. Lu, *J. Phys. Chem. B* 101, 6512 (1997).
77. D. P. Tieleman and H. J. C. Berendsen, *Biophys. J.* 74, 2786 (1998).
78. T. W. Allen, S. Kuyucak, and S. H. Chung, *J. Chem. Phys.* 111, 7985 (1999).
79. S. Garofoli and P. C. Jordan, *Biophys. J.* 84, 2814 (2003).
80. T. Hansson, C. Oostenbrink, and W. F. van Gunsteren, *Curr. Opin. Struct. Biol.* 12, 190 (2002).
81. S. J. Weiner, P. A. Kollman, D. A. Case, U. C. Singh, C. Ghio, G. Alagona, S. Profeta, and P. Weiner, *J. Am. Chem. Soc.* 106, 765 (1984).
82. B. R. Brooks, R. E. Bruccoleri, B. D. Olafson, D. J. States, S. Swaminathan, and M. Karplus, *J. Comp. Chem.* 4, 187 (1983).
83. J. Hermans, H. J. C. Berendsen, W. F. van Gunsteren, and J. P. M. Postma, *Biopolymers* 23, 1513 (1984).
84. E. Lindahl, B. Hess, and D. van der Spoel, *J. Mol. Model.* 7, 306 (2001)
85. B. Roux, *Curr. Opin. Struct. Biol.* 12, 182 (2002).
86. C. E. Capener, I. H. Shrivastava, K. M. Ranatunga, L. R. Forrest, G. R. Smith, and M. S. P. Sansom, *Biophys. J.* 78, 2929 (2000).
87. C. E. Capener, H. J. Kim, Y. Arinaminpathy, and M. S. P. Sansom, *Human Mol. Genet.* 11, 2425 (2002).
88. M. A. Eriksson and B. Roux, *Biophys. J.* 83, 2595 (2002).
89. P. C. Biggin and M. S. Sansom, *Biophys. J.* 83, 1867 (2002).
90. D. P. Tieleman, L. R. Forrest, M. S. Sansom, and H. J. Berendsen, *Biochemistry* 37, 17554 (1998).
91. H. I. Petrache, D. M. Zuckerman, J. N. Sachs, J. A. Killian, R. E. Koeppe, and T. B. Woolf, *Langmuir* 18, 1340 (2002).
92. W. Im and B. Roux, *J. Mol. Biol.* 322, 851 (2002).
93. A. Burykin and A. Warshel, *Biophys. J.* 85, 3696 (2003).
94. O. Beckstein and M. S. Sansom, *Proc. Natl. Acad. Sci. USA* 100, 7063 (2003).
95. G. Hummer, J. C. Rasaiah, and J. P. Noworyta, *Nature* 414, 188 (2001).
96. D. P. Tieleman, B. Hess, and M. S. Sansom, *Biophys. J.* 83, 2393 (2002).
97. O. Beckstein, P. C. Biggin, and M. S. P. Sansom, *J. Phys. Chem. B* 105, 12902 (2001).
98. R. Allen, S. Melchionna, and J. P. Hansen, *Phys. Rev. Lett.* 89, 175502 (2002).
99. A. Burykin, C. N. Schutz, J. Villa, and A. Warshel, *Prot. Struct. Function Genet.* 47, 265 (2002).
100. P. C. Jordan, *Biophys. J.* 83, 1235 (2002).
101. J. Åqvist and V. Luzhkov, *Nature* 404, 881 (2000).
102. S. Berneche and B. Roux, *Nature* 414, 73 (2001).
103. Y. Zhou and R. MacKinnon, *J. Mol. Biol.* 333, 965 (2003).
104. T. W. Allen, O. S. Andersen, and B. Roux, *J. Am. Chem. Soc.* 125, 9868 (2003).
105. S. Berneche and B. Roux, *Proc. Natl. Acad. Sci. USA* 100, 8644 (2003).
106. D. P. Tieleman, M. S. P. Sansom, and G. A. Woolley, *Biophys. J.* 84, 1464 (2003).
107. C. H. Yu and R. Pomes, *J. Am. Chem. Soc.* 125, 13890 (2003).
108. F. H. Stillinger and C. W. David, *J. Chem. Phys.* 69, 1473 (1978).
109. A. M. Smondyrev and G. A. Voth, *Biophys. J.* 83, 1987 (2002).
110. Y. J. Wu and G. A. Voth, *Biophys. J.* 85, 864 (2003).
111. A. Warshel, *Acc. Chem. Res.* 35, 385 (2002).
112. M. A. Lill and V. Helms, *J. Chem. Phys.* 115, 7993 (2001).
113. B. L. de Groot, T. Frigato, V. Helms, and H. Grubmuller, *J. Mol. Biol.* 333, 279 (2003).
114. N. Chakrabarti, E. Tajkhorshid, B. Roux, and R. Pomes, *Structure (Cambridge)* 12, 65 (2004).
115. C. Dellago, M. M. Naor, and G. Hummer, *Phys. Rev. Lett.* 91, 105902 (2003).
116. P. S. Crozier, D. Henderson, R. L. Rowley, and D. D. Busath, *Biophys. J.* 81, 3077 (2001).
117. D. P. Tieleman, H. J. Berendsen, and M. S. Sansom, *Biophys. J.* 80, 331 (2001).
118. G. Cevc, *Biochim. Biophys. Acta* 1031, 311 (1990).
119. A. Kalra, S. Garde, and G. Hummer, *Proc. Natl. Acad. Sci. USA* 100, 10175 (2003).
120. Y. Y. Sham, Z. T. Chu, H. Tao, and A. Warshel, *Proteins* 39, 393 (2000).
121. D. P. Tieleman, in "AIP Symposia Proceedings," al. Sbe (ed.), AIP Press, 298 (2002).
122. C. Sagui and T. A. Darden, *Annu. Rev. Biophys. Biomol. Struct.* 28, 155 (1999).
123. P. Carlon, U. Rothlisberger, and Parrinello, *Acc. Chem. Res.* 35, 455 (2002).
124. U. F. Rohrig, L. Guidoni, and U. Rothlisberger, *Biochemistry* 41, 10799 (2002).
125. L. Guidoni and P. Carloni, *Biochim. Biophys. Acta Biomembr.* 1563, 1 (2002).

126. B. Roux, *Acc. Chem. Res.* 35, 366 (2002).
127. K. M. Robertson and D. P. Tieleman, *Biochem. Cell Biol.* 80, 517 (2002).
128. E. Tajkhorshid, A. Aksimentiev, I. Balabi, M. Gao, B. Isralewitch, J. C. Phillips, F. Zhu, and K. Schulten, *Adv. Protein Chem.* 66, 195 (2003).
129. C. Domene and M. S. Sansom, *Biophys. J.* 85, 2787 (2003).
130. C. E. Capener and M. S. P. Sansom, *J. Phys. Chem. B* 106, 4543 (2002).
131. R. D. Hotchkiss and R. J. Dubos, *J. Biol. Chem.* 132, 791 (1940).
132. D. W. Urry, *Proc. Natl. Acad. Sci. USA* 68, 672 (1971).
133. S. B. Hladky and D. A. Haydon, *Nature* 225, 451 (1970).
134. S. B. Hladky and D. A. Haydon, *Biochim. Biophys. Acta* 274, 294 (1972).
135. O. S. Andersen, *Biophys. J.* 41, 119 (1983).
136. O. S. Andersen, *Biophys. J.* 41, 147 (1983).
137. A. Pullman, *Q. Rev. Biophys.* 20, 173 (1987).
138. O. S. Andersen and R. E. Koeppe, *Physiol. Rev.* 72, 89 (1992).
139. G. A. Woolley and B. A. Wallace, *J. Membr. Biol.* 129, 109 (1992).
140. D. D. Busath, *Annu. Rev. Physiol.* 55, 473 (1993).
141. R. E. Koeppe and O. S. Andersen, *Annu. Rev. Biophys. Biomol. Struct.* 25, 231 (1996).
142. B. A. Wallace, *J. Struct. Biol.* 121, 123 (1998).
143. D. G. Levitt, *Biophys. J.* 22, 209 (1978).
144. P. C. Jordan, *Biophys. J.* 39, 157 (1982).
145. H. Monoi, *Biophys. J.* 59, 786 (1991).
146. T. B. Woolf and B. Roux, *Proc. Natl. Acad. Sci. USA* 91, 11631 (1994).
147. T. B. Woolf and B. Roux, *Biophys. J.* 72, 1930 (1997).
148. S. W. Chiu, S. Subramaniam, and E. Jakobsson, *Biophys. J.* 76, 1929 (1999).
149. F. Tian, K. C. Lee, W. Hu, and T. A. Cross, *Biochemistry* 35, 11959 (1996).
150. F. Tian and T. A. Cross, *J. Mol. Biol.* 285, 1993 (1999).
151. S. Edwards, B. Corry, S. Kuyucak, and S. H. Chung, *Biophys. J.* 83, 1348 (2002).
152. J. Åqvist and A. Warshel, *Biophys. J.* 56, 171 (1989).
153. P. Jordan, *Biophys. J.* 58, 1133 (1990).
154. R. Elber, D. P. Chen, D. Rojewska, and R. Eisenberg, *Biophys. J.* 68, 906 (1995).
155. B. L. de Groot, D. P. Tieleman, P. Pohl, and H. Grubmuller, *Biophys. J.* 82, 2934 (2002).
156. O. S. Andersen, H. J. Apell, E. Bamberg, D. D. Busath, R. E. Koeppe, F. J. Sigworth, G. Szabo, D. W. Urry, and A. Woolley, *Nat. Struct. Biol.* 6, 609 (1999).
157. P. Tang and Y. Xu, *Proc. Natl. Acad. Sci. USA* 99, 16035 (2002).
158. B. Roux and M. Karplus, *J. Am. Chem. Soc.* 115, 3250 (1993).
159. T. W. Allen, T. Bastug, S. Kuyucak, and S. H. Chung, *Biophys. J.* 84, 2159 (2003).
160. T. W. Allen, O. S. Andersen, and B. Roux, *Proc. Natl. Acad. Sci. USA* 101, 117 (2004).
161. M. Sancho, M. B. Partenskii, V. Dorman, and P. C. Jordan, *Biophys. J.* 68, 427 (1995).
162. B. Roux, B. Prodhom, and M. Karplus, *Biophys. J.* 68, 876 (1995).
163. R. Ketchem, B. Roux, and T. Cross, *Structure* 5, 1655 (1997).
164. L. E. Townsley, W. A. Tucker, S. Sham, and J. F. Hinton, *Biochemistry* 40, 11676 (2001).
165. R. MacKinnon, S. L. Cohen, A. Kuo, A. Lee, and B. T. Chait, *Science* 280, 106 (1998).
166. M. LeMasurier, L. Heginbotham, and C. Miller, *J. Gen. Physiol.* 118, 303 (2001).
167. Z. Lu, A. M. Klem, and Y. Ramu, *Nature* 413, 809 (2001).
168. J. H. Morais-Cabral, Y. Zhou, and R. MacKinnon, *Nature* 414, 37 (2001).
169. Y. Zhou, J. H. Morais-Cabral, A. Kaufman, and R. MacKinnon, *Nature* 414, 43 (2001).
170. Y. Jiang, A. Lee, J. Chen, M. Cadene, B. T. Chait, and R. MacKinnon, *Nature* 417, 523 (2000).
171. A. Kuo, J. M. Gulbis, J. F. Antcliff, T. Rahman, E. D. Lowe, J. Zimmer, J. Cuthbertson, F. M. Ashcroft, T. Ezaki, and D. A. Doyle, *Science* 300, 1922 (2003).
172. Y. Jiang, A. Lee, J. Chen, V. Ruta, M. Cadene, B. T. Chait, and R. MacKinnon, *Nature* 423, 33 (2003).
173. Y. Jiang, V. Ruta, J. Chen, A. Lee, and R. MacKinnon, *Nature* 423, 42 (2003).
174. B. E. Cohen, M. Grabe, and L. Y. Jan, *Neuron* 39, 395 (2003).
175. L. G. Cuello, J. G. Romero, D. M. Cortes, and E. Perozo, *Biochemistry* 37, 3229 (1998).
176. L. Heginbotham, M. LeMasurier, L. Kolmakova-Partensky, and C. Miller, *J. Gen. Physiol.* 114, 551 (1999).
177. E. Perozo, D. M. Cortes, and L. G. Cuello, *Science* 285, 73 (1999).
178. Y. S. Liu, P. Sompornpisut, and E. Perozo, *Nat. Struct. Biol.* 8, 883 (2001).
179. R. J. Mashl, Y. Tang, J. Schnitzer, and E. Jakobsson, *Biophys. J.* 81, 2473 (2001).
180. R. Coronado, R. L. Rosenberg, and C. Miller, *J. Gen. Physiol.* 76, 425 (1980).
181. D. Meuser, H. Splitt, R. Wagner, and H. Schrempf, *FEBS Lett.* 46, 447 (1999).
182. H. Schrempf, O. Schmidt, R. Kümmerlen, S. Hinnah, D. Müller, M. Betzler, T. Steinkamp, and R. Wagner, *EMBO J.* 14, 5170 (1995).
183. L. Heginbotham, T. Abramson, and R. MacKinnon, *Science* 258, 1152 (1992).
184. M. S. Sansom, I. H. Shrivastava, J. N. Bright, J. Tate, C. E. Capener, and P. C. Biggin, *Biochim. Biophys. Acta* 1565, 294 (2002).
185. T. W. Allen, S. Kuyucak, and S. H. Chung, *Biophys. J.* 77, 2502 (1999).
186. P. C. Biggin, G. R. Smith, I. Shrivastava, S. Choe, and M. S. Sansom, *Biochim. Biophys. Acta* 1510, 1 (2001).
187. L. Guidoni, V. Torre, and P. Carloni, *FEBS Lett.* 477, 37 (2000).

188. S. Berneche and B. Roux, *Biophys. J.* 78, 2900 (2000).
189. I. H. Shrivastava and M. S. P. Sansom, *Biophys. J.* 78, 557 (2000).
190. P. C. Biggin and M. S. Sansom, *Biophys. J.* 83, 1867 (2002).
191. Y. Liu, M. Holmgren, M. E. Jurman, and G. Yellen, *Neuron* 19, 175 (1997).
192. M. Zhou, J. H. Morais-Cabral, S. Mann, and R. MacKinnon, *Nature* 411, 657 (2001).
193. Y. Jiang, A. Lee, J. Chen, M. Cadene, B. T. Chait, and R. MacKinnon, *Nature* 417, 515 (2002).
194. L. Monticelli, K. M. Robertson, J. L. MacCallum, and D. P. Tieleman, *FEBS Lett.* 564, 325 (2004).
195. I. H. Shrivastava, D. P. Tieleman, P. C. Biggin, and M. S. P. Sansom, *Biophys. J.* 83, 633 (2002).
196. T. W. Allen, A. Bliznyuk, A. P. Rendell, S. Kuyucak, and S. H. Chung, *J. Chem. Phys.* 112, 8191 (2000).
197. B. Roux and S. Berneche, *Biophys. J.* 82, 1681 (2002).
198. A. Grossfield, P. Ren, and J. W. Ponder, *J. Am. Chem. Soc.* 125, 15671 (2003).
199. V. B. Luzhkov and J. Åqvist, *Biochim. Biophys. Acta* 1481, 360 (2000).
200. L. Guidoni, V. Torre, and P. Carloni, *Biochemistry* 38, 8599 (1999).
201. A. Accardi and C. Miller, *J. Gen. Physiol.* 122, 16a (2003).
202. A. Accardi and C. Miller, *Nature* 427, 803 (2004).
203. K. Steinmeyer, C. Lorenz, M. Pusch, M. Koch, and T. J. Jentsch, *EMBO J.* 13, 737 (1994).
204. N. Piwon, W. Grunther, M. Schwake, M. R. Bosl, and T. J. Jentsch, *Nature* 408, 369 (2000).
205. B. D. Simon, R. S. Bindra, T. A. Mansfield, C. Nelson-Williams, E. Mendonca, R. Stone, S. Schurman, A. Nayir, H. Alpay, A. Bakkaloglu, J. Rodri-Guez-Soriano, J. M. Morales, S. A. Sanjad, C. M. Taylor, D. Pilz, A. Brem, H. Trachtman, W. Griswold, G. A. Richard, E. John, and R. P. Lifton, *Nat. Genet.* 17, 171 (1997).
206. C. Miller, *Phil. Trans. Roy. Soc. Lond.* B288, 401 (1982).
207. T. J. Jentsch, T. Friedrich, A. Schriever, and H. Yamada, *Pflugers Arch.* 437, 783 (1999).
208. C. Lorenz, M. Pusch, and T. J. Jentsch, *Proc. Natl. Acad. Sci. USA* 93, 13362 (1996).
209. G. Y. Rychkov, M. Pusch, M. L. Roberts, and A. H. Bretag, *J. Physiol.* 530.3, 379 (2001).
210. M. Kawasaki, M. Suzuki, S. Uchida, S. Sasaki, and F. Marumo, *Neuron* 14, 1285 (1995).
211. K. Steinmeyer, B. Schwappach, M. Bens, A. Vandewalle, and T. J. Jentschh, *J. Biol. Chem.* 270, 31172 (1995).
212. D. Duan, S. Cowley, B. Horowitz, and J. R. Hume, *J. Gen. Physiol.* 113, 57 (1999).
213. T. Friedrich, T. Breiderhoff, and T. J. Jentsch, *J. Biol. Chem.* 274, 896 (1999).
214. C. G. Vonoye and A. L. George, Jr., *J. Physiol.* 539, 373 (2002).
215. G. V. Miloshevsky and P. C. Jordan, *Biophys. J.* 86, 825 (2004).
216. J. Cohen and K. Schulten, *Biophys. J.* 86, 836 (2004).
217. B. Corry, M. O'Mara, and S. H. Chung, *Biophys. J.* 86, 846 (2004).
218. B. Corry, M. O'Mara, and S. H. Chung, *J. Chem. Phys. Lett.* 386, 233 (2004).
219. B. Bennetts, M. L. Roberts, A. H. Bretag, and G. Y. Rychkov, *J. Physiol.* 535, 93 (2001).
220. C. Fahlke, R. Rüdel, N. Mitrovic, M. Zhou, and A. L. George, *Neuron* 15, 463 (1995).
221. C. Fahlke, C. L. Beck, and A. L. George, *Proc. Natl. Acad. Sci. USA* 94, 2729 (1997).
222. C. Saviane, F. Conti, and M. Pusch, *J. Gen. Physiol.* 113, 457 (1999).
223. F. Weinrich and T. J. Jentsch, *J. Biol. Chem.* 276, 2347 (2001).
224. E. W. McCleskey and W. Almers, *Proc. Natl. Acad. Sci. USA* 82, 7149 (1985).
225. P. G. Kostyuk, S. L. Mironov, and Y. M. Shuba, *J. Membr. Biol.* 76, 83 (1983).
226. W. Almers and E. W. McCleskey, *J. Physiol.* 353, 585 (1984a).
227. P. Hess, J. B. Lansman, and R. W. Tsien, *J. Gen. Physiol.* 88, 293 (1986).
228. C. C. Kuo and P. Hess, *J. Physiol.* 446, 629 (1993).
229. W. Almers, E. W. McCleskey, and P. T. Palade, *J. Physiol.* 353, 565 (1984).
230. A. Bahinski, A. Yatani, G. Mikala, S. Tang, S. Yamamoto, and A. Schwartz, *Mol. Cell. Biochem.* 166, 125 (1997).
231. J. Yang, P. T. Ellinor, W. A. Sather, J. F. Zhang, and R. W. Tsien, *Nature* 366, 158 (1993).
232. R. W. Tsien, P. Hess, E. W. McCleskey, and R. L. Rosenberg, *Annu. Rev. Biophys. Chem.* 16, 265 (1987).
233. F. Benzanilla and C. M. Armstrong, *J. Gen. Physiol.* 60, 588 (1972).
234. P. Hess and R. W. Tsien, *Nature* 309, 453 (1984).
235. T. X. Dang and E. W. McCleskey, *J. Gen. Physiol.* 111, 185 (1998).
236. C. M. Armstrong and J. Neyton, *Ann. NY Acad. Sci.* 635, 18 (1991).
237. E. Perozo and D. C. Rees, *Curr. Opin. Struct. Biol.* 13, 432 (2003).
238. R. B. Bass, K. P. Locher, E. Borths, Y. Poon, P. Strop, A. Lee, and D. C. Rees, *FEBS Lett.* 555, 111 (2003).
239. F. Benzanilla and E. Perozo, *Adv. Protein Chem.* 63, 211 (2003).
240. D. E. Elmore and D. A. Dougherty, *Biophys. J.* 81, 1345 (2001).
241. J. Gullingsrud, D. Kosztin, and K. Schulten, *Biophys. J.* 80, 2074 (2001).
242. L. E. Bilston and K. Mylvaganam, *FEBS Lett.* 512, 185 (2002b).
243. G. Colombo, S. J. Marrink, and A. E. Mark, *Biophys. J.* 84, 2331 (2003b).
244. M. Betanzos, C. S. Chiang, H. R. Guy, and S. Sukharev, *Nat. Struct. Biol.* 9, 704 (2002).
245. E. Perozo, D. M. Cortes, P. Sompornpisut, A. Kloda, and B. Martinac, *Nature* 418, 942 (2002).
246. H. Valadie, J. J. Lacapcre, Y. H. Sanejouand, and C. Etchebest, *J. Mol. Biol.* 332, 657 (2003).
247. K. M. Robertson and D. P. Tieleman, *FEBS Lett.* 528, 53 (2002).
248. W. Im and B. Roux, *J. Mol. Biol.* 319, 1177 (2002).
249. W. Im and B. Roux, *J. Chem. Phys.* 115, 4850 (2001).
250. P. S. Phale, A. Philippsen, C. Widmer, V. P. Phale, J. P. Rosenbusch, and T. Schirmer, *Biochemistry* 40, 6319 (2001).

251. T. Schirmer and P. S. Phale, *J. Mol. Biol.* 294, 1159 (1999).
252. E. M. Nestorovich, T. K. Rostovtseva, and S. M. Bezrukov, *Biophys. J.* 85, 3718 (2003).
253. G. A. Woolley, P. C. Biggin, A. Schultz, L. Lien, D. C. Jaikaran, J. Breed, K. Crowhurst, and M. S. Sansom, *Biophys. J.* 73, 770 (1997).
254. M. S. Sansom, *Q. Rev. Biophys.* 26, 365 (1993).
255. D. P. Tieleman, H. J. Berendsen, and M. S. Sansom, *Biophys. J.* 76, 1757 (1999).
256. A. V. Starostin, R. Butan, V. Borisenko, D. A. James, H. Wenschuh, M. S. Sansom, and G. A. Woolley, *Biochemistry* 38, 6144 (1999).
257. V. Borisenko, M. S. Sansom, and G. A. Woolley, *Biophys. J.* 78, 1335 (2000).
258. J. D. Lear, Z. R. Wasserman, and W. F. DeGrado, *Science* 240, 1177 (1988).
259. H. S. Randa, L. R. Forrest, G. A. Voth, and M. S. Sansom, *Biophys. J.* 77, 2400 (1999).
260. Q. Zhong, Q. Jiang, P. B. Moore, D. M. Newns, and M. L. Klein, *Biophys. J.* 74, 3 (1998).
261. L. J. Holsinger, D. Nichani, L. H. Pinto, and R. A. Lamb, *J. Virol.* 68, 1551 (1994).
262. K. C. Duff and R. H. Ashley, *Virology* 190, 485 (1992).
263. F. A. Kovacs and T. A. Cross, *Biophys. J.* 73, 2511 (1997).
264. A. Kukol, P. D. Adams, L. M. Rice, A. T. Brunger, and T. I. Arkin, *J. Mol. Biol.* 286, 951 (1999).
265. L. R. Forrest, W. F. DeGrado, G. R. Dieckmann, and M. S. Sansom, *Fold. Des.* 3, 443 (1998).
266. L. R. Forrest, A. Kukol, I. T. Arkin, D. P. Tieleman, and M. S. Sansom, *Biophys. J.* 78, 55 (2000).
267. K. J. Schweighofer and A. Pohorille, *Biophys. J.* 78, 150 (2000).
268. W. B. Fischer and M. S. Sansom, *Biochim. Biophys. Acta* 1561, 27 (2002).
269. J. D. Lear, *FEBS Lett.* 552, 17 (2003).
270. Y. J. Wu and G. A. Voth, *FEBS Lett.* 552, 23 (2003).
271. M. Montal and S. J. Opella, *Biochim. Biophys. Acta* 1565, 287 (2002).
272. R. Law, D. P. Tieleman, and M. S. P. Sansom, *Biophys. J.* 84, 14 (2003).
273. N. Unwin, *FEBS Lett.* 555, 91 (2003).
274. M. Bentazos, C. S. Chiang, H. R. Guy, and S. Sukharev, *Nat. Struct. Biol.* 9, 704 (2002).
275. S. Sukharev, S. R. Durell, and H. R. Guy, *Biophys. J.* 81, 917 (2001).
276. L. Polo-Parada and S. J. Korn, *J. Gen. Physiol.* 109, 693 (1997).